CRANFIELD UNIVERSITY

Chang Hengky

Synthesis and Characterisation of Nanostructured $BiFeO_3$ for Photodecolourisation of Azo Dyes Using Visible Light

School of Applied Sciences

PhD Thesis

Academic Year: 2009-2013

Supervisors: Professor Robert Dorey & Dr. Steve Dunn

CRANFIELD UNIVERSITY

School of Applied Sciences

PhD Thesis

2013

Chang Hengky

Synthesis and Characterisation of Nanostructured $BiFeO_3$ for Photodecolourisation of Azo Dyes Using Visible Light

Supervisors: Professor Robert Dorey & Dr Steve Dunn

Academic Year: 2009-2013

This thesis is submitted in partial fulfilment of the requirements for the degree of PhD

ABSTRACT

In this work, effort is being made to synthesize a narrow band gap ferroelectric perovskite nanostructure semiconductor that is $BiFeO_3$ (BFO). The BFO nanopowders were synthesized at 650 ℃ using a self-combustion method with glycine as the fuel. The effect of the different fuel concentrations, annealing temperatures and the duration of annealing are all demonstrated to influence the phase and crystallography of the synthesized nanoparticles. The author has demonstrated that the self-combustion process can be used to produce high purity BFO nanopowders which exhibit good absorption in the visible-light regime as determined by the UV-Vis-NIR spectroscopy with a measured optical band gap of 2.22 eV.

The photochemical decolourisation experiment set-up has been developed to assess and demonstrate the efficiency of the organic dye degradation by the synthesized BFO nanopowders on known organic compounds such as Rhodamine B (RhB) and Acid Black 1 dyes under a solar simulator with an air mass (AM) of 1.5. Detailed study was carried out on the effect of the BFO particle surface charge and the organic dyes interaction on the photochemical decolourisation efficiency of the dyes. It was demonstrated that the synthesized BFO powder has the highest photochemical decolourisation efficiency on the RhB dye (cationic dye) at the point of a zero charge (iso-electric point) of the BFO particle. Ferroelectric nature plays important role in the BFO particle surface to dye molecule interactions as BFO shown absorption of dyes at the particle surface during equilibrium test between BFO powders and dye solution without illumination (under dark environment). However, this is not the case for non-ferroelectric nano-TiO_2 where there was no dyes absorption during equilibrium test under dark environment. The energy band structure of the BFO with respect to the RhB dye showed some instability of the material and was liable to photocorrosion. X-ray Photoelectron Spectroscopy (XPS) study was performed on the BFO powder before and after the photochemical decolourisation experiment and showed changes in the chemical environment of Fe^{3+} cations, changes of the Fe^{2+}/Fe^{3+} peaks ratios, hence it was proposed that the

BFO photocorrodes through dissolution of the Fe-O bonds. An experiment was conducted to mitigate the photocorrosion of the BFO by replacing the BFO powder at a fixed interval during the photodeclourisation experiment and showed the dye degradation rate exceeding the rate of the nano TiO_2 (P25 degussa)

The BFO is also doped with metal cations (M) of Copper (Cu) and Tungsten (W), $BiFe_{1-X}M_XO_3$ with the aim to improve the photochemical reactivity of the material under visible light irradiation. The Cu and W doped BFO showed that the increase in the dopant concentration improved the photo-decolourisation rate against the RhB dye. This improvement could be attributed to the decrease in the optical band gap and increased in the carriers' separation that improved the visible light response and the carriers' lifetime respectively. It was also demonstrated that the heterojunction of TiO_2 thin layer coated on the BFO particle's surface creating a heterojunction to protect the BFO and improve its photostability as well as the photochemical reactivity against the RhB dye. Photocatalytic reactivity showed improvement over the pure BFO with steady photodecolourisation rate, and was able to degrade the RhB dye completely within the 6 hour time frame, however still slower when compared to Titania. This is because the thin layer of the TiO_2 is of amorphous state as shown by high resolution TEM image.

ACKNOWLEDGEMENT

The author would like to express his gratitude and appreciation to his project supervisor Dr. Steve. C. Dunn for having provided good advice and guidance in all aspects of this project. He was always available to give direction, vision and encouragement in accomplishing this project.

The author would also like to thank Prof. Rob Dorey for his support during the PhD candidature process and the staff of both the Cranfield University School of Applied Sciences and the Advanced Materials Center at Nanyang Polytechnic for their help and support utilization of the machinery and investigation equipment.

Lastly, to my beloved family and friends, your continuous support and encouragement has always brightened my day, giving me the extra fuel to complete this marathon journey and make each day very special. In addition, the author would like to address special thanks to Dr. Valdew Singh and the School of Engineering Management for their kind understanding and encouragement in finishing this PhD programme.

TABLE OF CONTENTS

LIST OF TABLES

LIST OF FIGURES

1 INTRODUCTION

1.1. Research Motivation

Rapid industrialization has driven earth to massive pollutions, particularly water pollutions due to industrial waste water discharge. Water pollution is a major problem globally and has become the worldwide leading cause of deaths and disease.[1] Hence, waste-water treatment technology has become critical due to the depleted water resources, increase in waste-water disposal costs, and stricter regulations for waste-water discharge that have lowered the permissible contaminant concentrations in waste-water streams[2].

Currently, there is a wide range of persistent organic compounds detected in industrial and municipal wastewater which pose severe problems in biological treatment systems due to their resistance to biodegradation such as toxic organic compounds, surfactants, organic dyes and agriculture chemical wastes such as insecticides and pesticides.[3] The need for safe disposal of the organic compounds in waste water has driven the global efforts in the development of clean and green technologies to degrade the pollutants prior to discharge into the atmosphere and water environments. The use of advanced water treatment technologies to accomplish a high mineralization rate or to transform the persistent organic compound molecules into other harmless substances has generated broad interest. Recently, advanced oxidation processes (AOPs) have gained growing interest in decontaminating organic pollutants. AOPs are highly effective and potent in degrading organic pollutants which involve oxidization, decolourisation and mineralisation process. AOPs are the technologies that lead to the generation of

hydroxyl radical ($^{\cdot}OH$) as the main oxidant by using oxidizing agent such as hydrogen peroxide (H_2O_2), Ozone (O_3), UV irradiation, and photocatalysts.

Photocatalysis refers to the acceleration of the rate of chemical reactions (oxidation/reduction) brought about by the activation of a catalyst, usually a semiconductor oxide, by photon energy. Semiconductor photocatalysis research has gained strong interest after TiO_2 photochemical electrodes were discovered to be able to split H_2O to H_2 and O_2 using UV light[4.] Following that, the photocatalytic oxidation of organic contaminants using TiO_2-based semiconductors as a photocatalyst has been rigorously researched because they have excellent photochemical stability, high-efficiency, non-toxic and low cost.[5,6] Nevertheless, the TiO_2 photocatalytic efficiency is limited to the absorption in the visible-light range. Only about 4% of sun light radiation on earth surface is suitable for the photoexcitation of TiO_2[7] causing the process impractical due to the inefficiency of photocatalysis or photochemical reaction.

A number of alternative systems have been investigated to generate systems that are photoactive under visible light stimulation. These include doping and modification of wide band gap materials such as the doping of TiO_2[8] and recently the use of plasmonic nanostructures grown on the surface of the catalyst.[9] These represent a large and significant global effort to generate photocatalysts that are responsive in the visible region and so enhance the need to find materials that a band gap in the visible region, are effective catalysts and stable. The use of $BiFeO_3$ a material that exhibits a low band gap (*ca.* 2.1 eV)[10] could make a significant contribution to the visibly active photochemical reaction or photocatalysts.

1.2 Scope of the Work

The aim of this research project is to harness the benefits of both low band gap particulate catalysts capable of photoactivation at a visible light range as well as a photoelectrochemical cell characteristic due to its multiferroic nature (ferroelectricity) by inducing a charge separation in the particulate catalysts. It was hypothesized that by using a ferroelectric material with spontaneous internal depolarization fields, it is possible to increase the separation of the sites of the two half reactions and reduce the recombination of photogenerated charge carriers'. The separation of the reaction sites may significantly increase the efficiency of the photocatalysis process.

The idea of achieving charge separation by band bending was originally conceived by Nozik et al.[11] using photochemical diodes that consist two electrodes of the photoelectrochemical cell which fused together to produce either p – n type or Schottky – type devices. Giocondi et al[12,13] and Dunn et al[14,15,16,17] have shown that the spatial charge separation can be achieved using ferroelectric materials such as barium titanate ($BaTiO_{3)}$, Lead zirconate titanate (PZT), and Lithium Niobate ($LiNbO_3$) when under illumination. The internal polarization field creates energy band bending that separates the charge carriers, hence, prolong the photogenerated electrons and holes lifetime. The photogenerated electrons and holes will move towards the different surfaces of the crystal with different polarisation, and thus separate the oxidation and reduction sites. Thus, the objectives of this research are:

1. To develop a detailed understanding of the low bandgap semiconductor $BiFeO_3$ particulate nanostructures as visible light activated photocatalysis with

consideration of its multiferroic nature (the surface charge-dye interactions) and the relative energy band structures against various organic azo dyes.

2. To improve photocatalytic reaction against organic azo dyes by means of ionic doping and surface modifications. Metallic dopants will be introduced to $BiFeO_3$ particulates during the synthesis process with the intention to increase the carriers' lifetime and hence photocatalyst reactivity and stability. Surface modifications with a thin layer coating of another semiconductor oxide with favourable band structure to enhance the charges separation, thus will increase the photocatalytic reactivity and stability of the catalyst.

2 LITERATURE REVIEW

2.1. Introduction to Perovskite Oxides Material

A perovskite oxide is any compound which has the general molecular formula of ABO_3 and similar crystal structure as that of calcium titanium oxide ($CaTiO_3$), widely known as the perovskite structure, where A and B denote a large cation and small cation respectively. The perovskite oxide structure is considered as one of the most common structures of the complex oxides materials on the earth.

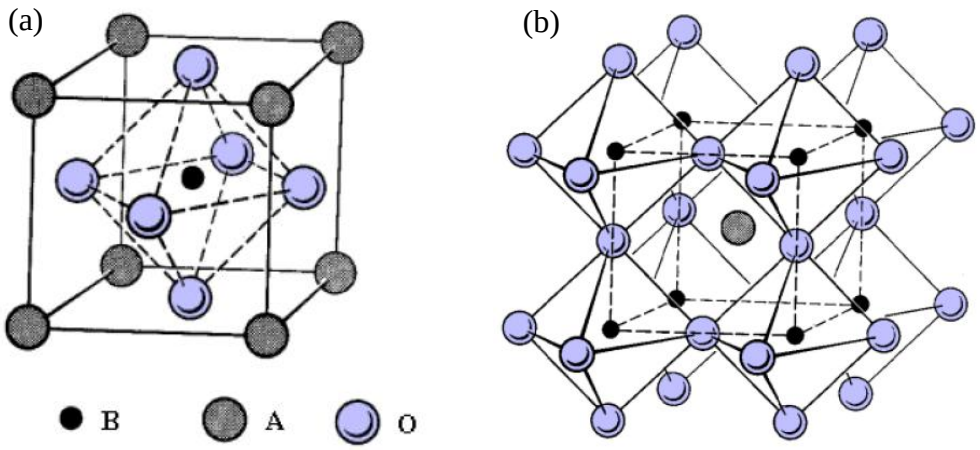

Figure 2.1 Two typical views of ideal cubic ABO_3 perovskite structure unit cell. (a) The A atom located at the corner of the cube (0,0,0), and B atom located at the centre position of the cube (½ , ½ , ½), while oxygen atom sits at the face centre positions (½ , ½, 0); (b) ABO_3 structure in terms of BO_6 octahedral networks.

The simplest perovskite structure has a standard cubic symmetry as shown in Figure 2.1 (a), where “A” atom has 12 oxygen atoms neighbours and “B” atom sits at the centre of an octahedron composed of six oxygen atoms. The 'A' atoms are larger than the 'B' atoms. Meanwhile, in an alternative view cubic structure, it can also be outlined as a 3D network of corner sharing the BO_6 octahedral network as

shown in Figure 2.1 (b). In 1926, Goldschmidt[18] defined a parameter, tolerance factor *t*, to accurately describe the stability of a perovskite structure. The factor *t* which associates with the ionic radius is obtained upon the concept of the well-known closed pack theory[19] , and given as:

$$t = \frac{r_A + r_0}{\sqrt{2}\,(r_B + r_0)} \qquad \text{Equation 2.1}$$

Where r_A, r_B and r_0 correspond to the ionic radius of A, B and O atoms respectively. A change in A and B atomic species will result in the change of the *t* value, thus, the crystallographic symmetry will be lowered and can be tuned to orthorhombic, rhombohedral, tetragonal or trigonal in many perovskites. Hence, a broad range of properties will be brought by the changes in molecular formula and crystal structures symmetry.

2.2 Piezoelectricity

Piezoelectricity is the ability of crystalline materials to generate an electrical charge proportional to mechanical deformation. The name comes from an ancient Greek word *piezein* which means to ‘squeeze’ or ‘press’. With the extensive knowledge of pyroelectricity and its crystal structures, the Curie brothers were the first to discover piezoelectricity in 1880 in various crystals including zincblende, tourmaline, cane sugar, topaz, Rochelle salt (sodium potassium tartrate tetrahydrate) and quartz.[20] Quartz and Rochelle salt materials showed the most piezoelectricity effect. The Curie brothers, however, did not predict the converse piezoelectric effect. Within a year in 1881, Lippmann predicted the converse piezoelectric effect based on thermodynamic considerations. This behaviour was also confirmed by the Curies and they went on to obtain quantitative proof of the complete reversibility of

electro-elasto-mechanical deformations in piezoelectric crystals. The first practical applications came a few decades later. In 1918, Langevin developed an ultrasonic submarine detection technique using a quartz-based piezoelectric transducer[21] known as sonar, was subsequently used during both world wars. Since then, piezoelectric materials have found many applications in phonograph pickups, air and instrument transducers, wave filters and high voltage sources.[19]

A stress σ only causes proportional strain ε in ordinary solid crystals, and both are related by an elastic modulus (Y), $\sigma = Y \varepsilon$. Piezoelectricity is the additional creation of an electric charge by the applied stress, and this is the ***direct*** piezoelectric effect. The charge induced is proportional to the applied force, and thus has opposite sign for compression and tension. The relations of dielectric displacement D (charge Q per unit area) and stress σ, may be as follows:

$$D = Q / A = d \sigma \ldots\ldots \quad (d \text{ expressed in coulombs/Newton}) \qquad \text{Equation 2.2}$$

The ***converse*** effect of piezoelectricity, where an applied electric field E produces a proportional strain ε, either expansion or contraction depending on the polarity of electric field E, is written as follows:

$$\varepsilon = d E \ldots\ldots \quad (d \text{ expressed in meters/Volt}) \qquad \text{Equation 2.3}$$

For both ***direct*** and ***converse*** effects, the proportionality constant is d, the piezoelectric constant, which is numerically identical for both ***direct*** and ***converse*** effects, where:

$$d = D / \sigma = \varepsilon / E$$

High *d* constant is desirable for materials in the application intended to develop mechanical motion or vibration, such as ultrasonic transducers or sonar.

Another piezoelectric constant is *g* which represents the electric field produced by a stress, and its units are *meter.volts/Newton.* The permittivity relates the *g* constant to the *d* constant by:

$$g = d / \epsilon' = d / K\epsilon_0 \qquad \text{Equation 2.4}$$

High *g* constant is desirable for materials in the application intended to generate voltages in response to mechanical stress, such as in spark generators and phonograph pickup.

k constant, the electromechanical coupling factor, measures the fraction of the electrical energy converted to mechanical energy when an electric field is applied (or vice versa when a crystal is stressed). The relationship is in terms of k^2:

$$k^2 = \frac{\text{electrical energy converted to mechanical energy}}{\text{input electrical energy}} \qquad \text{Equation 2.5}$$

or

$$k^2 = \frac{\text{mechanical energy converted to electrical energy}}{\text{input mechanical energy}} \qquad \text{Equation 2.6}$$

Because the conversion of mechanical to electrical energy (or vice versa) is always incomplete, k^2 is always < 1, and thus *k* is also < 1. Typical values of *k* are 0.10 for quartz crystal, 0.40 for barium titanate ceramic, 0.5-0.7 for Lead Zirconate Titanate (PZT) ceramic, and as much as 0.9 for Rochelle salt at its curie point of 24˚C.[19]

2.3 Primary Ferroics

A primary ferroic material is a crystalline solid that exhibits a spontaneous magnetization, polarization or strain. And the orientation of these spontaneous orders can be reoriented by an applied magnetic field, electric field, or mechanical stress below a characteristic transition temperature (Currie temperature). The three simple primary ferroics are ferromagnetic, ferroelectric, and ferroelastic,[22] listed in table 2.1

Table 2.1 The three simple primary ferroics

Ferroic Classes	Orientation States	Switching Forces	Example
Ferroelectric	Spontaneous polarization (P)	Electric Field (E)	$BaTiO_3$
Ferromagnetic	Spontaneous magnetization (M)	Magnetic Field (H)	Fe_3O_4
Ferroelastic	Spontaneous strain (S)	Mechanical Stress (T)	Nitinol

2.3.1 Ferroelectricity and Ferroelectric Materials

The first materials discovered to exhibits ferroelectricity was Rochelle salt in 1921. Since then, ferroelectric materials have received a great amount of interest in the past few decades and have been used in many applications such as non-volatile ferroelectric random access memories (NVFRAM), dynamic random access memories (DRAM), sensors and microactuators.[23] A ferroelectric crystal possesses at least two equilibrium orientations of the spontaneous polarization vector in the absence of an external electric field. The spontaneous polarization vector in the ferroelectric crystal can be switched between the two equilibrium orientations by an

electric field.[23] Figure 2.2 shows a hysteresis loop indicated with important parameters such as a coercive field (E_c), remnant polarization (P_r) and saturation polarization (P_s), illustrates the polarization switching in ferroelectric materials by alternate external electric field.

According to the number of rotational axes and reflection planes the crystalline solid exhibit, the structure of all crystals can be classified into thirty-two crystal classes. Among these, only eleven crystals exhibit the existence of a centre of symmetry, thus the crystals are centrosymmetric and cannot possess any polar properties. The remaining twenty-one crystal classes do not have a centre of symmetry (non-centrosymmetric), thus, it is possible for them to have one or more polar axes, and odd-rank tensor properties. All of the twenty-one non-centrosymmetric crystal exhibit piezoelectric effect, defined by a change in electric polarity under applied stress, and vice versa (converse piezoelectric effect).

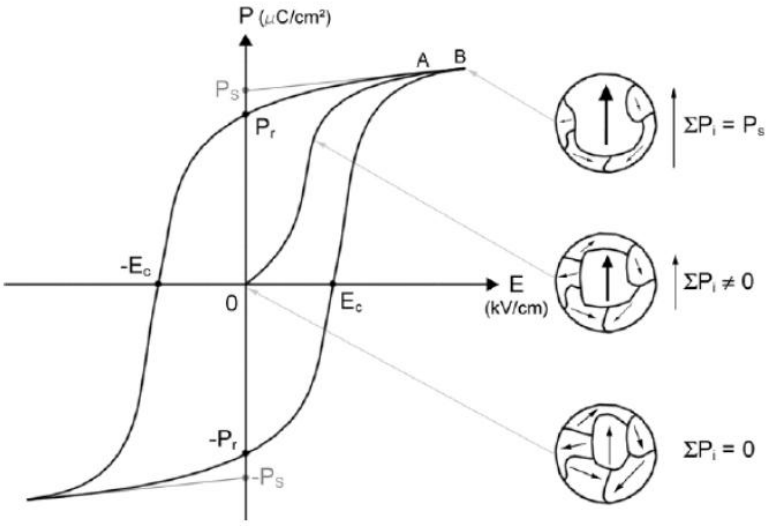

Figure 2.2 Ferroelectric hysteresis loop illustrating the polarization switching.[23]

Out of the twenty piezoelectric classes, ten possess a unique polar axis because they are spontaneously polarized, and this spontaneous polarisation value is temperature dependent. A change in the polarization occurs when the temperature changes and electric charges can be observed on the crystal faces perpendicular to the polar axis. This is called the pyroelectric effect, thus, the ten crystal classes with a unique polar axis are also called pyroelectric classes. Ferroelectric crystals belong to the pyroelectric family, but the direction of the spontaneous polarization in ferroelectric crystals can only be reversed by an external electric field.

Ferroelectrics crystals are non-centrosymmetric, with the positive and negative charges having different centres of symmetry resulting in a spontaneous polarized crystal. The most extensively studied and widely used ferroelectric crystals are the perovskite ferroelectrics with a general formula of ABO_3 such as $BaTiO_3$. In the case of $BaTiO_3$ and other perovskite oxides (ABO_3), the tetravalent B cation located in the centre of an octahedron made up of six oxygen ions. Above its critical temperature (Curie temperature, T_c), the $BaTiO_3$ structure maintains the cubic shape and is centrosymmetric as shown in figure 2.3 (a). Below T_c, the octahedral cages of oxygen distorted and the positive ions (Ti^{4+}) shift to off-centre positions resulting in a tetragonal structure, hence the crystal becomes polarized[24,25] as depicted in figure 2.3 (b). Typically, ferroelectric crystals demonstrate the ferroelectricity effect only at temperature below the phase transition temperature (Curie temperature, T_c), and they are paraelectric above this Curie temperature.[26]

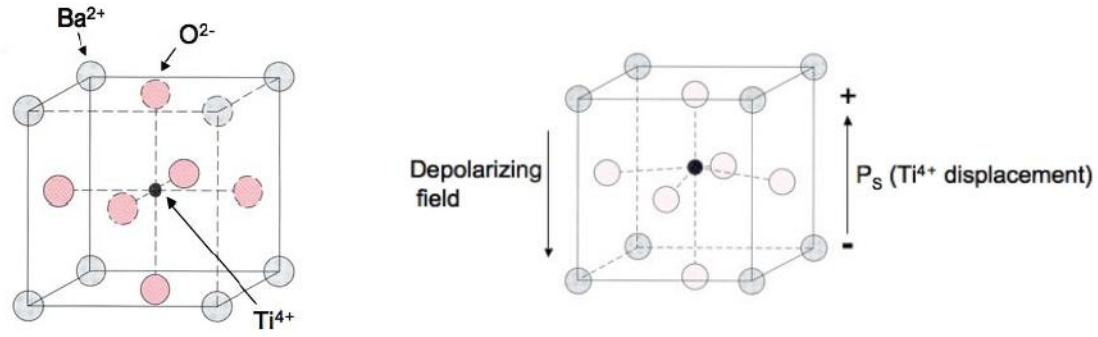

(a) (b)

Figure 2.3 – (a) Cubic perovskite unit cell structure of $BaTiO_3$. (b) Tetragonal crystal structure of ferroelectric $BaTiO_3$ due to Ti^{4+} displaced in +z direction causing the offset of the unit cell's positive and negative centres of symmetry, resulting in the unit cell polarization.[24,25]

2.3.1.1 Lattice Dynamic Theory (Soft Phonon) of Ferroelectricity

About fifty years ago, Cochran and Anderson[27,28] suggested that the phase transition in the ferroelectrics may be associated with a lattice vibrational mode which exhibits instability at the transition temperature causing minute displacements of atoms in the unit cell that results in the spontaneous polarization. This mode is called the soft phonon or soft mode. The frequency of the soft phonon decreases when the temperature cooled down approaching the critical temperature (T_c). Freezing of the vibrations at T_c cause the restoring force decreases to zero, and give rise to the corresponding reduction in symmetry (Polarization, P_s).

2.3.1.2 Domain Structure of Ferroelectric

Ferroelectric domain is the regions within a ferroelectric crystal with uniformly oriented polarisation and the boundary or plane separating the two

domains is called a domain wall, which are a few atomic steps thick. Due to the depolarising field energy, multiple ferroelectric domains form to minimise the depolarisation field, hence no net polarisation in the ferroelectric materials, in the case of unpoled ferroelectric. Thus, a ferroelectric crystal forms into separate domains during synthesis to achieve equilibrium energy level between the domain walls and the depolarisation field of the crystal.[29] The sizes of the domains in a crystal in equilibrium are determined by the minimisation of the depolarisation field energy and the domain wall energy: $W_E + W_W$,[23] yield:

$$d = \left(\frac{\sigma t}{\varepsilon^* P_0^2} \right)^{1/2} \qquad \text{Equation 2.7}$$

where d is a domain width, σ is the energy per unit area of a domain wall, t is the crystal thickness, ε^* is a dielectric constant of the ferroelectric, and P_0 is the polarization of the domain.

Domains with polarisation vector in +z direction are 'up'(c+) domains, and domains with polarisation vector in -z direction are 'down'(c-) domains. The domains that lie in ±x or ±y directions are the domains that lie on the surface plane are lateral domains, indicated as (a) as shown in figure 2.4. Figure 2.4 illustrates the various domains and domain boundaries. The boundaries that separate the "a" and "c" domains are called 90˚ boundaries, and those separating c+ and c- domains are called 180˚boundaries. The boundary name implies the angle between the polarisation vectors between the adjacent domains.

Both 180˚ and 90˚ domain walls formation minimise the depolarisation field due to the compensation of the surface charge in an unpoled ferroelectric. However,

only 90˚ domain wall formation can release the elastic energy stored in the ferroelectric crystal. The polarization vector for a polarized tetragonal crystal, e.g. $BaTiO_3$ is in the direction of the [001] in the c-axis. Hence, when one domain meets the other in the crystal, the polarization directions on either side of domains can only be either 90˚ or 180˚.[23] The domain walls motion and interaction will significantly affects the piezoelectric, mechanical and optical properties of the ferroelectrics structure.[30]

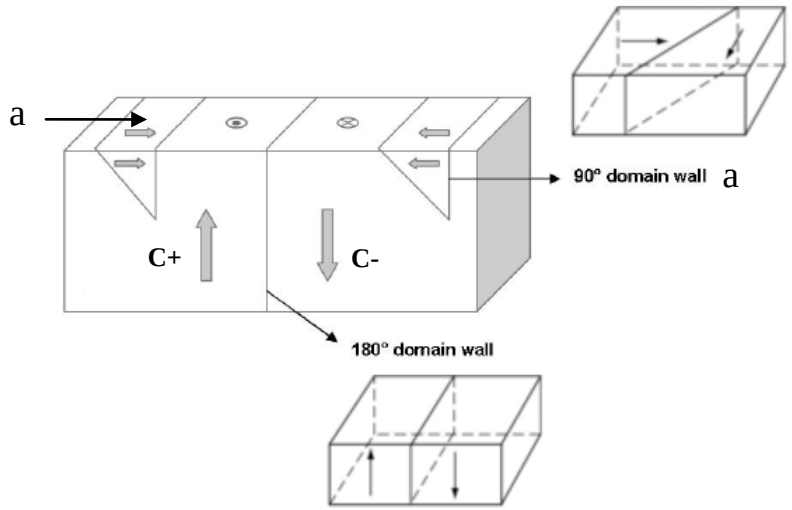

Figure 2.4 Schematic representations of the domain walls in a ferroelectric. Boundaries between anti parallel out of the plane domains are called 180˚ domain walls whereas those between out-of-plain and in-plain are 90˚ walls. Convention is based on the angle between the polarization directions in the adjacent domains.[31]

2.3.1.3 Phase Transition of Ferroelectricity

While the lattice dynamic theory provides correlations between the microscopic lattice vibrations and the macroscopic properties (e.g. polarization) of ferroelectric crystals, the thermodynamic theory provide correlations between

different macroscopic properties such as polarization, dielectric constant and temperature. In the Landau-Devonshire theory,[26, 32] it is assumed that the Gibbs free energy equation can be expanded in a polynomial power series of the system order parameter. For a ferroelectric, the macroscopic order parameter is polarization (P), and the microscopic polarization is the a set of ions displacement (x) from their position midway along some double well potential, for example, the Ti^{4+} ions displacement in $BaTiO_3$ as shown in figure 2.3. It is assumed that (P) is proportional to (x). Hence, the free energy is assumed to have the explicit form:

$$F(P,T,E) = -EP + \alpha_0 + \frac{1}{2}\alpha_1 P^2 + \frac{1}{4}\alpha_2 P^4 + \frac{1}{6}\alpha_3 P^6 \qquad \text{Equation 2.8}$$

where α_n (n=1, 2, 3,…) is the temperature dependent dielectric stiffness, and n is the tensor rank of the dielectric stiffness. The polynomial series expansion was terminated rather arbitrarily at P^6 for mathematical simplicity. α_0 is a constant of no importance and the coefficient α_1 is temperature dependent parameter and has the form of : $\alpha_1 = \gamma (T - T_o)$, where γ is a positive constant and T_o is the phase transition temperature that may not be necessarily equal to Curie temperature (T_c). This form of α_1 is a result related to the mean field theory, and has been experimentally validated by Curie-Weiss law. The mean field theory assumed that every ion in a double well potential in the crystals interact with every other such ion equally, independent of how far away it is. At $T < T_o$, α_1 value is negative, and it would indicates that the unpolarized state is unstable, hence the system is ferroelectric.

When the unpolarized crystal has a centre of symmetry, this Landau-Devonshire polynomial series expansion equation of P does not contain terms in

odd power, which is generally true for most of the perovskite ferroelectrics. In thermal equilibrium, the spontaneous polarization P_s can be achieved by minimizing the free energy as a function of P, which is the differentiation of equation 2.8 with respect to P:

$$\frac{\partial F}{\partial P} = 0$$

$$-E + \alpha_1 P + \alpha_2 P^3 + \alpha_3 P^5 = 0$$

Or $E = \alpha_1 P + \alpha_2 P^3 + \alpha_3 P^5$ Equation 2.9

Two cases are of interest: If the coefficient α_2 is positive, we can neglect the α_3 coefficient in equation 2.8, hence the polarization under the zero external field can be found from equation 2.9, and become:

$$\gamma (T - T_o) P_s + \alpha_2 P_s^3 = 0$$ Equation 2.10

Solving equation 2.10 gives: $|P_s| = \left(\frac{\gamma}{\alpha_2}(T_o - T)\right)^{1/2}$ Equation 2.11

In the second order transition, the change of the free energy and polarization at the transition temperature are continuous and in this case there is no latent heat of transition and the Curie Temperature is equal to the phase transition temperature ($T_c = T_o$). The temperature dependence of spontaneous Polarization of the second order phase transition is qualitatively sketched in figure 2.5 (a). The curves for Gibbs free energy (F(x)) versus the displacement (x) are qualitatively sketched in figure 2.5 (b). When α_1 coefficient is positive ($T \geq T_o$) the free energy curve has a single minimum at $x = 0$, but when α_1 is negative ($T < T_o$) the curves acquire a double-minimum form with minima at non-zero values of the displacement as shown in figure 2.5 (b).

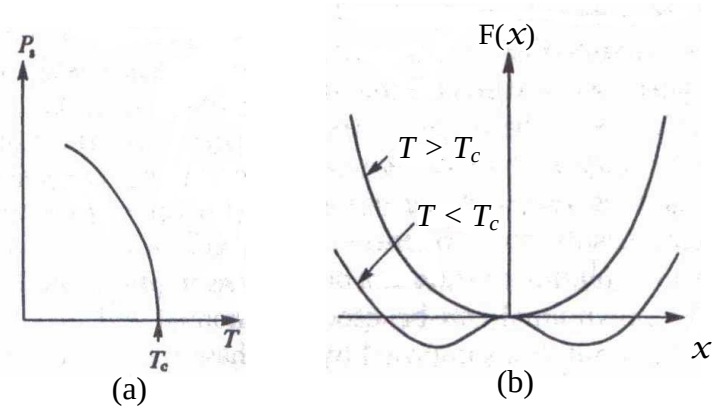

Figure 2.5 The second order phase transition spontaneous polarization against temperature curve (a) and the temperature dependence free energy against the atomic displacement curves for the second order phase transition (b).[23]

If α_2 is negative, the phase transition is discontinuous (first order), and the Curie temperature is not equal to the phase transition temperature ($T_c \neq T_o$) but is higher as seen in figure 2.6(b). Rewrite the equation 2.8 with $\alpha_2 = -\alpha_2'$ gives:

$$F(P,T,E) = -EP + \alpha_0 + \frac{1}{2}\alpha_1 P^2 - \frac{1}{4}(\alpha_2')P^4 + \frac{1}{6}\alpha_3 P^6 \qquad \text{Equation 2.12}$$

As a function of temperature, the free energy curves (F(x)) against the displacement (x)) at various temperatures take the qualitative form shown in figure 2.6(b). The first order transition is characterised by the meta-stable phase's existence during the phase transition and a sudden increase of polarization occurs at T_c. Figure 2.6(a) shows the plot of P_s versus the temperature for a first order phase transition.

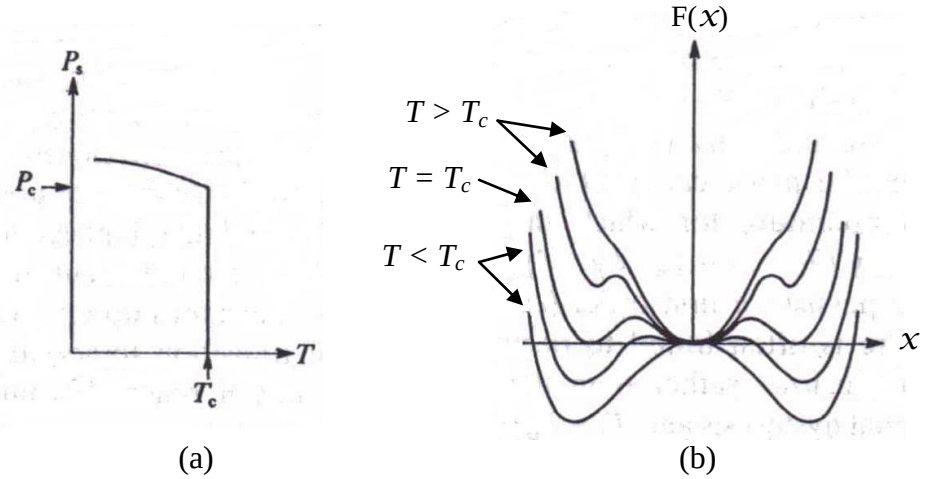

(a) (b)

Figure 2.6 The first order phase transition spontaneous polarization against temperature curve (a) and the temperature dependence free energy against the atomic displacement curves for the first order phase transition (b).[23]

2.3.2 Magnetism and Magnetically Ordered States

The magnetism phenomenon has been known for thousands of years. The first permanent magnetic material identified and studied was the Lodestone (Fe_3O_4). The magnetic moment of an atom/ion derived from three main sources: (1) the spin of electrons; (2) electron orbital angular momentum about the nucleus; and (3) a change in the orbital moment induced by an applied external magnetic field. The first two effects give paramagnetic behaviours to the magnetization, and the third one gives a diamagnetic contribution.[32]

The overall magnetic property of a crystal depends on two factors: (i) the magnetic dipole moments associated with each individual atom/ion, and (ii) the interactions between these magnetic dipole moments. For a single isolated electron,

the strength of the magnetic field associated with it is term as Bohr magnetron, given as: $\beta = \frac{eh}{4\pi m_e}$ and has the value 9.27×10^{-24} Am^2 or JT^{-1}. The magnetic susceptibility, $\chi_m = H/M$, is generally a good indication of magnetic properties. It defines the degree of magnetization of a material in response to an external applied magnetic field.

When there are no unpaired electrons around each atom/ion, there will be no net magnetic moments associated with them, since in a fully filled orbital both orbital moments and electron spins cancelled to zero. Hence, the material will show a ***diamagnetic*** behaviour. The magnetic susceptibility value of diamagnetic materials is negative and small, for instance, the silicon crystal is diamagnetic with $\chi_m = -5.2 \times 10^{-6}$. When an external magnetic field applied to diamagnetic materials, it will slightly unbalance the orbiting electrons in atom and creates small magnetic dipoles that oppose the applied field. This phenomenon produces a negative magnetic effect in response to the applied magnetic field.

In the case of atoms/ions with unpaired electrons, every atom/ion has a net magnetic dipole moment. The interactions between the magnetic dipole moments in the crystal will determine the magnetism behaviour of the materials and may show paramagnetism (PM), ferromagnetism (FM), antiferromagnetism (AFM) and ferrimagnetism (FIM). The magnetic susceptibility value of paramagnetic is positive and small with χ_m ranges from 10^{-6} to 10^{-2}. Individual magnetic dipoles of the atoms are aligned by an applied external field, thus slightly increase the magnetic induction, *B.*

Ferromagnetism consists of parallel aligned adjacent magnetic moments, as shown in figure 2.7 (a). The magnetic susceptibility χ_m of ferromagnetic is positive and very large ($10^1 < \chi < 10^6$). Hence, under an applied external magnetic field, very large magnetization will be created by the ferromagnetic material. The relationship between the magnetization (*M*) and the applied field (*H*) is nonlinear and complicated. Repeated magnetization and demagnetization will lead to the hysteresis loop and large magnetic field can be retained after the applied field is removed, remnant magnetization. Ferromagnetism exists below a critical temperature called the Curie temperature T_c, above T_c, ferromagnetism is lost and becomes paramagnetic.

Antiferromagnetic order consists of antiparallel aligned equal magnetic moments; hence there is no net magnetic moment, figure 2.7 (b). And, ferrimagnetic order consists of antiparallel unequal magnetic moments, resulting in a non-zero net magnetization, figure 2.7 (c). Ferrimagnetic also has a large magnetic susceptibility, in the range of $10^1 < \chi_m < 10^4$.

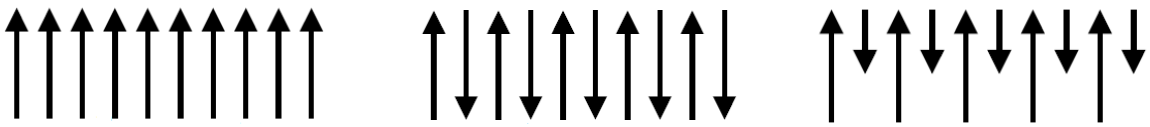

(a) (b) (c)

Figure 2.7 Schematic pictures of (a) ferromagnetic, (b) antiferromagnetic and (c) ferrimagnetic orders. Figure adapted from Kittel *et al*.[32]

2.3.3 Multiferroic Materials

Ferroelectric crystal possesses stable and switchable spontaneous polarization which relies on atom displacements in its crystal structure[24] while a ferromagnetic crystal exhibits a stable and switchable magnetization that arises from the atomic electron spin and the quantum mechanical phenomenon.[33] The combination of these two effects is known as "multiferroicity". According to the original definition, multiferroic material is a class of material that simultaneously exhibits more than one primary ferroic order parameter of ferroelectricity, ferromagnetism, and antiferromagnetism in the same material.[34] Multiferroic materials offer a wide opportunity for potential applications in information storage, spintronic devices and sensors. Ferroelectric and magnetism origins involved with of-centre structural distortions and local electron spins of atoms respectively. Ferroelectricity and magnetism could possibly coexist in a material, however the interplay between these properties has rarely been observed.[37]

The basic concept of multiferroicity or magnetoelectricity can perhaps be originated to Pierre Curie in the late 19th century.[35] After linear coupling of magnetoelectricity was defined and predicted to occur in the specific Cr_2O_3 by Dzyaloshinskii in 1957,[36] the magneto-electric (M-E) coupling coefficient α_{ij} was experimentally measured to be non-zero by Astrov in 1960.[37] Unfortunately, the paraelectricity and antiferromagnetism of Cr_2O_3 make it impossible for industrial applications. A small number of breakthroughs took place in this area during the 1960s. Schmid demonstrated the first magneto-electric switching on his work to boracites ($Ni_3B_7O_{13}I$).[38] Since boracites only exhibits its magnetoelectricity at

extremely low temperature (below 60 ℃), it was impractical for device applications.

Typical multiferroics materials are those from the group of the perovskite transition metal oxides, rare-earth manganites and -ferrites (e.g. $TbMnO_3$, $HoMn_2O_5$, $LuFe_2O_4$). Other examples of multiferroics materials are the bismuth alloys $BiFeO_3$ and $BiMnO_3$, and the non-oxides such as $BaNiF_4$ and spinel chalcogenides such as $ZnCr_2Se_4$. These single phase alloys show rich phase diagrams combining different ferroic orders in separate phases. Besides the single phase multiferroics, composites and heterostructures exhibiting more than one ferroic order parameter are also studied extensively.[39,40,41]

2.4 Fundamentals of the $BiFeO_3$

Bismuth Ferrite ($BiFeO_3$) is one of the few single phase materials that exhibit both ferroelectric and antiferromagnetic properties at room temperature. $BiFeO_3$ material was first synthesized by Royen and Swars in 1957. A number of studies have been focused on this compound motivated by its multiferroic properties and the potentially high magnetoelectric property.

2.4.1 Crystallographic Structure of the $BiFeO_3$

In order to better explore this $BiFeO_3$ material, it would be essential to have an understanding of its basic crystal structure. The atomic structure of $BiFeO_3$ was determined by Michel et al. in 1969[42] who performed an x-ray diffraction on a

single crystal and a neutron diffraction on $BiFeO_3$ powder samples. Under an ambient temperature, $BiFeO_3$ belongs to the *R*3*c* point group with a highly distorted perovskite structure in rhombohedral symmetry containing 2 formula units of $BiFeO_3$[43] with a lattice dimension of $a = b = c = a_r = 5.63$ Angstrom, distorted angle of $\alpha = \beta = \gamma = \alpha_r = 59.4^{o}$ at room temperature[44]. The magnitude of the ion shifts in this rhombohedral symmetry is Bi: 0.62 Å along [111]; Fe: 0.23 Å along [111]; O: 0.30Å along [111], all values ± 0.03 Å.

The rhombohedral symmetry can also be represented by the pseudo-cubic structure with a cell lattice parameter of a_c = 3.965 Å, and with a pseudo-cubic angle α_c equals to *ca*. 89.3 – 89.4°. Alternatively, the structure can also be characterized in a hexagonal frame of reference by connecting two perovskite cubes along with their body in diagonal, *i.e.*, $[001]_{\text{hexagonal (h)}} \parallel [111]_{\text{pseudocubic (c)}}$ as shown in figure 2.8. The hexagonal lattice parameters are a_h = 5.58 Å and c_h = 13.90 Å.[45,46] The magnetic and electrical properties of the BFO crystal are often expressed in the hexagonal cell, and the pseudo-cubic direction where the $[111]_c$ corresponding to the hexagonal $[001]_h$.

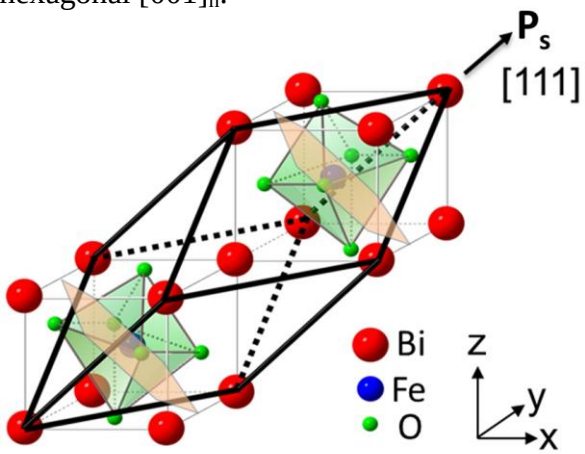

Figure 2.8 Schematic diagrams of a distorted rhombohedral perovskite structure of the BFO. The ferroelectric polarization and antiferromagnetic plane is indicated by the arrow sign and shaded planes respectively. Adapted from Chu *et al.*[47]

In the BFO lattice, the FeO_6 octahedra have a rotation angle, a result from its extra-large volume that buckles into the cell, Figure 2.8. The rotation angles of the two adjacent octahedras are +12 °and -12 ° around the polar $[111]_r$ axis, which was first discovered by Achenbach with neutron diffraction measurement,[48] and later confirmed by Sosnowska.[49] This rotation does not only determine its space group of *R*3*c*, but also indicates the Fe-O-Fe angle to be *ca.* 154-156 ° which is of great importance in establishing the magnetic ordering temperature.[46]

2.4.2 Electrical Properties of the $BiFeO_3$

Bismuth ferrite undergoes a ferroelectric ordering or spontaneous polarization Ps oriented along $[001]_h$ or $[111]_c$ at a T_c of 1100 °K.[51,52,53] The polarization arises due to the distortion of the Bi^{3+} and Fe^{3+} cations from their centro-symmetric positions. Due to current leakage and low resistivity of the bulk $BiFeO_3$ samples, electrical characterization on bulk $BiFeO_3$ has become very difficult. Teague *et al.* successfully measured the hysteresis loop of $BiFeO_3$ with liquid nitrogen in order to lower the charge carrier mobility and leakage currents[50], ending the controversy about whether the $BiFeO_3$ is ferroelectric or antiferroelectric. The measured spontaneous polarization was reported to be 3.5μC/cm^2 along the <100> direction and 6.1μC/cm^2 along <111>, this value is much smaller compared to other ferroelectric material with such a high Curie temperature and a large c/a distortion. The current leakage problem is likely due to defects and non-stoichiometry of the $BiFeO_3$ crystals. It has been the bottle neck for more comprehensive studies about the bulk $BiFeO_3$ and caused limited applications of this material.

While the ferroelectricity of the BFO was once considered to be very weak,[50] however, research by Ramesh's group[51] have shown a much higher P_s along the $[001]_c$ and $[111]_r$, approaching values of 0.6 C/m^2 and 1.0 C/m^2 at room temperature respectively (Figure 2.9) on single crystalline thin films fabricated by a pulsed laser deposition (PLD). Recently, Lebeugle[52] and Shvartsman[53] also proved that the BFO has high P_s through their high-quality single crystals and ceramics with around 60 $\mu C/cm^2$ normal to $[001]_c$ and almost 100 $\mu C/cm^2$ $[111]_r$ respectively, a result which is similar to Ramesh's[51] results.

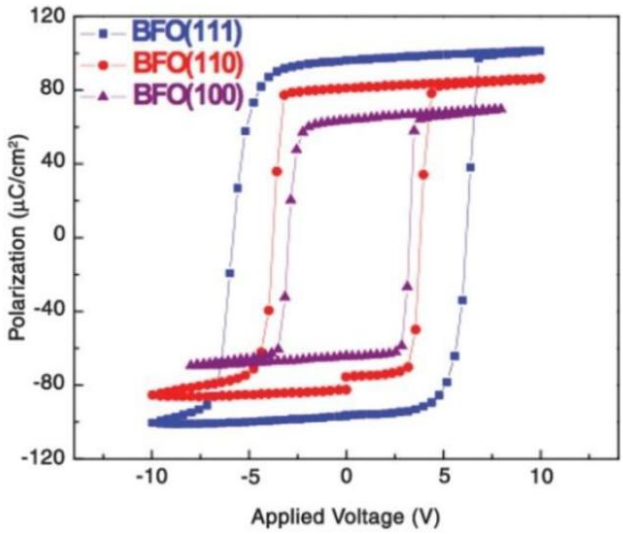

Figure 2.9 The ferroelectric polarization hysteresis loops measurement of the epitaxial BFO thin films with different crystallographic orientations.[51]

2.4.3 Magnetic Properties of the $BiFeO_3$

Magnetic properties of bulk $BiFeO_3$ have been studied for many years. Below its Neel Temperature (T_N~643 K), $BiFeO_3$ has a G-type antiferromagnetic configuration where the spin is provided by the transition metal cation Fe^{3+} with a

magnetic point group 3*m*. In this arrangement, the Fe^{3+} cations are surrounded by six antiparallels as their nearest neighbours.[54] The antiferromagnetic order of $BiFeO_3$ is oriented along the $[001]_h/[111]_c$ direction and the spin rotation plane is parallel to the $[110]_h$. A schematic diagram of the spin rotation and spiral direction is shown in Figure 2.10.

For $BiFeO_3$ single crystals, the antiferromagnetic spin order is not homogenous at microscopic level. The unusual magnetic spiral arrangement in $BiFeO_3$ was reported by Sosnowska *et al* [49,55] using neutron diffraction studies and proposed that the material has a modified G-type antiferromagnetic structure where the spin of Fe^{3+} ion is subjected to a long-range modulation. The studies revealed a spin structure that is disproportionately modulated and the spin structure manifests itself as a cycloid with a long wavelength λ of $\sim 600 \pm 20$Å. The antiferromagnetic dipole moments vector is averaged to zero over λ, hence the induced magnetization (*M*) under an applied external field (*H*) is very small. This perhaps is the main root cause why the BFO does not generally exhibit a detectable magnetism in its bulk form or nanostructures in contrast with other iron-based materials. However, by the application of high magnetic field (H > 18Tesla), the antiferromagnetic spiral moments was destroyed and induced a phase transition from the spatially modulated AFM spin structure to a spatially uniform antiferromagnetic. This phase transition is accompanied with the onset of a linear magnetoelectric effect and a weak ferromagnetic moment.[56,57]

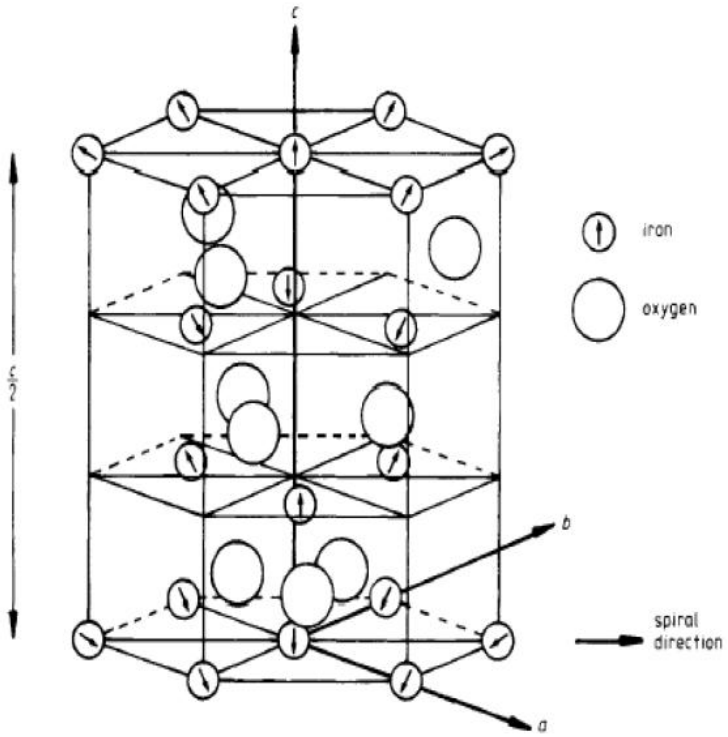

Figure 2.10 A portion of the $BiFeO_3$ lattice in hexagonal frame of reference with the arrows indicates the direction of Fe^{3+} moment. Figure adapted from Sosnowska *et al.*[55]

2.4.4 Multiferroicity in the $BiFeO_3$ (Ferroelectric/Antiferromagnetic Behaviour)

In tandem with its specific crystal structure, the BFO exhibits unique properties especially its superior electrodynamicity. Under its Curie temperature (T_c , Figure 2.11) of about 1100 K,[51] the BFO shows simultaneous piezoelectricity, pyroelectricity and ferroelectricity along its polar axis ($<111>_r$). Based on the works by Rovillain,[58] the linear piezoelectric coefficient of the BFO is d_{33} = 16 pm/V, about 6 times greater than that of quartz. A pyroelectric coefficient of about 3 x 10^{-3} $\mu C/cm^2K$ was observed by Rakov, comparable with that of $LiNbO_3$.[59] The ferroelectricity of the BFO was once considered to be very weak, however it has

been measured to have between 0.6 C/m^2 in $[001]_c$ and 1.0 C/m^2 in $[111]_r$ from a single crystalline thin film[51] and a bulk BFO.[52,53]

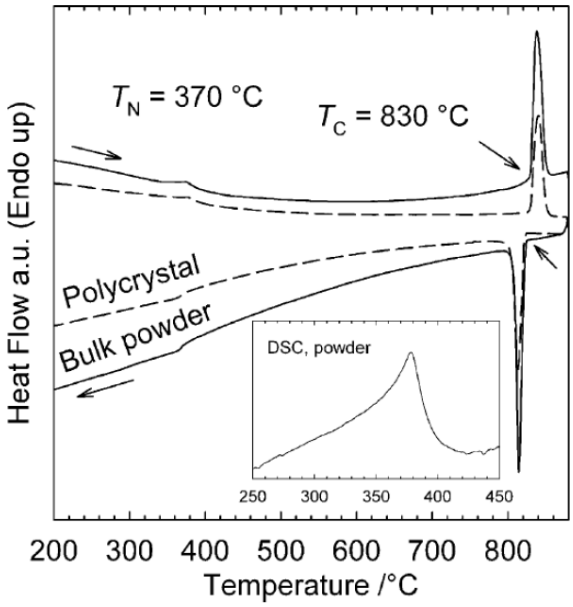

Figure 2.11 Differential thermal analysis measurement shows the antiferromagnetic – paramagnetic transition temperature (T_N, 370 ℃) and ferroelectric – paraelectric transition temperature (T_c, 830 ℃). Inset: The Differential Scanning Calorimetry measurement indicating the peak of the phase transition from antiferromagnetic to paramagnetic. (Figure adapted from Selbach *et al*[60])

Below its Neel temperature (T_N) of about 643 K (Figure 2.11), the BFO has the short range magnetic ordering that belongs to a G-type antiferromagnetism with a magnetic point group 3*m*. The multiferroic nature of the BFO is of marked distinction from the classic theory in which ferroelectricity originates from the B-sites ion with d^0 electron, whereas the magnets require d^j elelctrons ($j \neq 0$).[61] Indeed, it is now generally acknowledged that the polarization comes from the A-site Bi^{3+} lone pair $6s^2$ electrons that distort the system symmetry and hence, ferroelectricity while magnetization stems from the B-site Fe^{3+} through antiferromagnetic coupling of two adjacent crystals (Figure 2.8). Although they arise from different sources, a

magnetoelectric coupling coefficient is established to be around 3 V/cmOe across a temperature range of 77-300K.[62] Hence, $BiFeO_3$ is a multiferroics material that exhibits the coexistence of ferroelectric and antiferromagnetic (AFM) orders.

Among all the multiferroic materials that have been studied so far, $BiFeO_3$ (BFO) has received great attention due to its high ferroelectric Curie temperature (T_c ~ 1103 K) and the antiferromagnetic (AFM) Néel temperature (T_N ~ 647 K). The BFO is one of the prime candidates for room-temperature magneto electric applications.

2.5 Synthesis of the $BiFeO_3$

$BiFeO_3$ was studied by Smolenskii, a pioneer scientist in the study of the BFO. He failed to obtain single crystals of the BFO successfully and the ceramic samples obtained were found to be poor insulators even by doping other ions into both A and B sites of the lattice.[63,64] Strong research interests on the BFO have been revived since 2003. Ramesh's group observed a large remnant polarization together with strong ferromagnetism from a BFO on SrTiO3 epitaxial thin film[51] and the result was later confirmed by Lebeugle *et al*.[52,65,66] through the measurements from the single crystals. The BFO was then believed to be the only possible candidate that shows simultaneous large ferroelectricity and antiferromagnetism effect at room temperature. This finding led to a series of studies on this area from around the world and many more novel properties of the BFO were discovered including photovoltaic effect,[67] light-induced photostrictive effect,[68] and controllable ferroelastic switching.[69]

Earlier researches have mostly focused on bulk ceramics single crystals and thin film samples of the BFO to reveal its physical properties, inspired by the potential for information storage in spintronic devices and sensors.[70] The traditional solid state reaction to produce bulk ceramics, the BFO uses ground oxides or carbonates of metal components, however these proved to be futile when subjected to thermal treatment around 800-830 ℃. In a solid state route where Bi_2O_3 and Fe_2O_3 were mixed in the high energy planetary ball milling machine and milled from 5 hours to 120 hours duration and unreacted Bi_2O_3/$Bi_2Fe_4O_9$ phases are removed by washing in HNO_3.[71] A 'rapid liquid sintering" technique with a balanced stoichiometric ratio of Bi_2O_3 and Fe_2O_3 powder as starting materials was used to synthesis phase-pure the BFO successfully by rapidly heating the mixture of Bi_2O_3 and Fe_2O_3 to 1153 K followed by 7.5 minutes of soaking time and rapid cooling to an ambient temperature.[72]

The major drawback in the research of the BFO bulk and thin films is impurities and this also applies to the development of the BFO nanostructures. In practice, most studies have failed to synthesize the single phase BFO samples without generating secondary phases such as $Bi_{25}FeO_{39}$ and $Bi_2Fe_4O_9$. The initial solution was to react with excess Bi_2O_3 followed by leaching with diluted nitric acid to wash away other secondary oxides and the residual Bi_2O_3.[73] Later a protective atmosphere such as argon and nitrogen during the heating process was used to reduce the secondary phases.[74] Selbach *et al.* [75] Argued that the BFO is metastable in air with respect to $Bi_2Fe_4O_9$ and $Bi_{25}FeO_{39}$ based on thermodynamic factors. Hence, a decomposition process will be as follows:

$$49\ BiFeO_3 \rightarrow 12Bi_2Fe_4O_9 + Bi_{25}FeO_{39} \qquad \text{Equation 2.13}$$

The phase diagram for the Bi_2O3/Fe_2O_3 system has been mapped out[76,77,78] and is shown in Figure 2.12. Bi_2O_3 is widely known to evaporate easily when heated at a high temperature. Thus, this will lead to the generation of iron-rich phases such as Fe_2O_3 or even Fe_3O_4 [79, 80]

$$2\ BiFeO_3 \rightarrow Fe_2O_3 + Bi_2O_3 \qquad \text{Equation 2.14}$$

$$12\ BiFeO_3 \rightarrow 4\ Fe_3O_4 + 6\ Bi_2O_3 + O_2 \qquad \text{Equation 2.15}$$

In this situation, the properties of the sample, especially the magnetic characteristics, will be strongly affected by these impurities.[79] To minimize such problems, careful optimization of the growth parameters including thermodynamic and kinetic conditions would be required. Reaction in hermetic sealed systems or a low temperature is favourable in obtaining phase-pure perovskite samples.

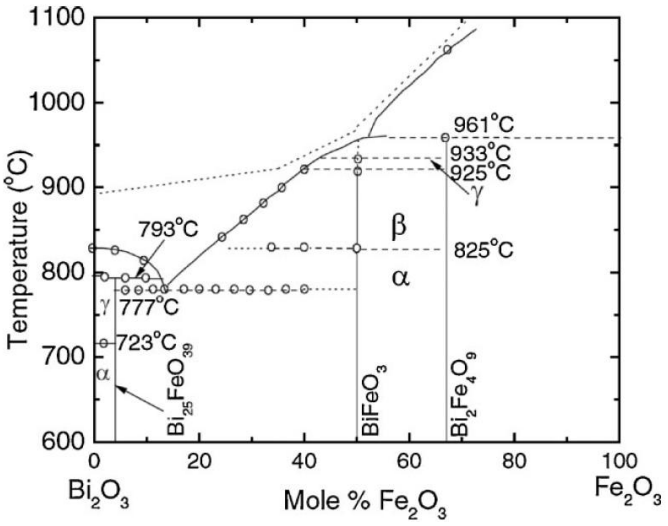

Figure 2.12 compositional phase diagram of Bi_2O_3-Fe_2O_3 system.[79]

There has been growing activities working on the BFO nanostructures as an effective way to fully understand the chemical properties and applications of the material. Recent research has focused on synthesizing nanostructures of the BFO such as nanoparticles, nanorods, nanowires, nanotubes and nanocubes with reference to their size-dependent physical and chemical properties.

2.5.1 Synthesis of Nanostructures $BiFeO_3$

Initially objectives of the synthesis approaches are for the pursuit of monodispersity, high stability and crystallinity with controllable morphologies, and significant progress has been made in the case of perovskite bismuth ferrite, BFO. Several techniques have been employed to produce $BiFeO_3$ nanostructures. The main drive behind each technique was to obtain the highest purity at the lowest possible temperature with a process to make cost effective materials for industrial applications. The traditional solid state reactions method mentioned earlier[71,72,73] have the following drawbacks; they require a high sintering temperature (>800˚C),[71,72] leaching in HNO_3 to wash the secondary oxide phases and the residual Bi_2O_3,[73] and did not yield the $BiFeO_3$ particle in the nanoscale. Due to these drawbacks, new wet chemical approaches have gained interest and become the focus of the BFO materials development recently. The synthesis of various BFO micro- and nano-structures using the wet chemical methods is highly controllable and tunable.

2.5.1.1 *0D* $BiFeO_3$ Nanostructures (Nanoparticles)

A broad range of wet chemical methods have been applied as synthetic approaches to generate BFO nanoparticles in the past years.[81-86] Among them is the solgel method.[81] Hydrated bismuth nitrate and iron nitrate salts were dissolved in 2-methoxyethanol and acetic acid to form a solution. The addition of chelating agents to form a homogeneous polymeric precursor, ageing of the precursor to form dried gel and finally followed by annealing at 600 ℃ in Air and N_2 environment to yield nanoparticles.[81] The sol-gel method exhibits a number of merits: (a) the procedures involved are simple, resulting in high reproducibility; (b) the method is cost effective due to the low sintering temperature with respect to the solid state reaction (c) the different particle sizes can be obtained by varying the sintering temperatures. However, the sol-gel process generally pose limitations such as a long synthetic duration (up to several days or even weeks) to form the dried gel, and the toxicity of some emergent gases (such as NO_x from the decomposition of metal nitrates) along with a large volume of shrinkage during the decomposition of the chelating compound.[82] These limitations have led to the search for other wet chemical approaches towards the BFO nanoparticles synthesis. For instance, the hydrothermal method was commonly used to prepare $BiFeO_3$ nanoparticle where Bi-Fe ionic solution was subjected to heat at around 200 ℃ and vapour pressure in the Teflon lined stainless steel autoclave vessel[83] yielding a sub-micron BFO particle. In this type of closed reaction system, the crystallization temperature will be effectively decreased due to autogenous pressure.

Hardy *et al*.[84], used an aqueous sol–gel route for the preparation of $BiFeO_3$ nanoparticles based on citrate complexes without toxic ethylene glycol. This is a water based wet chemical synthesis with ecological and economic advantages over solvent based routes to obtain phase-pure $BiFeO_3$. Bi(III) citrate ($BiC_6H_5O_7$), Fe (III) citrate hydrate ($FeC_6H_5O_7.H_2O$), Fe(III) nitrate nona hydrate ($Fe(NO_3)_3.9H_2O$) and citric acid are used as starting precursors for the synthesis. The ration between concentrations of metal ions to citric acid is equal (1:1 ratio). 10 % Bi excess is added to compensate for the bismuth loss during the thermal treatment. Xue *et al*.[85] reported the synthesis of the BFO nanoparticles by a solution evaporation process. Equimolar of $Bi(NO_3)_3.5H_2O$ and $Fe(NO_3)_3.9H_2O$ were dissolved in the diluted nitric acid to form a transparent solution. EDTA was added to the above solution with 1:1 mole ratio with respect to the metal nitrates followed by heating at 130 ^{0}C under the constant stirring in an oil bath until all liquids evaporated from the solution. The resultant powder was collected and sintered for around 5 minutes in air at different temperatures (300 – 600 ^{0}C) using the rapid thermal processor with a heating rate of up to 80˚C/s to obtain $BiFeO_3$ nanoparticles.

Co-precipitation technique is a low cost and simple method in general. The method has the main advantage of a significantly lower synthesizing temperature. However, the disadvantage of this technique is the impurity phase's formation and made this technique unpopular. Recently Ke *et al.*[86] investigated the synthesis of the BFO using a co-precipitation method with various parameters, but could not get rid of the impurity phases of $Bi_{25}FeO_{39}$.

Jiang *et al.*[87] synthesised $BiFeO_3$ powders with the Pechini method with polymer precursor resin. A mixture of cations is formed in an organic complexing agent such as citric acid or ethylene diamine tetra acetic acid (EDTA) and ethylene glycol solution. The cations chelate and a polymeric resin forms and eventually decomposes at 573 K. There are two reactions involved, the first is a complex formation between the citric acid or EDTA and metals, and the second is a sterification between the citric acid or EDTA and ethylene glycol (EG) to form polymeric organic net with the aim to reduce any segregation of the cations. $Fe(NO_3)_3.9H_20$ were dissolved in the citric acid solution and was stirred and heated at 70 ^{0}C for 3 hours to form a sol, and the pH value is adjusted using aqueous ammonia. Dissolved $Bi(NO_3)_3$ .5 H_2O was then slowly added to the Fe – sol to prevent the precipitation of bismuth salts. The sol was dried at 130 ^{0}C in an oven for 12 hours to form a gel and was slowly heated to 700 ^{0}C for 1 hour to obtain $BiFeO_3$.

One of the most widely used and useful method of preparation of the BFO is the combustion synthesis route using a fuel. The fuel used may be glycine , citric acid, urea or sucrose.[88, 89, 90] Farhadi *et al,*[88] synthesized $BiFeO_3$ using sol-gel autocombustion technique with sucrose as the fuel resulted in the formation of pure (single phase) rhombohedral crystal structure and nano-size $BiFeO_3$ with the particle size observed around 40 nm. Combustion synthesis technique has become one of the most popular methods for the preparation of a wide variety of nanomaterials[91] due to its simplicity, effectiveness, low cost, the broad applicability range, and the high temperature self-purifying feature. An aqueous solution of a metal nitrates ions acting as oxidizer, and fuel such as glycine, urea or citric acid is

heated up to moderate temperatures. Upon dehydration, the strongly exothermic redox reaction took place and provides the energy for the formation of the oxide.

2.5.1.2 *1D* $BiFeO_3$ Nanostructures

Since the first discovery of carbon nanotubes by Russian scientists Radushkevich and Lukyanovich in 1952,[92,93] 1D nanostructures have received great research interest. The few first works on the BFO 1D nanostructure were reported by Park *et al.*[94] who used a template synthesis involving sol-gel techniques. Pressure was applied on the precursor sol on porous anodic alumina template (AAO), followed by annealing and immersion in NaOH solution to remove the alumina template, leaving out the BFO nanotubes with diameters of around 200-300 nm and lengths up to 50 μm.

Zhang *et al.*[95] used an Anodized Aluminum Oxide (AAO) template combined with a similar sol-gel technique to synthesize the BFO nanotube arrays. The nanotube morphology had diameters about 250 nm and lengths of about 6 μm (Figure 2.13). Electrical measurement on these BFO nanotubes arrays gave a hysteresis loop and the array was proved to be ferroelectric. Li *et al.*[96] discovered the BFO nanotubes Y- junctions shape using similar techniques by Zhang *et al.*[95] Gao *et al.*[97] synthesized random BFO nanowires with the similar technique as Zhang et al and Li et al, obtained nanowires of around 50 nm in diameter and 5 μm in length and the measured optical bandgap of the nanowires is 2.5 eV.

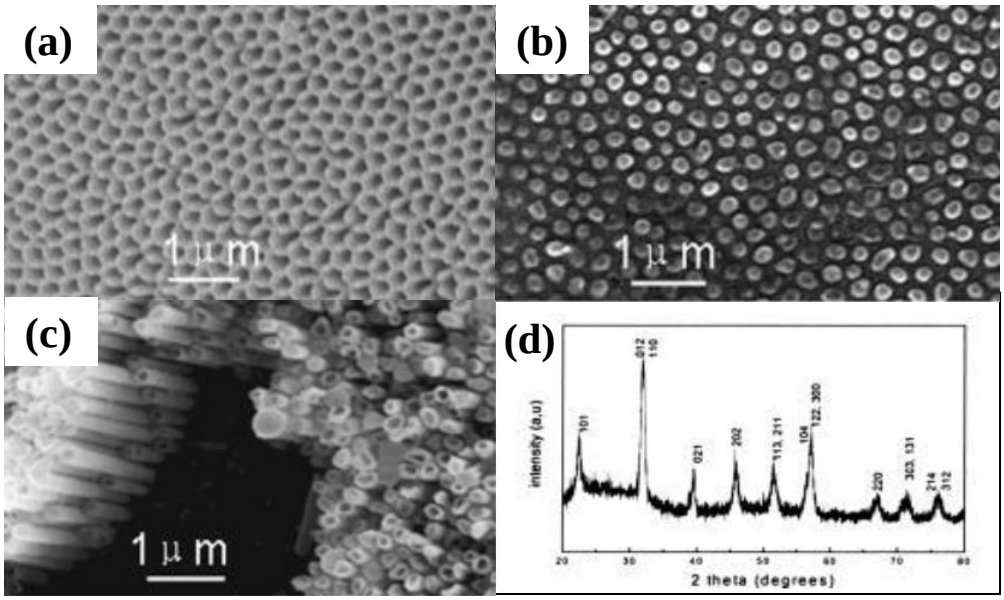

Figure 2.13 Micrograph images of Anodized Alumina (AAO) template and synthesized the BFO nanotubes; (a) AAO template, (b) AAO template filled with the BFO nanotubes, (c) Arrays of BFO nanotube tilted view, and (d) The XRD pattern of BFO nanotube arrays.[95]

Despite the complex procedures, one major obstacle for template-based synthesis is the elimination of the template after annealing, which so far is inadequate using the wet chemical etching.[95,96,97] The inter-diffusion during the heating process has often led to a certain amount of amorphous content in the final products. Hence, other chemical routes have been tested. Xie *et al*.[98] published results of nanocrystalline BFO nanofibres *via* sol-gel combined with an electrospinning technique. However, the pure perovskite phase seemed slightly difficult to obtain. Zhang *et al* [99] reported a facile polymer-directed solvothermal route which caused the BFO nanoparticles to segregate into rod-like structures due to the interaction between polymer molecules.

2.5.1.3 Complex/Special $BiFeO_3$ Nanostructures

Recently, there is an increased interest on the tunable synthesis of the BFO special nanostructures[100] to open up the possibility of further studies and applications of the BFO complex or special nanostructures. Currently, the BFO with special/complex morphologies, such as submicrometer-sized spindles[107], microplates[101], micro- and nano-cubes and microspheres[100,105,106], polyhedral particles[102], nanoflakes[103], and flower-like particles[104] have been synthesized via hydrothermal and solvothermal routes. Liu *et al.*[100] develop a tunable hydrothermal technique and obtained BFO microspheres, micro-cubes and submicron particles by controlling the annealing duration and the KOH mineralizer concentration. Recently, Joshi *et al.*[105] and Li *et al.*[106] employed the microwave assisted hydrothermal technique to synthesize the BFO cube-like structures with sizes ranging from 50 nm to 200 nm and the studies are mainly focused on the optical and photocatalytic properties of the BFO nano-cubes (Figure 2.14).

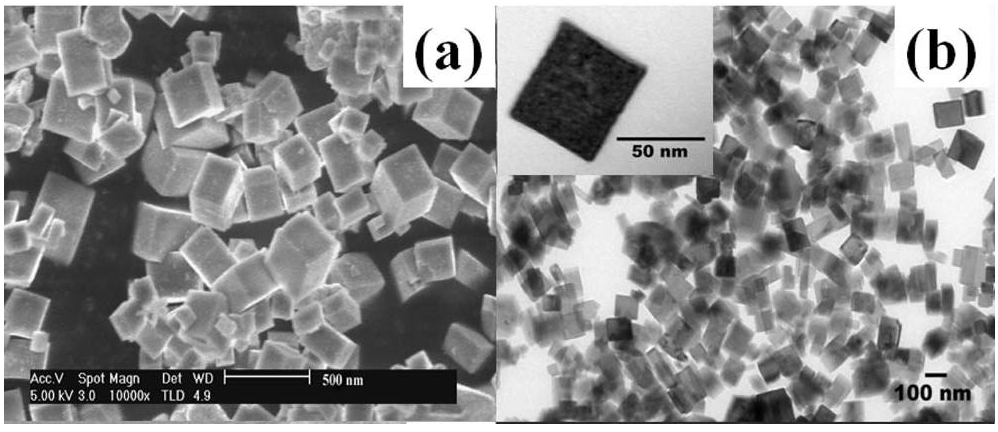

Figure 2.14 (a) SEM image of $BiFeO_3$ nanocubes. (b) TEM image of $BiFeO_3$nanocubes.[105]

Han *et al.* developed a tunable hydrothermal synthesis of a large family of bismuth ferrites with various morphologies, including sillenite- and perovskite-type compounds.[107] Single-crystal $BiFeO_3$ elongated submicrometer spindle shaped particles with lengths of around 600 nm and a thickness of about 300 nm can be selectively synthesized.

2.5.2 Doping in $BiFeO_3$

The doping of BFO with elements such as strontium (Sr),[108] manganese (Mn), lanthanum (La),[109] niobium (Nb),[110] gadolynium (Gd) etc have been made in attempt to improve the BFO properties. The dopant can be at the A site or the B site of ABO_3 structure, the A site being the edges of the perovskite cell and the B site being the centre of the perovskite cell. The crystal structure, electronic structure and magnetic properties of Strontium (Sr) - doped $BiFeO_3$ was reported by Li *et al.*[108] Sr-doping increases the oxygen vacancy concentration and $Bi_{1-x}Sr_xFeO_3$ behaves like an antiferromagnet and a weak ferromagnet simultaneously. Palkar *et al.*[109] studied the effect of Mn doping to La-modified $BiFeO_3$ and found that a small enhancement in magnetization was observed but ferroelectric properties were not affected by Mn substitution. Jun *et al.*[110] prepared highly resistive $BiFeO_3$ ceramics by Nb doping and studied their electric and magnetic properties. They reported a very low remnant polarization of 0.15 C/cm^2.

Mazumder *et al.*[111] prepared Pb doped $Bi_{1-x}Pb_xFeO_3$ ceramics using a simultaneous precipitation synthesis technique followed by conventional sintering. They found that improvement in the sintered density and dielectric property with

the Pb doping. The typical non-lossy ferroelectric loops have been observed in the $Bi_{1-x}Pb_xFeO_3$ ceramics at room temperature (Figure 2.15), in contrast to typical lossy loop of $BiFeO_3$.

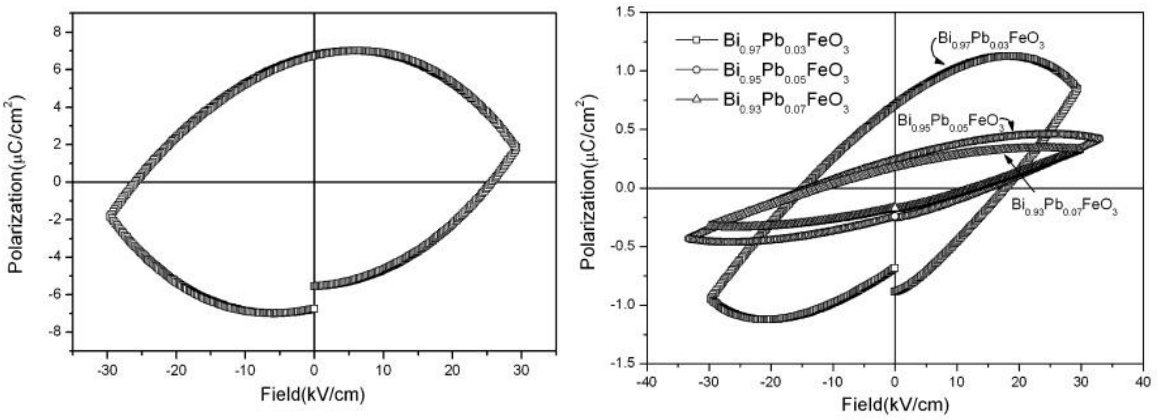

(a) (b)

Figure 2.15 Ferroelectric polarization hysteresis loops of (a) pure and (b) Pb (Lead) doped $BiFeO_3$ samples.[111]

One of the important goals in multiferroics is to establish a strong coupling of magnetic ordering at room temperature, which can be achieved by chemical substitutions at both the Bi and Fe sites.[112,113,114] Accordingly, Li *et al.*[108] has shown that Sr doping (at the Bi site) resulted in samples being oxygen sub-stoichometric, and with increasing the Sr concentration, transition to a $SrFeO_3$ phase accompanied by a decrease in magnetization. Komchenko *et al.* [115] have observed a similar behaviour in the Ca- and Ba- doped $BiFeO_3$ samples without any enhancement in magnetization. On the other hand, Pb^{2+} doping in the $BiFeO_3$ showed weak ferromagnetism, with an increase in magnetization. Wang *et al.*[116,117] observed that the Sr substitution in the $BiFeO_3$ showed an absence of Fe^{4+} and also the Ba substituted $BiFeO_3$ exhibited ferromagnetism and ferroelectricity simultaneously. Kothari *et al.*[118] has shown that the Ca doped $BiFeO_3$ materials show a structural

transformation (rhombohedral to triclinic) and the coexistence of ferromagnetism and ferroelectricity at room temperature with this material.

Modifications of the properties of multiferroic $BiFeO_3$ by substituting Fe with Mn and Bi with La have been investigated by Sahu *et al.*[119] They demonstrate the increased in magnetization property as indicated by hysteresis loops as well as improved dielectric properties. Magnetization at low temperatures (T=10˚K) was increased with the increase in Mn doping, the highest value being found in $BiFe_{0.7}Mn_{0.3}O_3$ with a coercive field (H_C) of 1094 Oe and a remnant magnetization (M_r) of 24 emu/mol and also a distinct magnetic hysteresis loop was observed for the $BiFe_{0.7}Mn_{0.3}O_3$ composition. The ferroelectric transition temperature of the Mn doped BFO ($BiFe_{1-x}Mn_xO_3$) is lower than that of the $BiFeO_3$, dropped from 1110˚K for x = 0 to 933˚K for x=0.3. The Gd-doped $BiFeO_3$ showed the coexistence of ferroelectricity (maximum polarization of 0.80 $\mu C/cm^2$) and magnetism (maximum magnetization of 0.2 emu/g) at room temperature according to the study by Uniyal *et al.*[120]

Nalwa *et al.*[121] demonstrated that Sm-doped $BiFeO_3$ showed an improved polarization but leakage current increased by an order of magnitude. The Sm-doped $BiFeO_3$ exhibits a remnant polarization of 0.60 $\mu C/cm^2$ and a coercive field of 17.7 kV/cm, but the $BiFeO_3$ sample shows a smaller hysteresis loop with a remnant polarization of 0.30 $\mu C/cm^2$ and a coercive field of 9.2 kV/cm. Cheng *et al.*[122] concluded that the La doping in the $BiFeO_3$ exhibited a phase transition leading to an improved magnetization, and the magnetic moment of the samples is greatly improved with increasing of the La doping content in $BiFeO_3$. The magnetic

moment of $BiFeO_3$ measured at 2000 Oe field in this experiment is 0.01 emu/g at room temperature, while the values are 0.016 and 0.042 emu/g for the $Bi_{0.9}La_{0.1}FeO_3$ and the $Bi_{0.8}La_{0.2}FeO_3$, respectively. Zhang *et al.*[123] has shown that the La doping enhanced the magnetization property and the remnant magnetization increased with the La doping concentration to as high as 0.04 emu/g.

2.6 Bismuth Ferric Oxide ($BiFeO_3$) as Photocatalyst

2.6.1 Photocatalysis

Semiconductor photocatalysis, which provides a promising method for the chemical conversion of solar energy, has been the many research focus because of its application for the destruction of chemical contaminants and water splitting.[124,125] The basic principle of the semiconductor photocatalysis involves photo generated electrons ($e-$) and holes ($h+$) that migrate to the surface acting as redox sources for the destruction of the pollutants when a high energy incident light (photon energy) irradiated on the semiconductor surface and causing excitation of the charge carriers in the semiconductor. Photons of sufficient energy ($> E_{gap}$) are needed to excite e- & h+ pairs across the band gap. The photo-generated electrons and holes can take part in the REDOX chemical reactions as shown in the illustration below (Figure 2.16).[126]

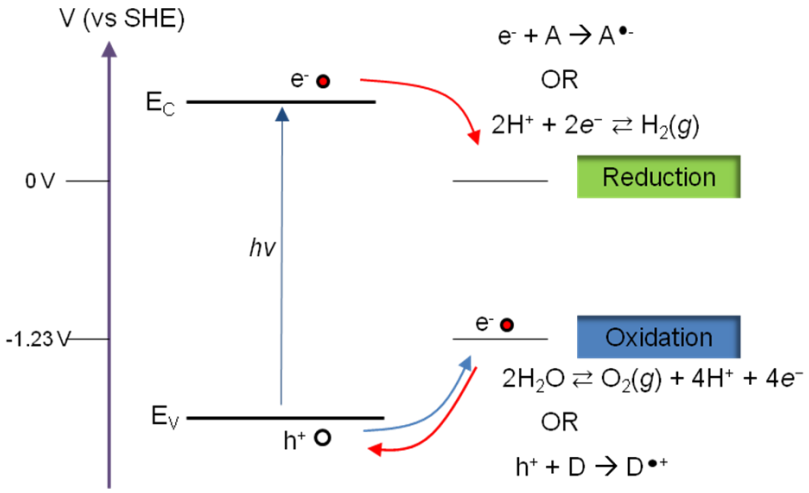

Figure 2.16 REDOX reactions from the photo-generated electrons and holes[126]

There are a few scenarios that would take place for photogenerated electrons in conduction-band: (1) it can combine with the holes in valence-band and dissipate the energy as heat, or (2) the photogenerated electrons get trapped in metastable surface states, or (3) react with charge species (electron donors and electron acceptors) that adsorbed on the semiconductor surface or within the vicinity of electrical double layer of the charged particles.[125] The valence band holes are powerful oxidants (+1.0 to +3.5V vs NHE depending on the semiconductor and pH), while the conduction-band electrons are good reductants (+0.5 to -1.5V vs NHE).[127] If there is a suitable scavenger or surface defect state available to trap the electron or hole, recombination is prevented and redox reactions may occur. The photogenerated electrons and holes will recombine within a few nanoseconds and dissipate the stored energy if there is no suitable electron and hole scavengers.[128] Most organic photodegradation reactions utilize the oxidizing power of the holes either directly or indirectly. However, to prevent a build-up of charge one must also provide a reducible species to react with the electrons.

Upon in contact with an electrolyte containing a redox couple, the semiconductor Fermi level moves to equilibrate with the potential of the redox couple and establishes a Schottky barrier, creating built-in electric field. This built-in electric field will drive photogenerated e- and h+ in opposite directions, hence induces spatial separation between e- and h+ by causing the energy band bending at the solid-liquid interface (Figure 2.17).[126]

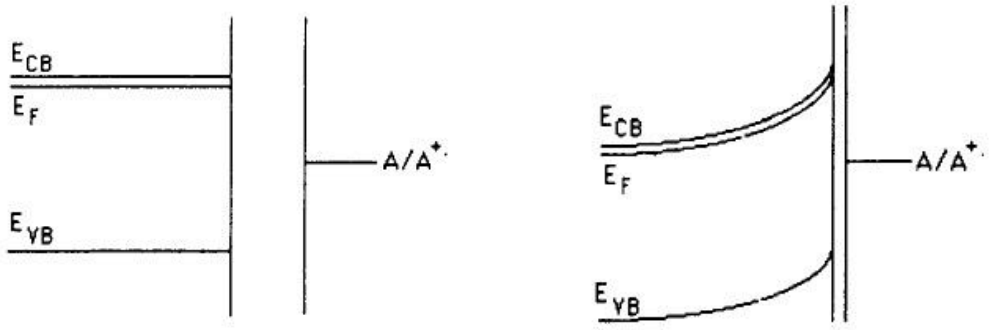

(a) (b)

Figure 2.17 Energy band diagram of an n-type semiconductor: (a) prior to interaction with an electrolyte solution and (b) in contact with an electrolyte solution.[126]

A photogenerated hole can react with an adsorbed species by interfacial electron transfer when it reaches the surface of the semiconductor. Thus, an adsorbed electron donor can be oxidized by transferring an electron to a photogenerated hole on the surface, and an adsorbed acceptor can be reduced by receiving an electron from the surface. The hole trapped by adsorbed electron donor generates a cation radical, D*+ and electron trapped by the adsorbed electron acceptor generates an anion radical, A*- (see Figure 2.16). If the rate of $\mathbf{D^{*+}}$ (reactive species) formation is kinetically competitive with recombination, then photo-oxidation will occur.

Photocatalysis creates a strong oxidation agent to breakdown the organic molecules to carbon dioxide and water with the presence of photocatalyst, light and water.[125] In order for the dye to be decolourised, photoexcited carriers must be able to migrate from catalyst to a suitable species that can subsequently react with the dye or interact directly with the dye, as indicated in equations 2.16-2.22 below.[126]

(1) $PC + hv \rightarrow e^-_{cb} + h^+_{vb}$ Equation 2.16

(2) $h^+_{vb} + OH^- \rightarrow OH^*$ Equation 2.17

(3) $e^-_{cb} + O_2\,ads \rightarrow O^{*}_{2}{}^-$ Equation 2.18

(4) $Dye + OH^* \rightarrow$ Degradation products Equation 2.19

(5) $Dye + e^-_{cb} \rightarrow$ Reduction products Equation 2.20

(6) $Dye + h^+_{vb} \rightarrow$ Oxidation products Equation 2.21

(7) $Dye^{+*} + O^{*}_{2}{}^- \rightarrow$ Degradation products Equation 2.22

Irradiating a photocatalyst with light exceeding the band gap produces photo-generated conduction band electrons and valence band holes. In the presence of a dye solution, dye is chemisorbed on the catalyst surface. The electrons can be directly transferred to the dye, thus it is possible to chemically reduce the dye. Alternatively the electrons can react with O_2 adsorbed on the surface to produce the oxide radical $O^{*}_{2}{}^-$ which can oxidize dye molecules. The holes either oxidize the dye directly or react with adsorbed H_2O to form H^+ or OH*. The oxide radicals produced by this step are very reactive and play a major role in the degradation of the dye molecules.[126]

Some of the commonly studied photocatalysts are TiO_2, ZnO, and CdS. Titanium dioxide (TiO_2) has become the benchmark photocatalytic measurements

due to its high photocatalytic activity. There are three crystalline forms of TiO_2, namely anatase, rutile, and brookite, however, anatase form is the most commonly used since it is the most photoactive.[129,130] Cadmium sulphide has also been extensively studied although not as photoactive as TiO_2 because of its good spectral response to the wavelengths of the solar spectrum. Like ZnO, CdS suffers from photocorrosion induced by self-oxidation.[131]

Traditionally, the wide band gap semiconductor; Titanium Dioxide (TiO_2) anatase phase with the energy band gap of 3.2 eV, is the most common photocatalyst materials used to photo-degrade the organic compound under Ultra-Violet (UV) light irradiation.[125,126] Hence, only about 4% of solar irradiation is suitable for the photoexcitation of TiO_2[7] rendering the process impractical. Other limitation of TiO_2 material is the low quantum yield, which is the ratio of the surface charge carrier transfer rate and the electron-hole ($e-$ /$h+$) recombination rate. The fast recombination rate of the photogenerated electron-hole pairs interrupts the commercialization of this technology.[7] However, the main advantage of TiO_2 is that it is photostable. For a photocatalyst to be stable, the band positions of the semiconductor must 'pinch' the electrolyte REDOX couples of available reactants and products as shown in figure 2.16, otherwise if the photocatalyst does not do this then it may be liable to photocorrosion.[132] This is a well-known problem for many narrow band gap semiconductors such as CdS.[131]

Recently, efforts have been made towards modifications of TiO_2 by doping to facilitate the activation of TiO_2 in the visible light region.[8,133,134,135,136] Ionic doping of TiO_2 with transition metal ions (e.g. Cd) has been reported to change the

electronic structure of TiO_2 which improves the electron trapping by introducing a charge trapping site and inhibits the electron – hole recombination which was observed in the shift in the absorption spectra.[135,136]

Other efforts to increase the photo-degradation efficiency have been made in the controlled synthesis of nanostructured composites such as TiO_2/ZnO and TiO_2/WO_3 creating heterogeneous nanocomposites, which will induce charge separation at the heterojunction that can significantly enhance the photocatalytic efficiency by decreasing the recombination rate of the photogenerated electron-hole pairs[137] as shown in the figure 2.18. However, this still does not remove the organic compound efficiently and is still dependent on the availability of ultra violet light.

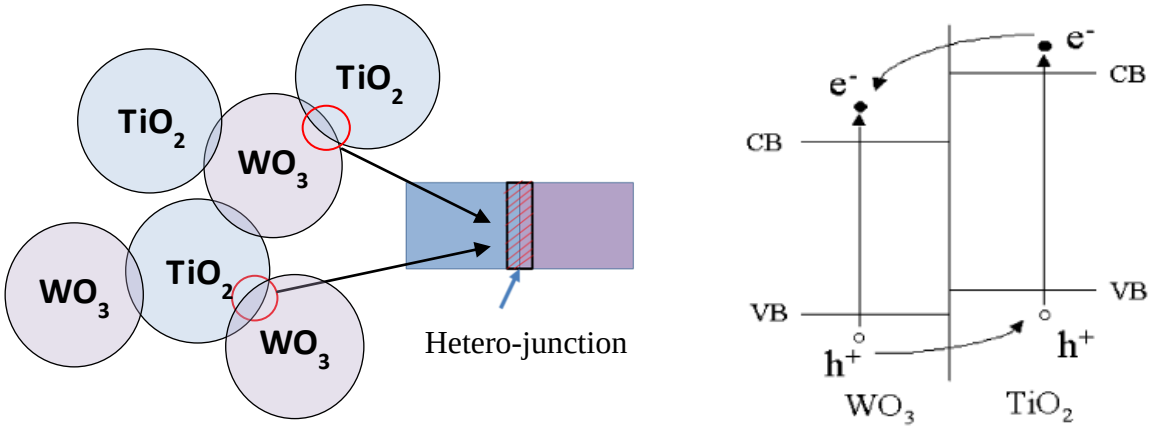

Figure 2.18 Composites of nano-TiO_2 and WO_3 by the mixing of TiO_2 and WO_3 aqueous sol creating heterojunction increased the charge separation[137]

2.6.2 Photochemical Reactions of Ferroelectric Material

Internal dipolar fields create charged surfaces on ferroelectrics that cause the photogenerated charge carriers to move in opposite directions, and is called the bulk

photovoltaic effect.[138,139,140,141,142] The electrons and holes move towards the different surfaces of the crystal and thus separate the oxidation and reduction sites.[11] Redistribution of electric charges and the formation of a double layer occurred when a semiconductor is in contact with another phase, such as liquid, gas, or metal.[7,126] The space-charge layers produced from the mobility of charge across a semiconductor-solution interface for an n-type semiconductor is illustrated in figure 2.19.[7,127] The flat band potential diagram of the semiconductor in the absence of a space charge layer is shown in figure 2.19(a) with a uniform distribution of charge. When negative charges exist at the semiconductor – solution interface, the majority electron carrier concentration at interface will be repelled from surface and become less than that in the interior of the semiconductor (Figure 2.19(b)). The space-charge layer formed is a depletion layer, and the bands bend upward toward the surface.

When positive charges exist on the interface (figure 2.19(c)), the n-type semiconductor majority carrier concentration of electrons near the surface within the region of the space-charge layer increased, and the layer is called the accumulation layer. The semiconductor bands near the interface will bend down as a result of the decrease of electron potential energy toward the positively charged outer layer.

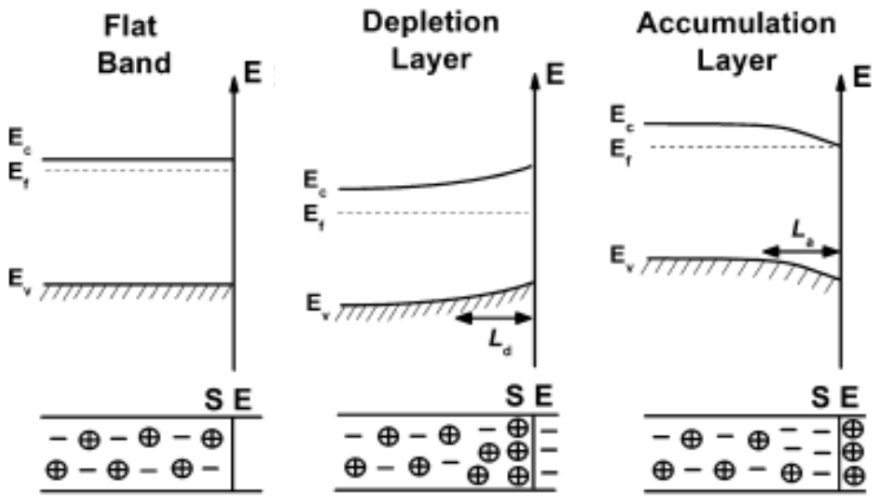

Figure 2.19 Formation of space charge layer and the bending of n-type semiconductor energy band at the semiconductor – solution interface showing (b) depletion of electron and (c) accumulation of electron.[127]

The energy bands bending at the interface determined the type of reaction that occurs on a ferroelectric surface. For conventional semiconductor solid, the band bending is a direct interaction of the charge mobile carriers' presence across the interface in ionic solution. However, the band bending nature for a material that has an internal field due to the displacement of ions in the crystal lattice, i.e. a ferroelectric, has some fundamental differences. The ferroelectric, either n or p-type does not generate bands bending in the same way as a conventional semiconductor, because the spontaneous depolarisation need to be screened and so the band bending at the ferroelectric surface is determined by this screening effect.[143] Hence, in ferroelectric materials the depolarising fields screen the surface charge by drawing electrons to the positive polarity surface region (termed as C+ face) forming accumulation layer and holes drawn to the negative polarity surface region (termed as C- face) forming depletion layer.[12,15,26] These regions of carrier

accumulation induce downward bending at the C+ face and upward bending at the C- face as shown in Figure 2.20 at the surface, resulting in spatially distinct REDOX chemistry.[14,15,144] Hence, reduction reaction occurs at the C+ face due to electron accumulation and oxidation reaction at the C- face due to hole accumulation[12] as seen in the illustration in figure 2.21. The separation of carriers by the depolarisation fields also suppresses recombination rates thereby increasing the carrier lifetimes. Evidence for this is provided by the long photo luminescence of up to 9 μs in $LiNbO_3$.[145]

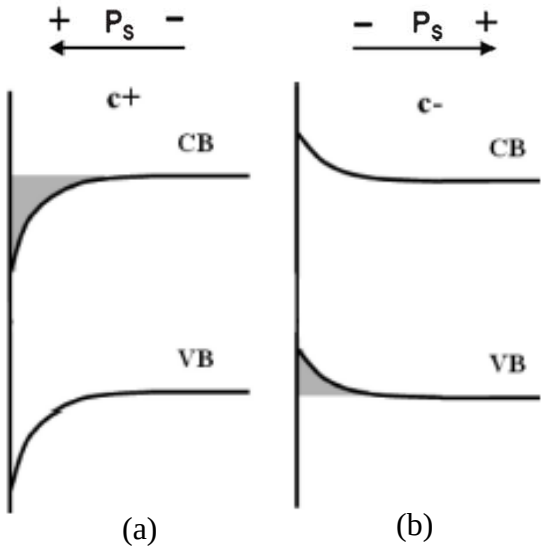

Figure 2.20 The structure of the energy band at the surface of the polarised ferroelectric. (a) The internal polarisation field causes downward bending in c+ domains (holes depletion). Thus, at c+ domains, the photo-excited electrons will be driven towards the surface and can participate in reduction reactions. (b) The bands bent upwards in the c- domains causing holes accumulation at the surface and can take part in the oxidation reactions at the surface of the ferroelectric.[15]

These intriguing properties of ferroelectrics have led to growing interest in their photochemistry. Selective deposition of metal nanoparticles on a wide range of

ferroelectric materials as catalyst including Barium Titanate, PZT and lithium niobate has been extensively investigated.[12,15,16,17,148,149] Ferroelectrics have also been used to drive photocatalytic reactions such as artificial photo synthesis[13,146] [13]and water splitting.[15,16] An investigation of different compositions of barium titanate to split water[147] showed the reactivity of the materials to increase with the strength of polarization.

This spatially selective photochemical reaction on a ferroelectric surface due to dipolar fields created by ferroelectric domains has been demonstrated by Kalinin *et al.*[148, 149] Biased Atomic Force Microscope tip were used to pattern to domains on the PZT surface and followed by photochemical deposition of Ag on the domain patterns, see figure 2.22, where silver positive ions were reduced at the C+ face where there is electron accumulation layer. Thus, they have proposed the spatially selective photochemical deposition of metals on ferroelectric domains to be a new way of producing nanostructures and a promising method for nanodevice integration.

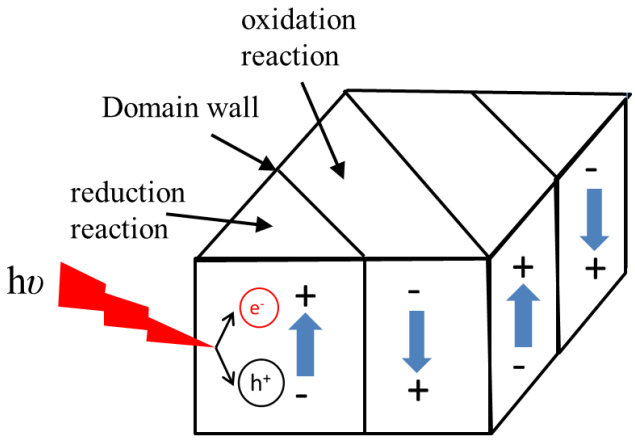

Figure 2.21 - Schematic diagram of the effect of internal polarizations on photochemical reactions of ferroelectrics.

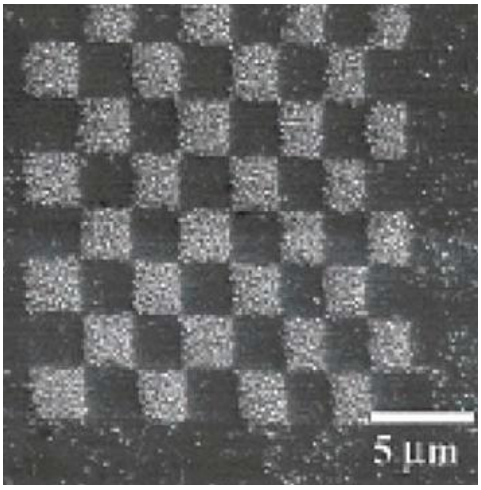

Figure 2.22 – SEM image of the chess board domain structure created with (PFM) Piezoresponse Force Microscopy corresponding with silver photodeposition pattern only at the c+ domains (positively polarized domains).[148]

2.6.3 $BiFeO_3$ as Visible Light Driven Photo-Catalytic Agent

Recently, $BiFeO_3$ has been examined as a photocatalyst in a visible-light region because of its small band gap value (2.2 eV).[10,97,150] Lou *et al.* [150] reported that the $SrTiO_3$-coated BFO core/shell nanostructures can produce H_2 under visible-light irradiation. Liu *et al.* further demonstrated that the BFO nanoparticles show significant degradation ability toward the photodegradation of methyl orange upon irradiation with visible light.[10] These studies suggest that BFO could be used as photocatalysts and optoelectronic devices operating in the visible-light region due to its unique optical and multiferroic properties. In addition, due to the presence of internal dipole of the materials, it is being established that ferroelectric materials can be highly photoactive with some exceptional properties.[15,31] Although the photocatalytic activity of BFO powders under visible light is mainly due to its small band-gap energy[97], attempts to understand the influence of other factors, such as their ferroelectric nature and weak ferromagnetic properties, are still being made.

Several works have been made on the BFO nanostructures which showed quite different properties from the bulk form. Recent research shows that the particle size greatly influence the Néel temperature T_N and the lattice parameters of the BFO.[151,152] Room-temperature ferromagnetic behaviour was observed in nanoscale BFO particles[153,154] unlike the antiferromagnetic characteristic in the bulk BFO.[55,155] The impact of the particle size on optical and photocatalytic properties of the BFO has been reported by Shun Li *et al.*[156] where the photo-degradation results reveal that the particle size has an influence on the photocatalytic activity of the BFO powders. In the BFO nanocrystals, the recombination opportunities of the photogenerated electron and hole pairs in the volume will be reduced compared to the bulk BFO, which can effectively move to the surface and degrade the absorbed organic pollutant. The decrease in the particle size also leads to a larger surface area, and thus increasing the available surface active sites.

Recently, a study has shown perovskite ferroelectric materials (PZT) can photocorrode.[157] Photochemical reaction of nitrate or chloride metal salts on a PZT surface and shows that there can be a metal deposition on positive domains or photodecomposition on negative domains. Shun Li *et al.*[158] and Luo *et al.*[159] also reported that as a visible light photocatalyst, the BFO lacks stability due to photo-corrosion on the surface of the particle. Hence, protection of the surface of the BFO nanoparticle by creating a heterojunction to alter the band gap of the BFO such as the core-shell structure of the TiO_2 coated BFO[158] and the $SrTiO_3$ coated BFO nanocomposites.[159]

The core-shell structured $BiFeO_3$ /TiO_2 systems reported by Shun Li *et al.* consist of two semiconductors in contact with each other and an electronic interaction occurs at their point of contact (heterojunction). The position of a valence band and a conduction band of the $BiFeO_3$ and the TiO_2 against the normal hydrogen electrode was calculated by *Shun Li et al,*[158] as shown in the figure 2.23. When the $BiFeO_3$ and the TiO_2 are in contact, creating heterojunctions that improve the photogenerated charge carriers lifetime by enhancing the charge separation, thus improving the efficiency of the photocatalytic activity. The separation of photogenerated electrons and holes induce redox reactions according to the relative potentials of the conduction and the valence bands of the two semiconductors and the redox potentials of the redox couples present at the interface.

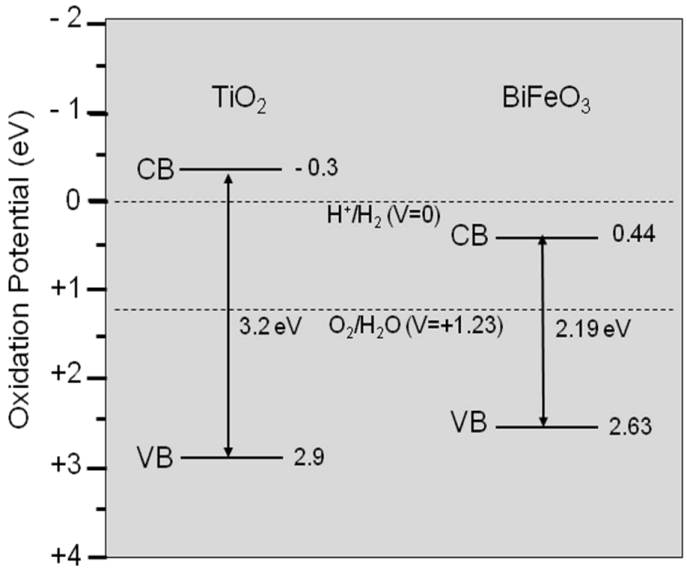

Figure 2.23 Schematic illustration for the calculated energy band level of titanium dioxide (TiO_2) and bismuth ferrite ($BiFeO_3$).[158]

Previous works on the photochemical degradation of organic dye compounds using the BFO as the catalyst has been done on Methyl Orange (MO),[10] Congo Red (CR)[156] and Rhodamine B (RhB)[160], however the ferroelectric nature or

multiferroic nature (in the case of the BFO) of the semiconductor has not been recognised or considered as important. Recently, there is an increasing interest of work on materials that demonstrates an internal electric field and a spontaneous polarization that behave in anomalous ways when photo-excited. For instance, the BFO thin film samples have recently been demonstrated to have shown spatially selective reduction oxidation (REDOX) chemistry by Rohrer *et al*.[161] Hence, it is therefore important to consider that the BFO is not only a semiconductor, but also a multiferroic material that demonstrates electron and hole separation due to the internal fields within the crystal lattice. The internal electric field of the multiferroic BFO exhibits a spontaneous polarisation that acts like an internal p-n junction ('self-junction') where the carriers are influenced by the field within, and are inherent to the material. This carrier's separation due to the internal polarisation largely determines the band bending at the interface and the surface where the mobile carriers can accumulate.[15]

In previous work, investigating the effect of Gd doping on the photocatalytic response of the BFO shows that the catalytic efficiency of the system increased when the band gap of the system increases from around 2 eV for the BFO to 2.2 eV for the $Bi_{0.9}Gd_{0.1}FeO_3$. However, the result did not consider that the change in the surface chemi or physisorption interaction of the catalyst with the dye or other molecules in the solution is the root cause for the enhanced performance. The increase in band gap producing an increased catalyst performance, however, is counter intuitive for a traditional photocatalyst.

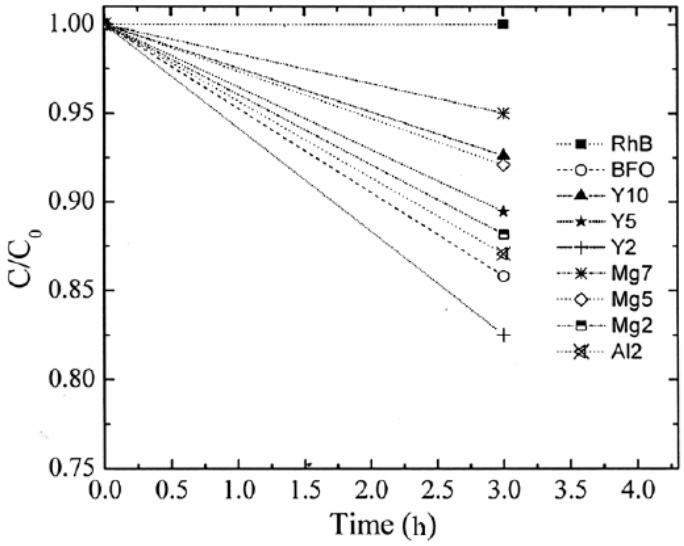

Figure 2.24 Photocatalytic degradation rate plot of the Rhodamine B on doped $BiFeO_3$ materials.[160]

Madhu *et al.*[160] used a sol-gel method to synthesise the doped BFO ($Bi_{1-x}M_xFeO_3$) with Magnesium (Mg), and Yttrium (Y) as the metal dopants. Cation doping showed that the substitution of the Bi metal did not result in a phase transition, and the doping substantially enhanced the magnetization leading to the samples exhibiting a ferromagnetic hysteresis loop. The photocatalytic improvement only shown on the $BiFeO_3$ doped with Yttrium with an 18% higher photodegradation rate compared to the undoped $BiFeO_3$ as shown in figure 2.24.

3 EXPERIMENTAL PROCEDURES

3.1 Synthesis of the $BiFeO_3$ Powder

One of the most widely used and useful methods of preparation of the BFO is the combustion synthesis route using a fuel. The precursor materials used for the synthesis of the BFO by the autocombustion route were commercially available reagent grade Bismuth Nitrate Pentahydrate ($Bi(NO_3)_3\ 5H_2O$) and Iron Nitrate Nonahydrate ($Fe(NO_3)_3\ 9H_2O$) salts with a purity of more than 99%, obtained from the International Laboratory. Nitric acid (HNO_3) with 70% concentration and De-Ionised (DI) water with resistivity of 18.3 MΩ were used to dissolve the salts raw materials. Reagent grade Glycine from Sigma Aldrich in a powder form with purity more than 99 % was used as fuel in the synthesis of the $BiFeO_3$ powder.

The $Bi(NO_3)_3.5H_2O$ and $Fe(NO_3)_3.9H_2O$ of 0.01 mol each were used in a proportion of 1:1 (molar ratio) to create 0.2 M solution. A solution containing 0.2 mol of nitric acid (25ml of 70% HNO_3) was mixed with 25 ml of DI water. The $Bi(NO_3)_3.5H_2O$ salts were dissolved in the nitric acid solution mentioned earlier and the $Fe(NO_3)_3.9H_2O$ were just dissolved in the DI water only. Once dissolved, both the bismuth and the iron ionic solutions were mixed together and the glycine fuel with molar ratios (Metal/Fuel) of 0.5:1, 1:1 and 2:1, respectively, was added into the Bi-Fe ionic solution and stirred until complete dissolution. The Bi-Fe with glycine solution were then heated up to 300 ℃ while continuously stirred until the solution dried and was followed by the auto ignition of the combustion and formed dark brownish flakes and was left heated for another ½ hour.

After the auto-combustion, the fluffy powder was ground before being placed in the furnace for annealing. Annealing was performed at 450 ℃, 550 ℃ and 650 ℃ with a heating rate of 5 ℃/minute and soaking durations of 3, 6, 9, 12 and 24 hours for each temperature.

The process flow summary is shown below:

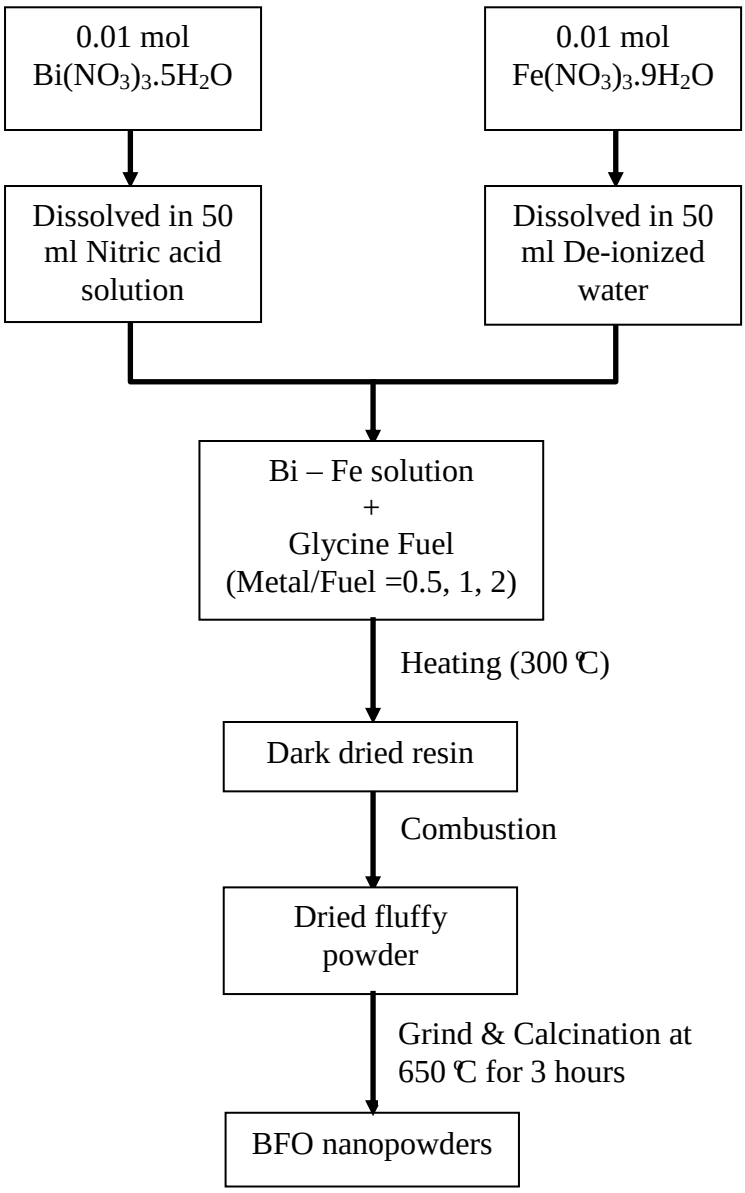

Figure 3.1 Process flow of synthesizing BiFeO3 nanopowders

3.2 Synthesis of the Doped-$BiFeO_3$ Powder

Dopants from the transitional metal group such as copper (Cu) and tungsten (W) were introduced into the BFO lattice by an in-situ doping process during autocombustion as shown in the process flow in figure 3.2. The synthesis process of the doped BFO powders was quite similar to the synthesis of pure BFO powder, except that there is an addition of metal salts of varying ratios into the Bi-Fe ionic solution before the heating process. Equimolar of Bismuth Nitrate Pentahydrate ($Bi(NO_3)_3\ 5H_2O$) and Iron Nitrate Nonahydrate ($Fe(NO_3)_3\ 9H_2O$) were dissolved in the nitric acid solution and the de-ionised water respectively. Glycine was added to the Bi-Fe solution with an equal molar ratio to the total metal ions molar content. If the initial Bismuth Nitrate Pentahydrate and Iron Nitrate Nonahydrate content is both 0.01 mol, then the total metal molar content is 0.02 mol.

Prior to heating the Bi-Fe solution, the metal salts (dopants) were added with varying ratios with respect to the metal molar content (0.02 mol). For instance, if the dopants are 0.5 atomic% the amount of metal salts added into the Bi-Fe solution is 0.1 mmol. The Bi-Fe ionic solution containing metal ion dopants are stirred until complete dissolution of the metal salts and then followed by the heating of the ionic solution until a dark dried resin formed followed by combustion to form a dried fluffy powder. The as-combusted dried fluffy powder were annealed in the furnace at 650℃ for 3 hours with 5℃/min heating rate to form the doped BFO powder.

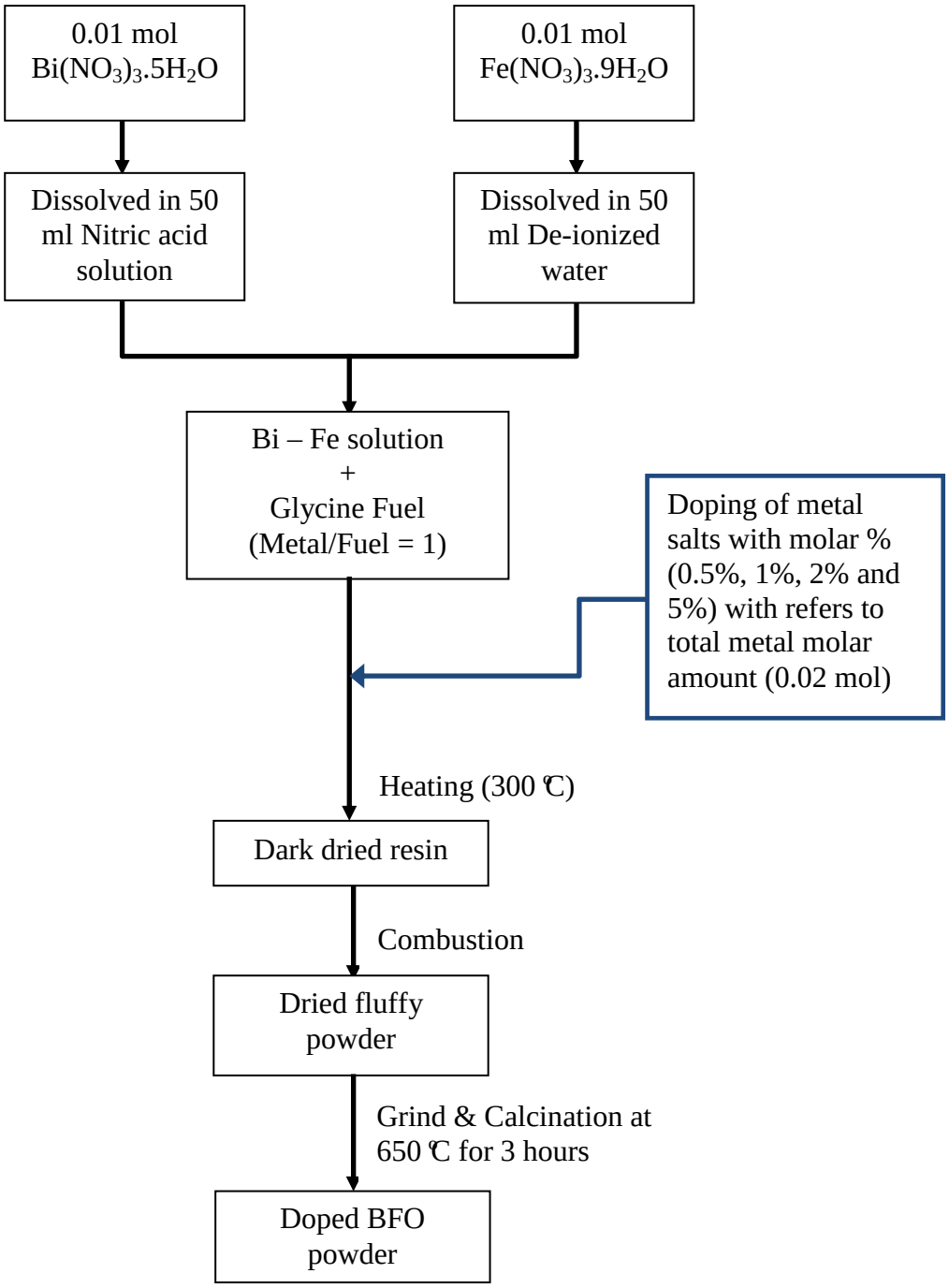

Figure 3.2 In-situ doping process flow for the BFO powder during the autocombustion process.

3.3 Synthesis of TiO_2-Coated $BiFeO_3$ Powder

In the preparation of the TiO_2 coated-BFO powder, pure BFO powder is first obtained by an auto-combustion process and reagent grade Titanium Tetra (IV) Iso-Propoxide (TTIP) from Sigma Aldrich is used as the precursor for the TiO_2 coating on the BFO powder surface. Different amounts of BFO powder and TTIP precursor with various molar ratios of $BiFeO_3$ to TiO_2 of **1:1**, **1:2** and **2:1** were prepared respectively. With respect to 1 g weight of the BFO powder (0.0032 mol), the TTIP amount was prepared accordingly to various molar ratios of the BFO: TTIP of 1:1, 2:1 and 1:2 and was poured into a beaker and added with a sufficient amount of acetylacetone followed by an addition of 100ml of ethanol into the same beaker. 1g of the BFO powder was mixed into ethanol – water solution and well stirred and dispersed with sonication, followed by the mixing of the TTIP solution into the dispersed BFO solution.

The pH level of the dispersed BFO-TTIP solution was adjusted to approximate pH 5 with diluted nitric acid under constant stirring. After 30 minutes, the BFO-TTIP solution was centrifuged to separate the powder and the remaining solution and was followed by the drying of the wet BFO powder at 80˚C until completely dried. The TiO2 coated BFO powder was extracted from centrifuge tube and annealed at 500˚C, with a rate of 5 ℃/min for 1 hour to crystallize the TiO_2 on the BFO particle surface. The process flow of the BFO coating is shown in figure 3.3.

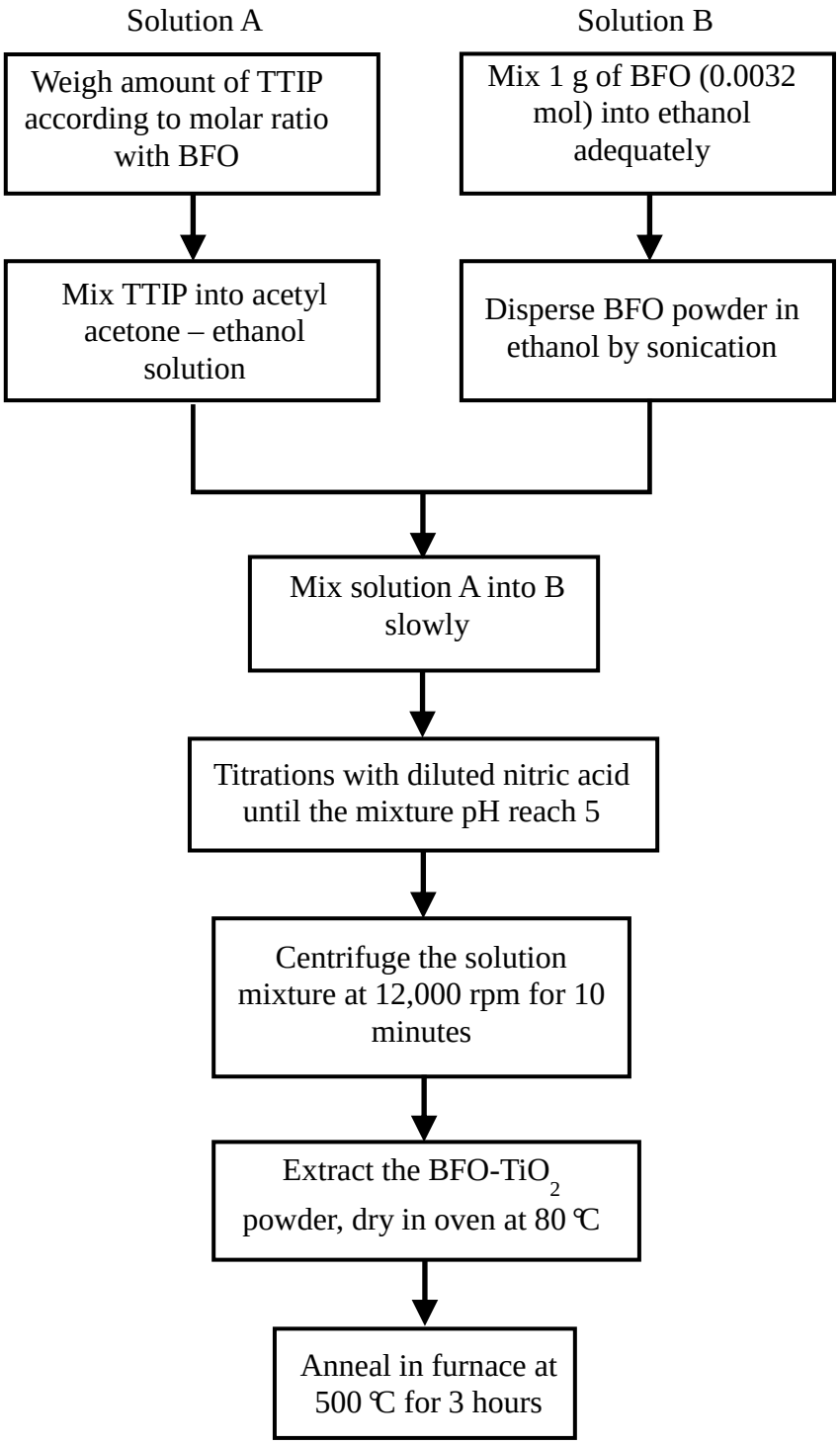

Figure 3.3 Process flow for the coating of the BFO with TiO_2 to create a hetero-junction structure.

3.4 Materials Characterization

3.4.1 Scanning Electron Microscopy (SEM)

The synthesized BFO nanopowders size and morphology was characterized using the Field Emission Scanning Electron Microscopy (FESEM JEOL-JSM7500F). Parameters for the SEM are as follows: the voltage setting used was 5 kV, 2 μA and a secondary electron was used. The BFO nanopowders were suspended in the de-Ionised water with **0.1 wt%** concentrations and were sonicated with 25 KHz frequency for around 30 minutes before dropping a drop of the suspension on the carbon tape and drying up the water. The specimens to be observed had to be platinum coated at 10 μA current for 100 seconds before the observation was performed.

3.4.2 Transmission Electron Microscopy (TEM)

For the Transmission Electron Microscopy (TEM) observation, the BFO nanopowders were dispersed in the ethanol and the copper grid (copper-support ultra-thin carbon film) was dipped into the above BFO nanopowders suspension and followed by the drying up of the water. The TEM used in the experiment was a JEOL model JEM 2010 and operating typically at 200 KV.

3.4.3 X-Ray Diffractometer (XRD) Analysis

The XRD technique is commonly utilized in the analytical characterization to gain crystallographic information of crystals. The main function of an XRD instrument is used to determine the phase structure, crystallographic structure and

the chemical composition. Since each material possesses its own unique XRD spectra, hence qualitative and quantitative analysis can be conveniently carried out by comparing the obtained sample XRD pattern to the standard database (ICDD). A wealth of information, such as lattice parameters and the particle size can also be extracted.

The phase analysis of the synthesized BFO powders was performed using X-Ray Diffractometer (XRD). The XRD is a versatile, non-destructive materials analysis method that provides detailed information about the crystallographic and microstructure of all types of natural and synthetic materials. The XRD pattern was obtained using the PANAlytical X'Pert Pro MPD advanced powder X-ray diffractometer using Cu-Kα = 1.54056 A° radiation, operating at 40 KV/30 mA. The scanning mode is θ - 2θ mode with 2θ range from 20 °to 70 °and a step size of 0.001. The sample holder used is made of glass materials.

The diffraction follows the Bragg's law:

$$n\lambda = 2d_{hkl}\sin\theta \qquad \text{Equation 3.1}$$

where n is an integer, λ is the wavelength of the X-ray, d_{hkl} is the lattice spacing between (hkl) planes and θ is the angle between the incident beam and (hkl) plane.

3.4.4 Optical Band Gap Determination

In determining the optical band gap of the synthesized $BiFeO_3$ nanopowders, the absorption optical property of the resultant BFO nanopowders was measured using a Perkin Elmer model Lambda 950 UV-Vis-NIR spectrophotometer with an integrating sphere. 1 mg of BFO nanopowders were pressed with 1 g of potassium bromide (KBr) salt into a thin translucent disc, as the KBr salt has no significant light absorbtion in visible light region and also transparent to near ultraviolet to the long-wave infrared wavelengths (0.25-25 μm) region. The absorption spectra data was further processed using Tauc's relationship to calculate the optical energy band gap of the $BiFeO_3$ nanopowders.

The UV-Vis-NIR is the instrument which can read out absorption spectroscopy in the ultraviolet-visible-near infrared spectral region. The absorbance (A) of the sample can be calculated based on the Beer-Lambert's law;

$$A = -\log \frac{I}{I_o} = \varepsilon * c * l \qquad \text{Equation 3.2}$$

Where ε is the extinction coefficient, c is the concentration of the absorbing species, and l refers to the path length through the sample, I refers the intensity of light that passed through a sample, (I_o) is the intensity of light before it passes through the sample (I_o),

3.4.5 Zeta Potential Measurement

The Zeta potential is refer to the measure of the magnitude of the electrostatic or charge repulsion or attraction between particles and provides detailed information on the causes of dispersion, aggregation or flocculation of particles. The zeta potential is determined by the measurement of electrophoretic mobility of particle suspension by an electrophoresis experiment on the sample and measurement of the velocity of the particles using Laser Doppler Velocimetry (LDV).

Due to interaction of the ions/charges at the particle surface, thus resulting in an electrical double layer that exists around each particle, see figure 3.4. The interface between the particle surface and liquid layer surrounding the particle consists of two parts; an inner region (the Stern layer), where the ions are strongly bound and an outer region (diffuse region), where they are less firmly attached. When a particle moves due to external field or gravitation force, ions within the boundary move with it, but any ions beyond the boundary do not travel with the particle. The potential that exists at this boundary is known as the Zeta potential.

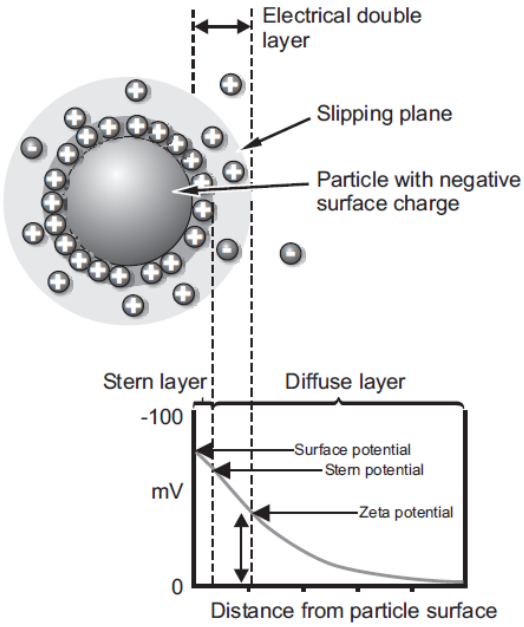

Figure 3.4 Zeta potential and the electrical double layer

The BFO powder was dispersed in DI water with 0.01wt% concentration. The zeta potential of the BFO powder dispersed in the DI water was measured using a Malvern Zeta Sizer Nano ZS Series at pH values of 6.7 (normal water pH), 4.8, 3.2 and 2.2. The pH of the solution was adjusted by titration with diluted nitric acid.

3.4.6 X-Ray Photoelectron Spectroscopy (XPS) Analysis

Photoelectron spectroscopy utilizes photo-ionization by X-Ray irradiation on the sample surface to emit photoelectrons. The kinetic energy distribution of the emitted photoelectrons is analysed to study the composition and electronic state of the surface region of a sample. Each and every element will give rise to a specific set of peaks in the photoelectron spectrum with respect to kinetic energies determined by the photon energy and the respective binding energies associated

with each core atomic orbital, thus, provides a quantitative analysis of the material surface composition.

X-ray sources that are commonly used are the Mg K_α radiation: $h\nu$ = 1253.6 eV and Al K_α radiation: $h\nu$ = 1486.6 eV. The emitted photoelectrons will therefore have kinetic energies in the range of around 0 - 1250 eV or 0 - 1480 eV. The X-ray photo-electron spectrometry (XPS) was performed using a Thermo Fisher Scientific Theta Probe. The X-ray source was monochromatic Al Kα (1486.5 eV) at a voltage of 15 kV and 100 W. XPS spectra were gathered using a hemispherical energy analyzer operated at pass energy of 200eV for survey scans and 40.0 eV for high resolution elemental scans.

3.4.7 X-Ray Fluorescence Spectroscopy Analysis

The Wavelength dispersive X-ray spectroscopy (WDXRF or WDS) is a method used to isolate the X-rays of interest for quantitative analysis and to count the number of X-rays of a specific wavelength diffracted by a crystal. The wavelength of the incident x-ray and the crystal's lattice spacing are related by Bragg's law.

For XRF measurements, the BFO nanopowders sample has to be pressed into a pellet (13 mm diameter) with a uniaxial compacter. Sample preparation needs to be done carefully and with the use of proper devices to prevent contamination. Therefore the devices such as mills, mortars and pulverisers should be made of agate, silicon carbide or tungsten carbide. The WDXRF measurement was

performed using a Shimadzu XRF-1800. Measurement was done with a 12 mm mask, with a 50 kV tension and a 100 μA current for 400 seconds.

3.4.8 Vibrating Sample Magnetometer

The magnetization of the optimized nanopowders was measured using a Princeton Measurements Corporation Vibrating Sample Magnetometer (VSM) with an applied field of $\mu_0 H = \pm 0.2T$ at room temperature ambient.

3.5 Photo-Decolourisation of Organic Dyes

3.5.1 Preparation of Dye Solution

Organic dyes are used as the pollutants model for the photodegradation reactivity assessment. The degradation of the dyes as a result of the photochemical reaction of the catalyst is measured on the colour intensity drop after a period of time. The dyes that are used for the photodegradation experiment are Rhodamine B (RhB) and Acid Black (AB) dyes.

Rhodamine B is one of the most important dyes of the xanthene group, which is highly water soluble and it is found as a reddish violet powder. Rhodamine B is a chemical compound and an amphoteric dye, although usually listed as basic as it has an overall positive charge. The solubility of Rhodamine B in water is approximately 50 g/L. However, the solubility in an acetic acid solution (30 vol.%)

is at 400 g/L. The maximum absorbance (λmax) of Rhodamine B is around 550 nm - 555 nm and the molecular weight of Rhodamine B is 479.02 g/mol.

Acid Black or Amido black 10B is an amino acid azo dye used commonly in the biochemical research. Amido Black can be dissolved either in methanol or water. It has molecular formula of $C_{22}H_{14}N_6Na_2O_9S_2$ with molar mass 616.49 g mol^{-1} and solubility in water is 30 g/l at 20 ℃. The dye solution was prepared with a 10 ppm concentration, where 4.8 mg of RhB and 6.16 mg of AB dye (equivalent to 0.01 mmol) powder were dissolved completely in 1 litre of de-ionised water with constant stirring and sonication.

3.5.2 Photo-Decolourisation of Organic Dyes Experimental Set-Up

The photodecolourisation reactivity of the BFO nanopowders are compared by the colour change of the organic dyes after the aqueous dye solution reacts with the catalyst powder loaded into the dye solution with concentration of 0.3g/100 mL as a result of exposure to the solar simulator light (SAN-EI solar simulator – XES Series) with AM 1.5 under constant stirring using a magnetic stirrer. The change in the colour of the dye is measured by diffuse reflectance spectroscopy and absorbance measurements. 3 mL of the solution was taken for sampling every interval followed by centrifugation at 12000 RPM for 10 minutes to separate the nanopowders and the dye solution before the measurement of the absorption spectra. The experimental set-up for the photodegradation test is shown in the figure 3.5 below.

A solar simulator is a device that provides light illumination mimicking the natural sunlight irradiation on earth surface with the irradiation energy approximating 1000 watt/m^2. Solar simulator is used to provide a controllable indoor test facility under laboratory conditions for the testing of solar cells, sun screen, plastics, and other materials and devices.

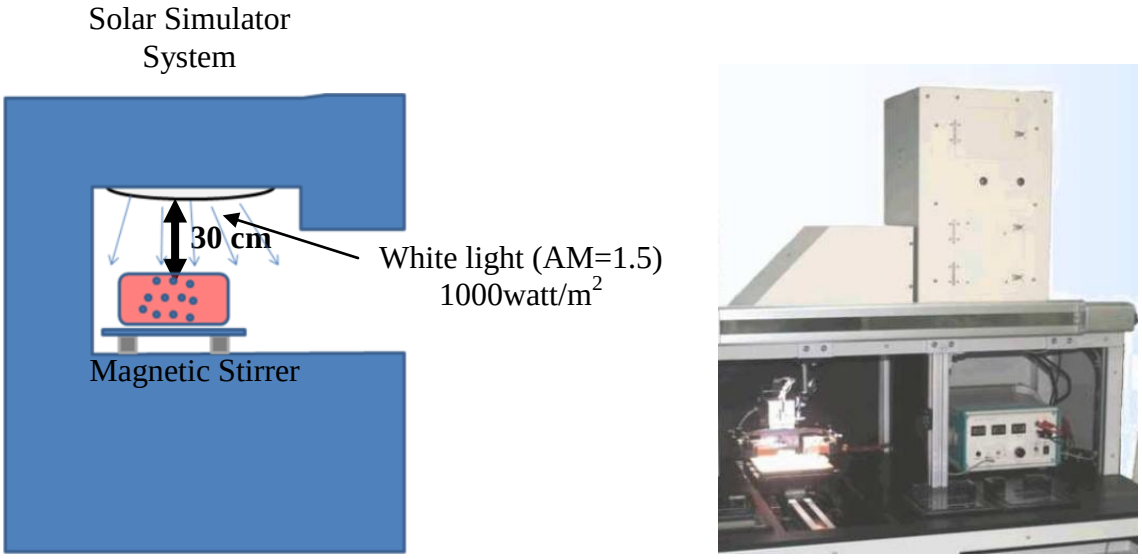

Figure 3.5 (a) Photodecolurisation of the organic dyes experimental set-up, and (b) SAN-EI Solar simulator equipment used in the experiment.

4 RESULTS AND DISCUSSIONS

4.1 $BiFeO_3$ Powder Synthesis via Autocombustion Route

4.1.1 X-Ray Diffraction Characterization

A design of experiment (DOE) has been prepared on a few annealing parameters of annealing temperature and duration as shown in table 4.1. The initial synthesis experiment started with Metal / Glycine molar ratio of 1:1 and annealing temperature of as low as 450℃ with a varying temperature and duration to determine the optimum annealing parameter to form the $BiFeO_3$(BFO) phase. Fifteen annealing parameters have been determined in the synthesis of the BFO experiment to obtain the best annealing temperature from all the parameters denoted from (a) to (o).

Table 4.1 DOE table of annealing parameters

Temperature / Duration	450°C	550°C	650°C
3 hours	(a)	(f)	(k)
6 hours	(b)	(g)	(l)
9 hours	(c)	(h)	(m)
12 hours	(d)	(i)	(n)
24 hours	(e)	(j)	(o)

From the XRD pattern in figure 4.1, the powder before annealing shows that some of the BFO phase has formed. However, both the Bi_2O_3 and the Fe_2O_3 phases exist in the BFO powder as shown in the highlighted patterns. The non-annealed BFO powder was placed inside the furnace for annealing at various temperatures and soaking durations to obtain the best annealing parameters to produce a high purity crystalline BFO phase.

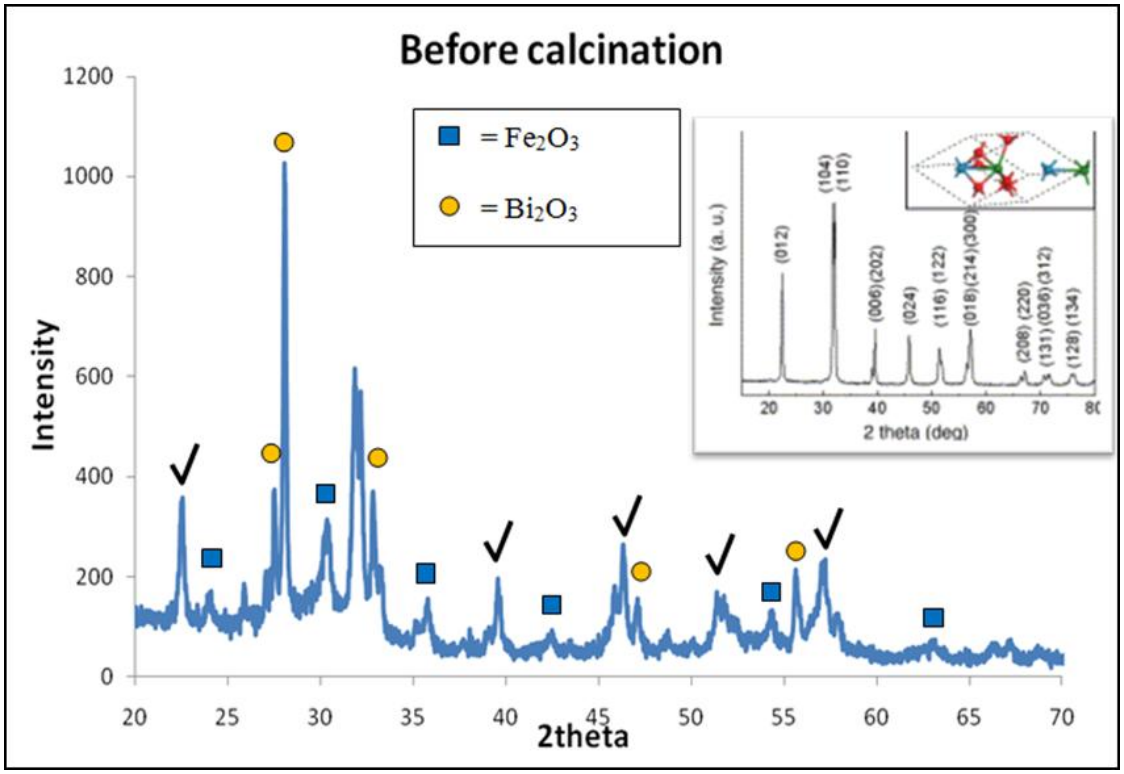

.

Figure 4.1 XRD pattern of the BFO powder after autocombustion before annealing and its analysis in comparison with the Bi_2O_3 and the Fe_2O_3 JCPDS data.

Figure 4.2 presents the XRD patterns of the BFO nanopowders annealed at 450 ℃ for 3, 6, 9, 12 and 24 hours showing that the BFO powder obtained are a highly crystallized BFO phase and exhibit a perovskite structure according to the JCPDS card no. 71-2494. However, the XRD patterns for all the samples annealed at 450 ℃ showed the presence of the Bi_2O_3 and the $Bi_2Fe_4O_9$ phases as also reported

by Jong Kuk Kim *et al.*[81] as highlighted in the figure 4.2. The obvious peak-splitting shows that the nanoparticles are rhombohedral, consistent with the structure of BFO ceramics[10]. As the annealing duration increase from 3 hours to 24 hours at 450 ℃, the Bi_2O_3 and $Bi_2Fe_4O_9$ phase decreased as shown in the decrease in the peaks intensity.

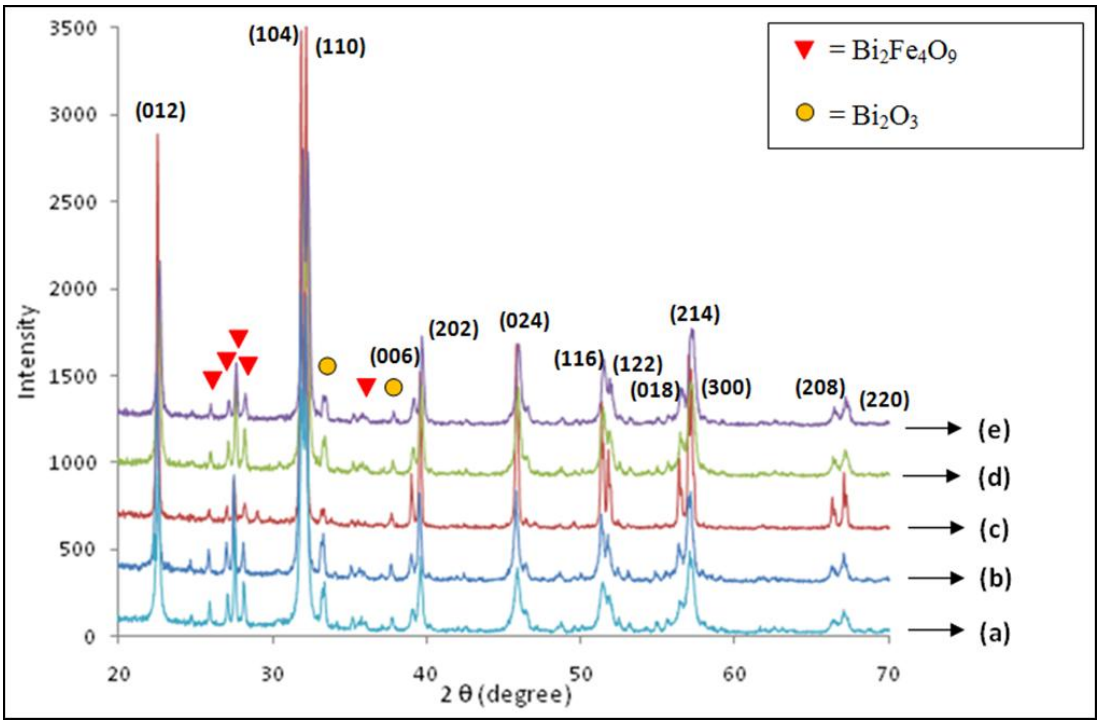

Figure 4.2 XRD patterns of the BFO powder synthesized at annealing temperature of 450 ℃ with various soaking durations of 3 hours (a), 6 hours (b), 9 hours (c), 12 hours (d) and 24 hours (e).

The XRD patterns of the BFO nanopowders annealed at 550 ℃ for 3, 6, 9, 12 and 24 hours also showed that the BFO powder obtained are a highly crystallized BFO phase, but the Bi_2O_3 and $Bi_2Fe_4O_9$ phases still exist. As the annealing duration increased from 3 hours to 24 hours at 550 ℃, the Bi_2O_3 phase and the $Bi_2Fe_4O_9$ phase decreased as shown in figure 4.3.

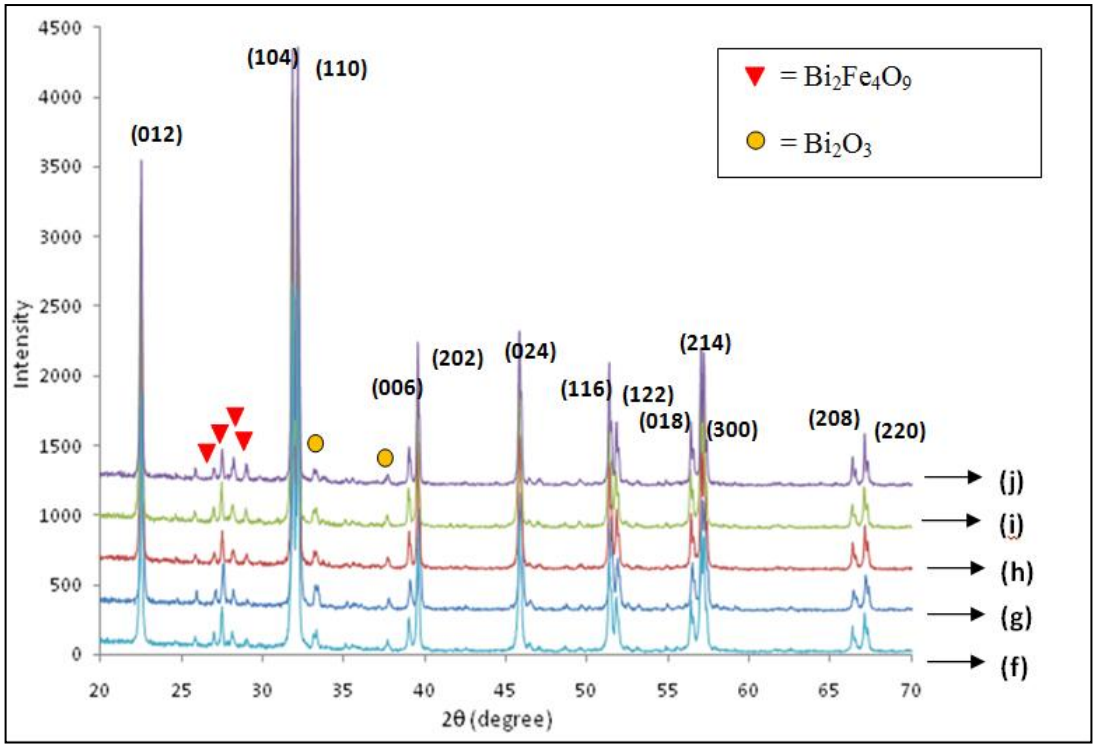

Figure 4.3 XRD patterns of the BFO powder synthesized at annealing temperature of 550 ℃ with various soaking durations of 3 hours (f), 6 hours (g), 9 hours (h), 12 hours (i) and 24 hours (j).

Figure 4.4 presents the XRD patterns of the BFO nanopowders annealed at 650 ℃ for 3, 6, 9, 12 and 24 hours also showing that the BFO powder obtained is a highly crystallized BFO phase. However, at 650 ℃ annealing temperature, the presence of the Bi_2O_3 and the $Bi_2Fe_4O_9$ phases are minimum compared to annealing at 450 ℃ and 550 ℃. As the annealing duration increased from 3 hours to 24 hours at 550 ℃, the Bi_2O_3 and the $Bi_2Fe_4O_9$ phase increased slightly only as evidenced in the figure 4.4. Thus, the best set of BFO synthesis parameter is annealing at 650 ℃ with 3 hours of soaking duration to produce a high crystalline high purity BFO powder.

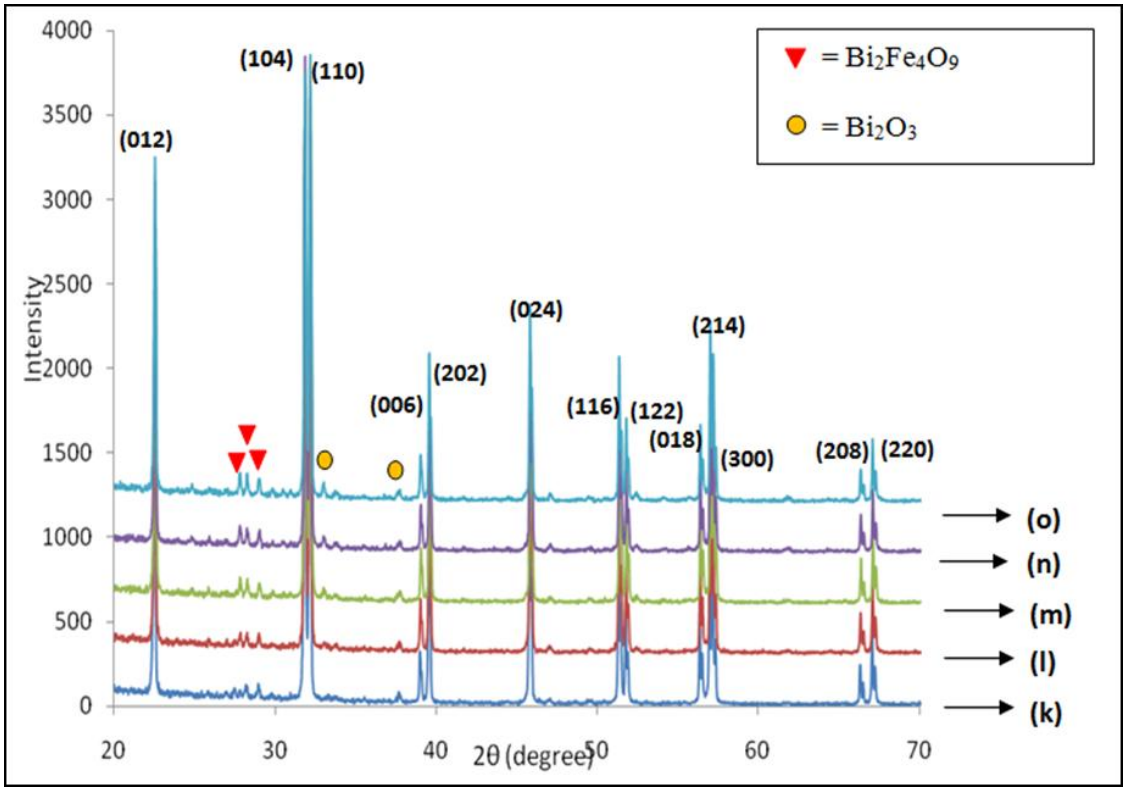

Figure 4.4 XRD patterns of the BFO powder synthesized at annealing temperature of 650 ℃ with various soaking durations of 3 hours (k), 6 hours (l), 9 hours (m), 12 hours (n) and 24 hours (o).

The XRD patterns of the BFO powder synthesized at 450 ℃, 550 ℃ and 650 ℃ for 3 hours soaking duration were combined to ascertain the comparison among the three calcination temperatures. It was observed that there is a trend that shows the Bi_2O_3 and the $Bi_2Fe_4O_9$ phases diminish as the calcination temperatures increases as shown in figure 4.5.

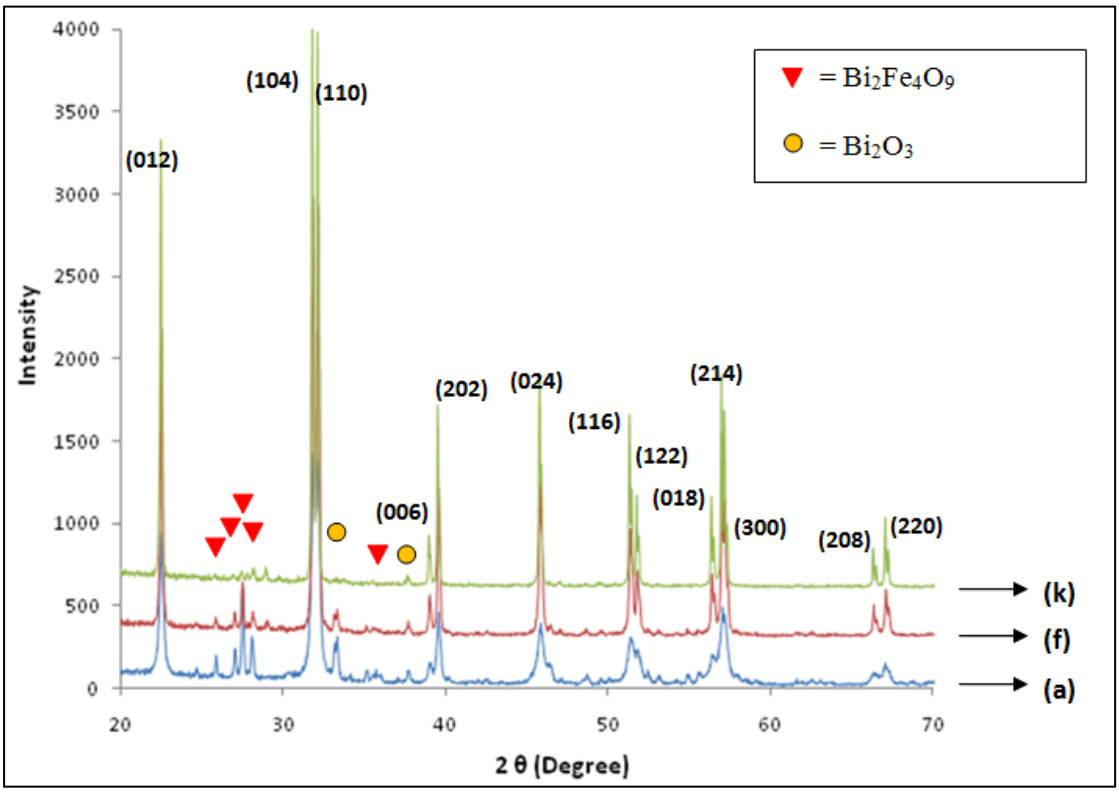

Figure 4.5 XRD patterns of the BFO powder synthesized at 450 ℃ (a), 550 ℃ (f) and 650 ℃ (k) for 3 hours soaking durations.

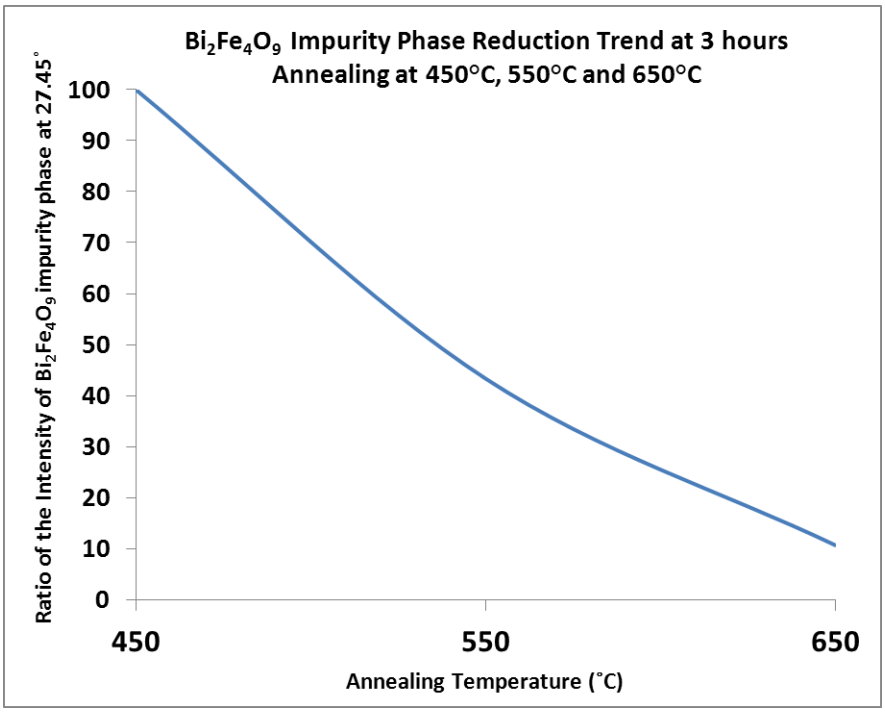

Figure 4.6 The impurity phase ($Bi_2Fe_4O_9$) reduction trend of 3 hours annealing at 450 ℃, 550 ℃ and 650 ℃

In order to see the reduction of the $Bi_2Fe_4O_9$ impurity phase at different annealing temperature, a graph of the relative peak intensity ratios of the $Bi_2Fe_4O_9$ impurity peak at 2 theta angle of 27.45 ° at three different annealing temperatures (450 ℃, 550 ℃, and 650 ℃) is plotted as shown in figure 4.6. It is revealed that the annealing at 450 ℃ has the highest peak intensity of the $Bi_2Fe_4O_9$ impurity phase and gradually reduced at 550 ℃ and is lowest at 650 ℃, where the peak intensity of $Bi_2Fe_4O_9$ impurity phase is about 10% of the 450 ℃ annealing temperature.

A series of experiments were conducted to synthesize the BFO powder with different Metal/Glycine (Fuel) molar ratios to investigate the influence of the amount of the fuel used in the auto-combustion synthesis technique. As shown in figure 4.7, the BFO powders were synthesised with the molar ratios of metal ions to glycine (m/g) of 0.5, 1 and 2. The m/g ratio of 1 was used for all the prior synthesis experiments. When the glycine fuel amount is less (m/g = 0.5), the resultant BFO powder has higher level of $Bi_2Fe_4O_9$ and Bi_2O_3 phases compared to the BFO powder synthesized with m/g ratio of 1 and 2. This could indicate a lack of fuel to carry out combustion process to form the BFO phase.

The annealing parameter in this experiment (varying the amount of the glycine fuel) is 650 ℃ and a soaking duration of 3 hours. These annealing parameters are the optimum annealing conditions as determined in the previous BFO nanopowders work.

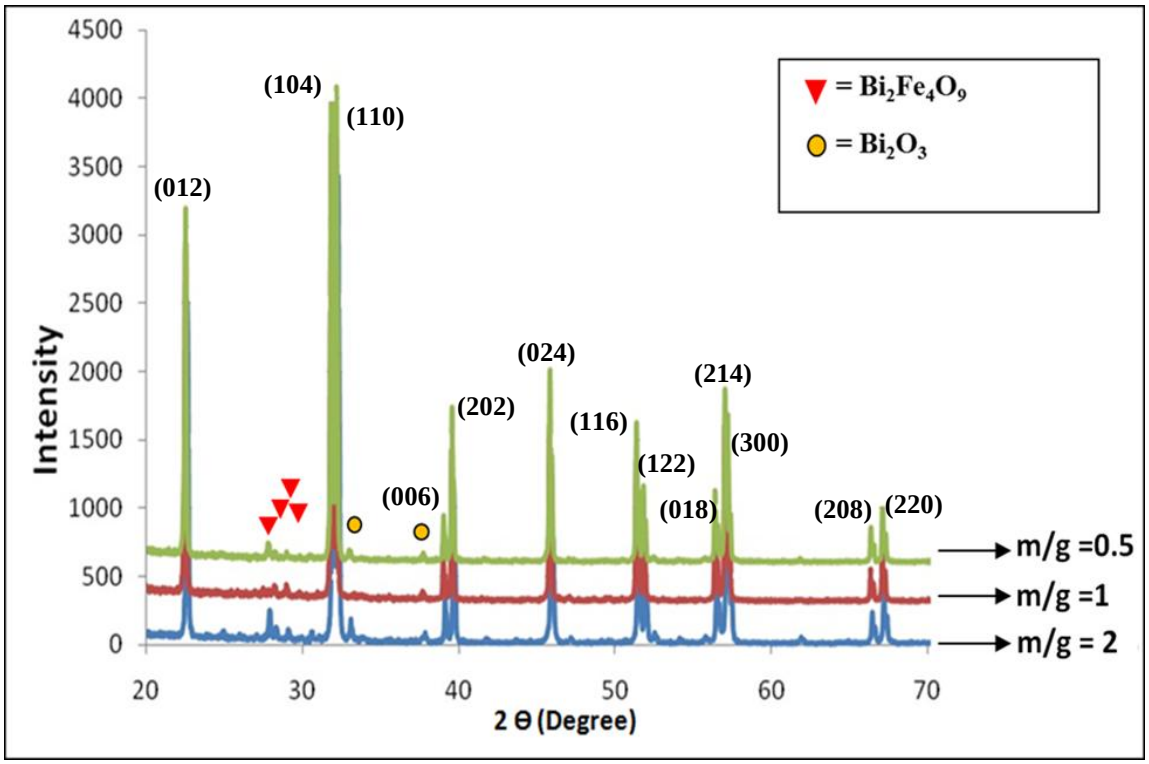

Figure 4.7 XRD patterns of the BFO powder synthesized at 650 ℃ for 3 hours annealing durations with a different metal/glycine fuel molar ratio (m/g = 0.5, 1and 2).

The XRD pattern shown in Figure 4.8 obtained for the $BiFeO_3$ (BFO) sample after annealing at optimum parameters (650 ℃ – 3 hours) shows that the material contains a fully crystalline phase and a very minor trace of secondary phases of ($Bi_2Fe_4O_9$ & Bi_2O_3) with the majority phase fitting the BFO pattern according to the JCPDS card no. 71-2494. The XRD pattern of the BFO sample produced using this technique matched very closely with the accepted BFO XRD pattern published in a previous work by Gao *et al.*[97] and also showed the peak splitting associated with the BFO ceramics rhombohedral crystal lattice structure.

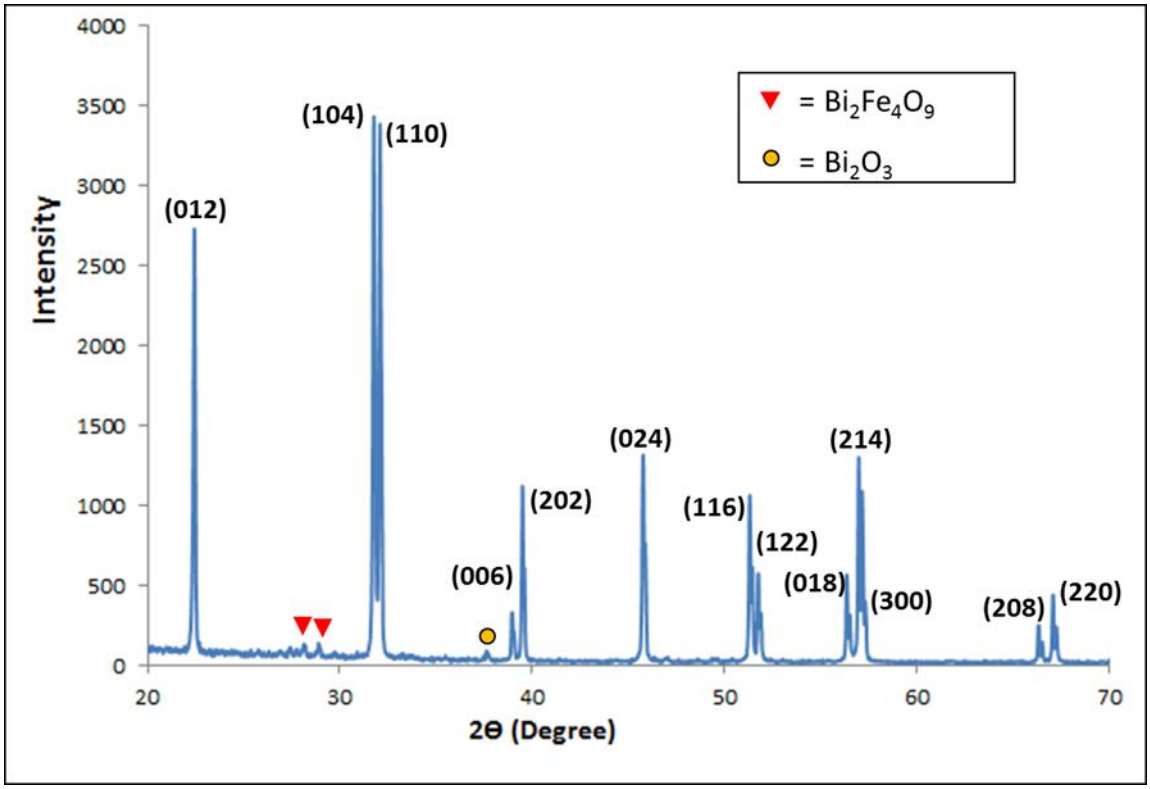

Figure 4.8 XRD pattern of the BFO powder synthesized at 650℃ for 3 hours soaking durations (optimum synthesis parameters).

4.1.2 Morphology Characterization of the BFO Nanopowders

For morphology characterization by scanning and transmission electron microscopy, the BFO powders were dispersed in water and subjected to ultra-sonication to break down the agglomeration. It was observed that the resultant BFO nanopowders morphology was spherical in shape as shown in the figure 4.9 below. The size of the particles is in the range of 100 nm and quite uniform in size and shape.

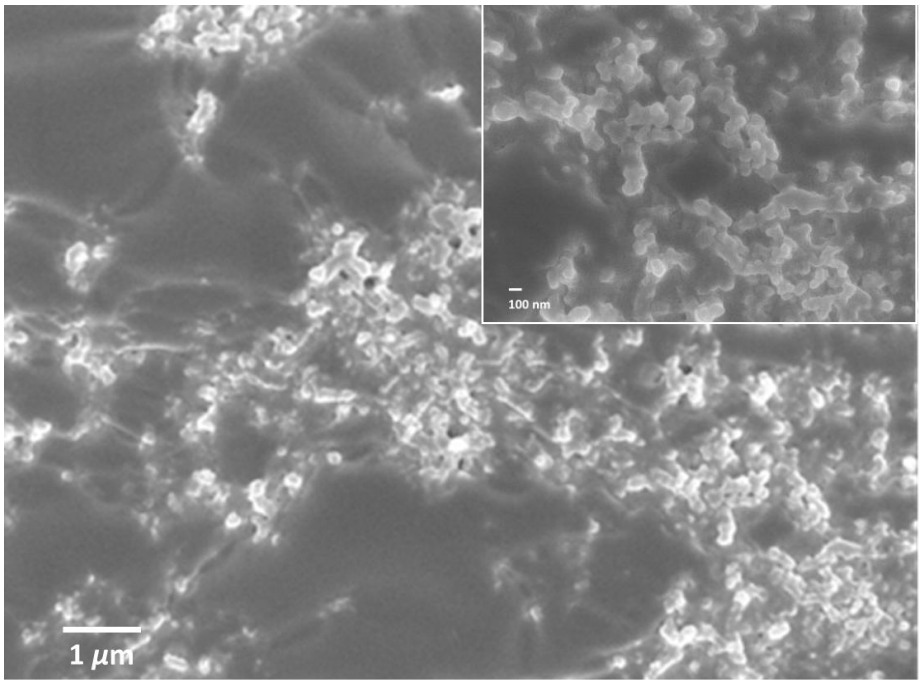

Figure 4.9 FESEM micrograph of synthesized BFO nanopowders at 650˚C annealing for 3 hours with m/g ratio = 1 (inset: higher magnification of the SEM micrograph).

For the TEM analysis as shown in figure 4.10, it was observed that the BFO nanoparticles size is around 20 nm to 100 nm with spherical morphology but showing a certain degree of faceted morphology.

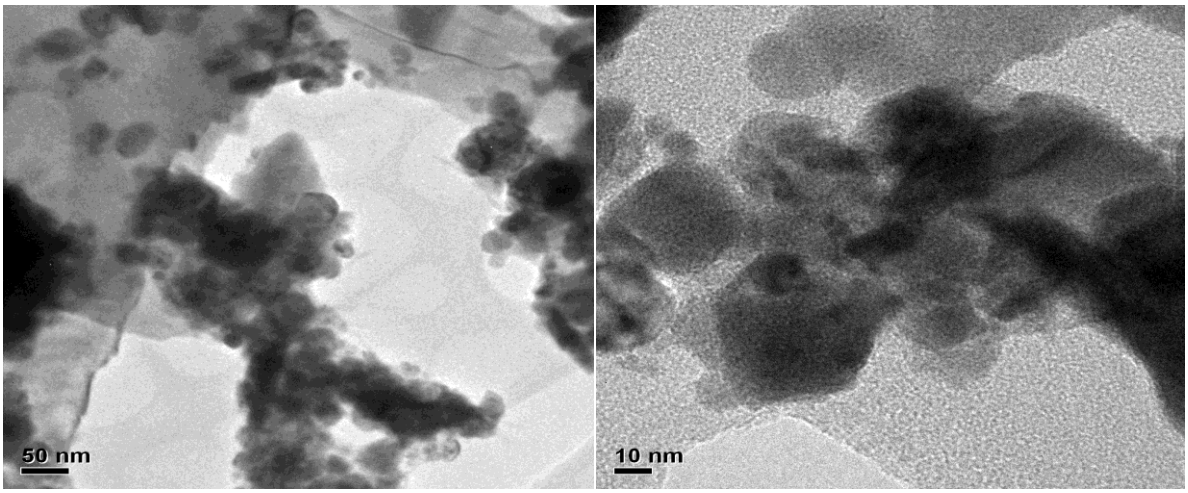

Figure 4.10 TEM micrograph of synthesized BFO nanopowders at 650˚C annealing for 3 hours with m/g ratio = 1.

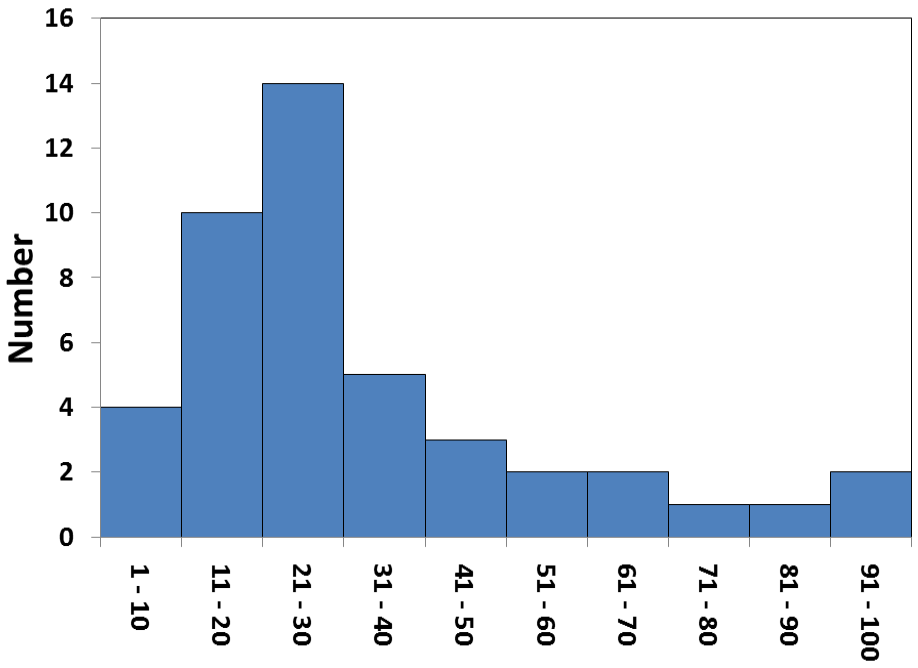

Figure 4.11 Histogram of synthesized $BiFeO_3$ particles at 650˚C annealing for 3 hours with m/g ratio = 1, showing particle size distribution.

From the high resolution Transmission Electron Micrograph (TEM), a histogram of the particle size distribution (figure 4.11) was manually derived from the measurement of all the particles in the micrograph and indicates a good percentage of particles in the range of 10 -40 nm size.

4.1.3 Optical Property Characterization of the BFO Nanopowders

The BFO nanopowders synthesized using a Metal/Glycine molar ratio of 1:1 and calcined at 650 ℃ for 3 hours were used in the optical characterization work. The absorption characteristics of the BFO nanopowders were investigated using UV–Vis-NIR spectrophotometer and the absorption spectra of the synthesized BFO nanopowders is shown in figure 4.12. The absorption cut-off wavelength of the synthesized BFO sample is about 565 nm, indicates that the BFO nanopowders

have a good absorption at UV and near UV range and steeply and the absorption steeply falling off up to 565 nm, and there is also a shallow absorption at around 600 nm wavelength.

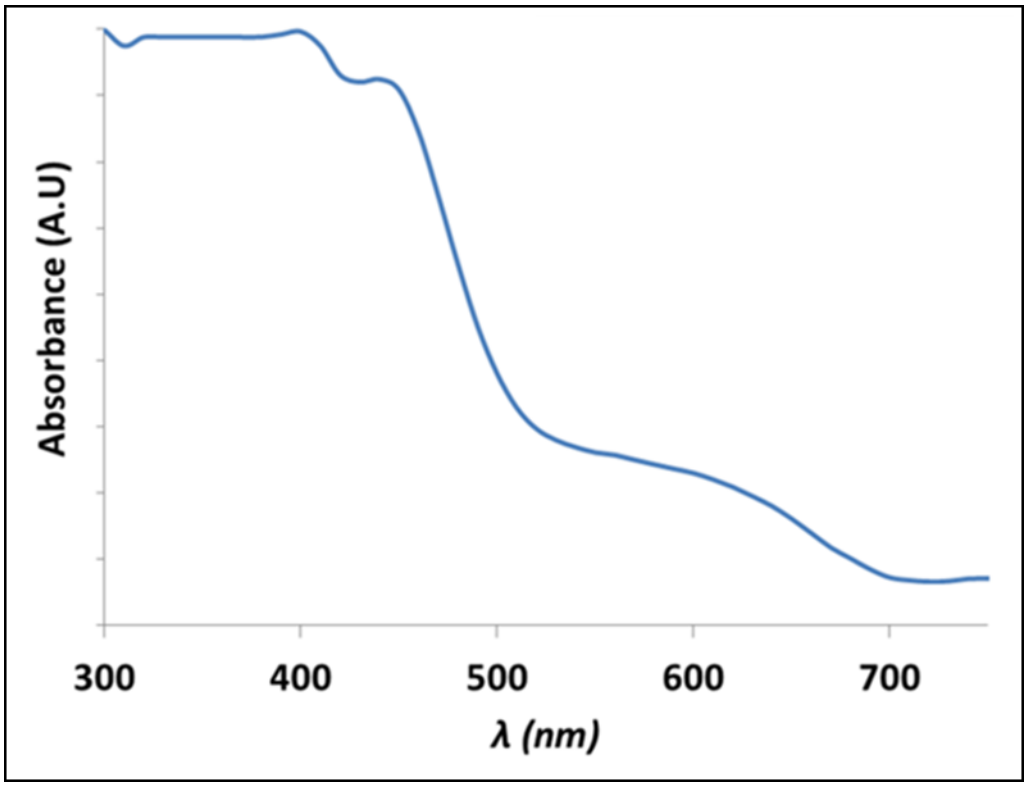

Figure 4.12 the UV-Vis absorption spectroscopy of the BFO nanopowders synthesized at 650˚C for 3 hours with m/g ratio = 1.

The optical energy band gap of the synthesized BFO nanopowders was calculated using the absorption spectra obtained from the UV-Vis-NIR spectrophotometer. Figure 4.13 showed the optical band gap of the BFO nanopowders calculated using Tauc's relationship (equation 4.1):

$$\alpha h\nu = \mathrm{A}(h\nu - E_g)^n \qquad \text{Equation 4.1}$$

where n is ½ as the BFO is a direct bandgap semiconductor. To obtain an optical band gap (E_g) value, a curve of $(\alpha hv)^2$ is plotted against (hv) and extrapolation of the linear region of the graph intersecting x-axis at 0 value gives the value of the optical band gap, E_g. The calculated value from the Tauc's plot of the absorption spectrum is around 2.2 eV, which is similar to the band gap value with that of another report by Gao et al[10] which is 2.18 eV and smaller than the BFO thin film of 2.5 eV as reported by K.Takahashi et al.[146] These results suggest that the synthesized BFO nanoparticles are promising visible-light photocatalysts.

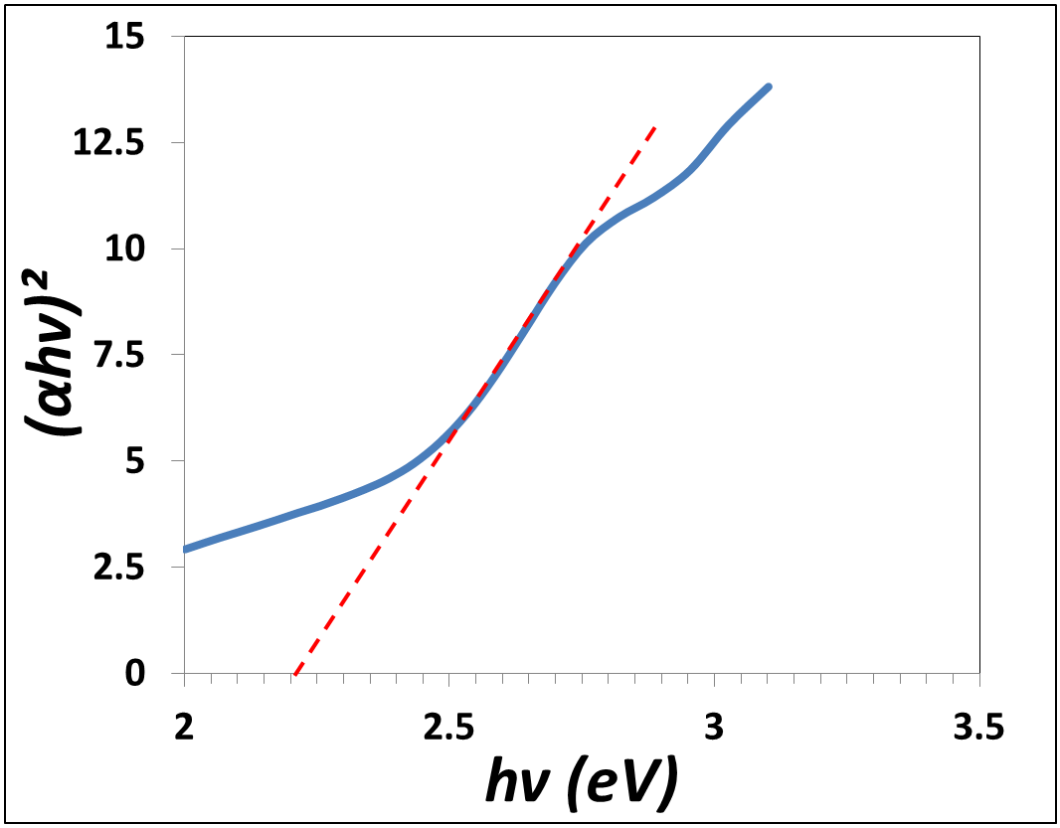

Figure 4.13 Tauc's plot of the absorption spectra of BFO nanopowders annealed at 650 ℃ for 3 hours

4.1.4 Magnetic Property Characterization of the BFO Nanopowders

The magnetic property of the synthesized BFO nanopowders with the optimum synthesis parameters was measured to a maximum applied field of 0.2 Tesla and is shown in Figure 4.14. Earlier work by Smolenskii *et al*[64] shows that bulk BFO is antiferromagnetic. However, the synthesized BFO nanoparticles show a slight magnetic hysteresis loop and the magnetization do not saturate. This is in agreement with the work done on synthesizing nanoparticles derived from sol-gel technique by Park et al.[162] The magnetization value of the BFO nanoparticles at the maximum measurement field corresponds well to the value for BFO thin film with reference to the work by Mathur et al.[44], but is an order of magnitude smaller compared to the magnetization value of the BFO nanoparticles synthesized by sol-gel technique.[162] The difference in the magnetization value could be due to the differences in the synthesis technique and its associated particle-size distribution.

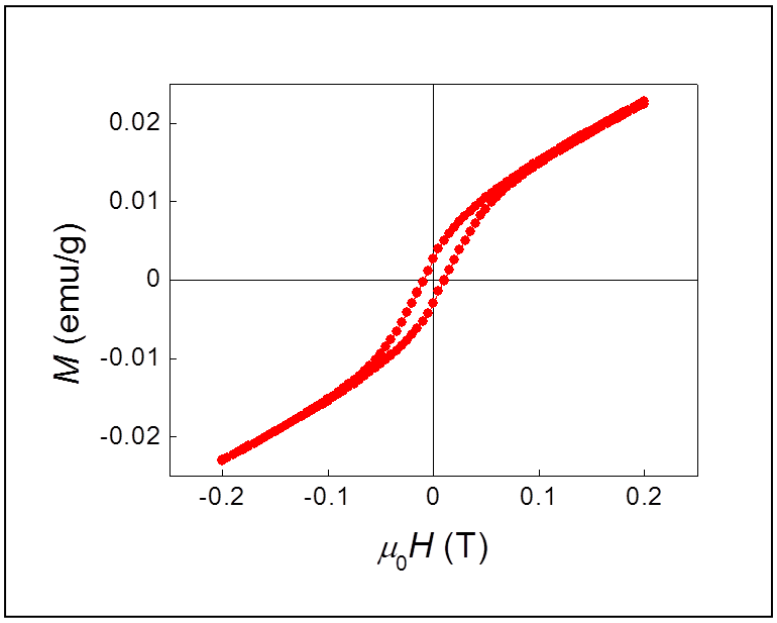

Figure 4.14 Room temperature magnetization versus the field for the $BiFeO_3$ nanoparticles annealed at 650 ℃ for 3 hours.

4.2 Photodecolourisation of Organic Dyes and Photocorrosion Study of the $BiFeO_3$

With a portable spectrometer, the transmission of the solar simulator illumination was measured for different BFO nanopowders loadings, i.e. 0.1 g and 0.3 g in 100 ml of 10 ppm concentration of Rhodamine Blue (RhB) dye solution (figure 4.15). The objective of this experiment was to obtain the optimum solution depth (thickness) for optimum light penetration from a solar simulator through the BFO powder loaded RhB dye solution. The BFO nanopowders suspensions were transferred into a borosilicate glass beaker starting with 0.5 cm thickness and increased incrementally by 0.5 cm after each transmission measurement. The spectrometer detector is placed right below the beaker under the solar simulator light path as shown in the experimental set up image in figure 4.16.

Figure 4.15 Two different BFO nanopowders concentration loaded into a 10 ppm RhB dye solution: 0.1 g BFO/100 ml RhB dye solution (Left), 0.3 g BFO/100 ml RhB dye solution (Right)

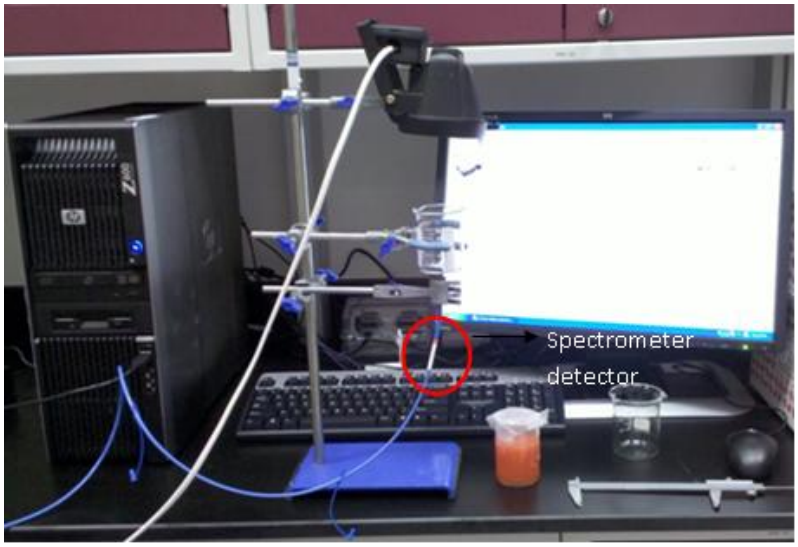

Figure 4.16 Setup of the transmission test to measure the depth of the light penetration on a different suspension concentration with a different thickness of the BFO-RhB dye solution.

For 0.1 g BFO powder loading in 100 ml 10ppm RhB dye solution, as shown in the transmission measurement graph in figure 4.17, the visible light was able to pass through the suspension up to 5 cm thickness, however, the powder loading may not be enough for good photodecolourisation activity.

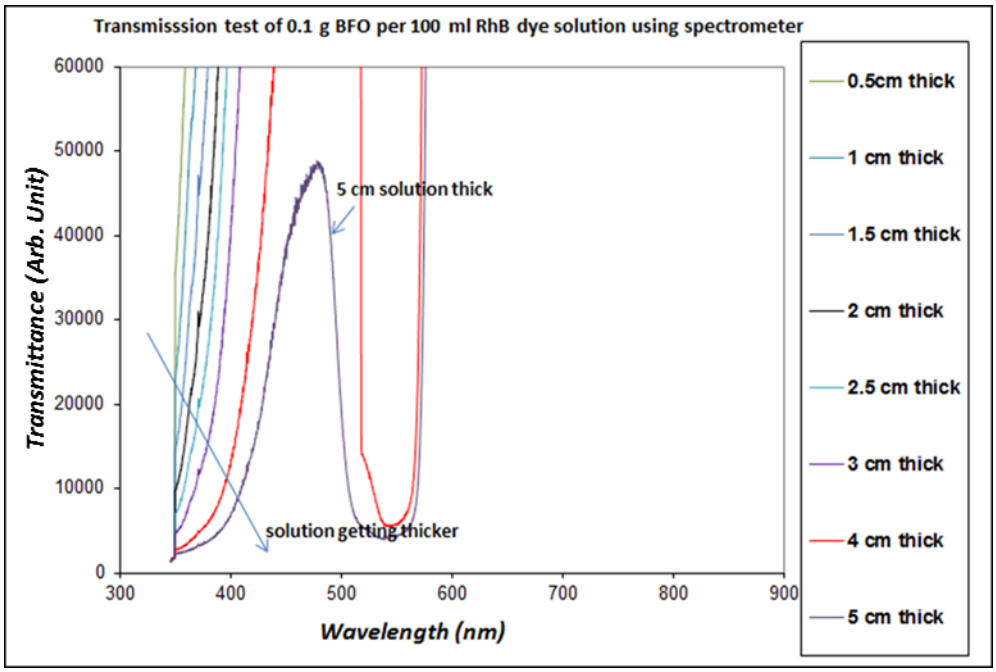

Figure 4.17 Transmission test of 0.1 g BFO nanopwder in 100 ml of 10 ppm concentration of RhB dye solution.

Figure 4.18 shows the transmission test result of 0.3 g BFO powder loaded into 100 ml of the RhB dye solution (10 ppm concentration). It is observed that above 1.5 cm solution thickness, the suspension has blocked most of the light from the halogen lamp source. At 1cm suspension thickness, it has still allowed the light to pass through the solution. Hence, for the photodecolourisation experiment, a 1 cm thick solution of 0.3g BFO/100 ml RhB solution is chosen.

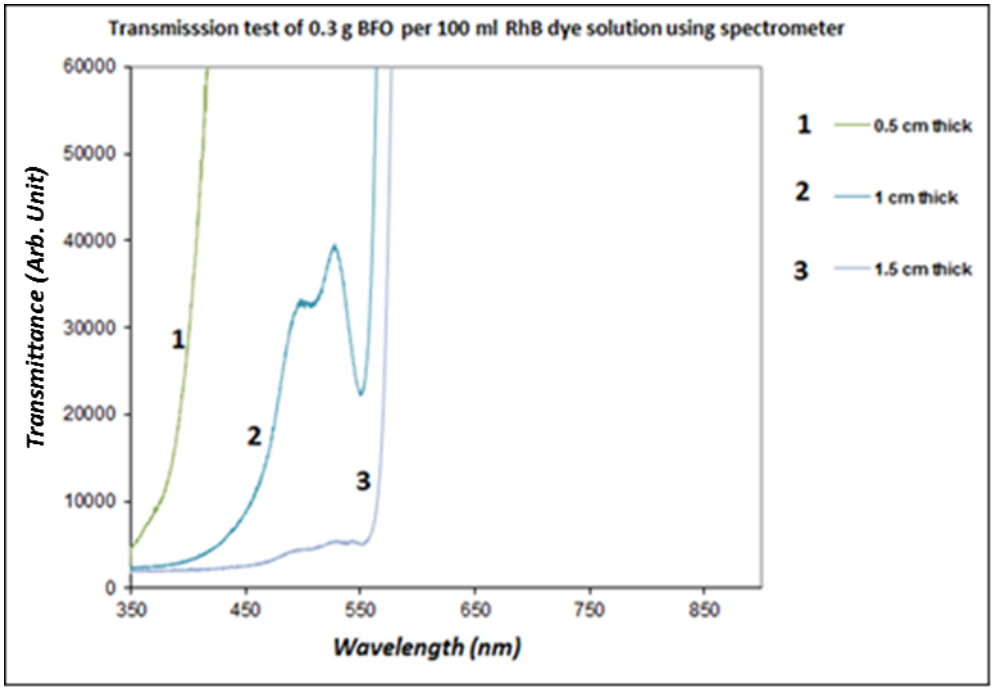

Figure 4.18 Transmission test of 0.3 g BFO nanopowders in 100 ml of 10 ppm concentration of the RhB dye solution.

4.2.1 Photodecolourisation of RhB Dye with BFO Nanopowders

A photodecolourisation experiment was performed with a solar simulator with air mass = 1.5 and lamp output of 1000 watt/m^2 as shown in figure 3.12. During the photodecolourisation experiment, the BFO-RhB dye suspension was stabilized in the dark under stirring for 30 minutes. The BFO-RhB dye suspension

was constantly stirred during illumination in the glass petri dish. From the absorption spectrum of the RhB dyes with a different exposure time (figure 4.19), it was observed that at 1 hour exposure there was a drop in absorbance intensity. However, at 2 hours to 6 hours exposure time, there was no noticeable drop in the absorbance intensity. Sampling was at hourly intervals, and subjected to 10 minutes centrifugation at 12000 RPM to separate the BFO nanoparticles and the RhB dye in the suspension.

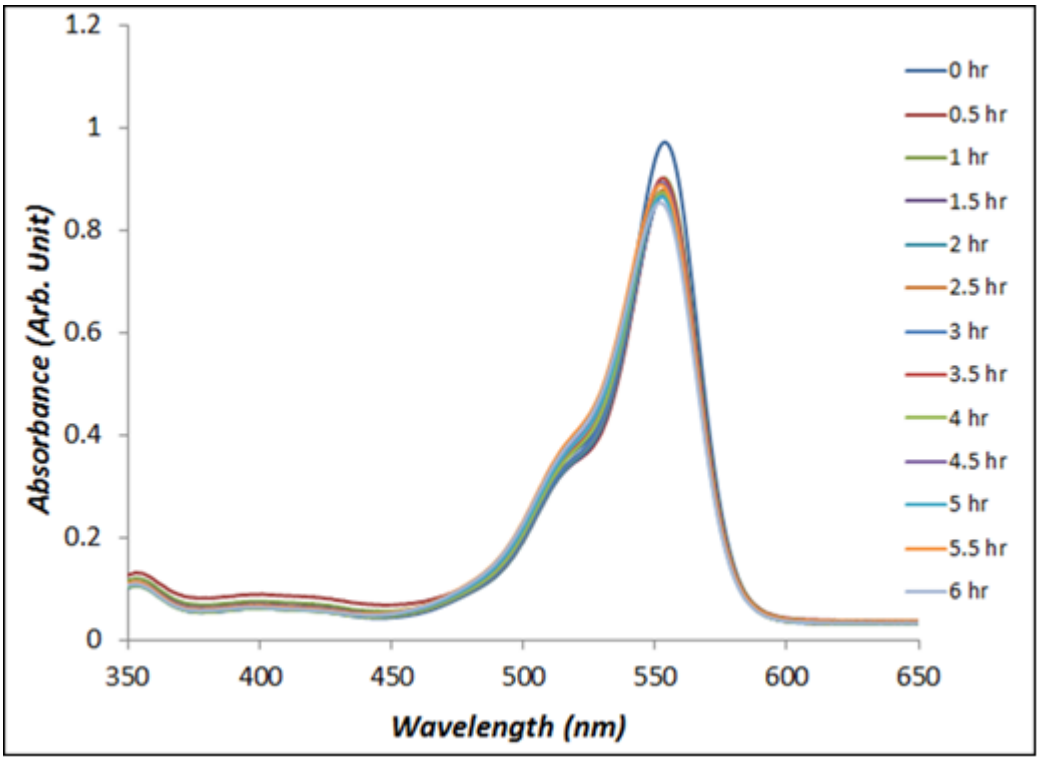

Figure 4.19 Absorption spectrum of Rhodamine Blue dye solution before and after 6 hours of illumination with a solar simulator AM=1.5

The photodecolourisation profile was plotted from the absorption spectral of the RhB dye exposed under different timing with the presence of the BFO nanopowders, with reference to the absorption peak wavelength (554 nm) of the Rhb dye. The drop in the absorption peaks at each sampling interval were normalise

to the absorption of the initial RhB dye absorption peak ((C/C_0) x100%). The changes/drops in the absorption peak normalise against the initial RhB dye solution absorption peak is plotted against sampling interval timing to obtain the photodecolourisation profile (figure 4.20).

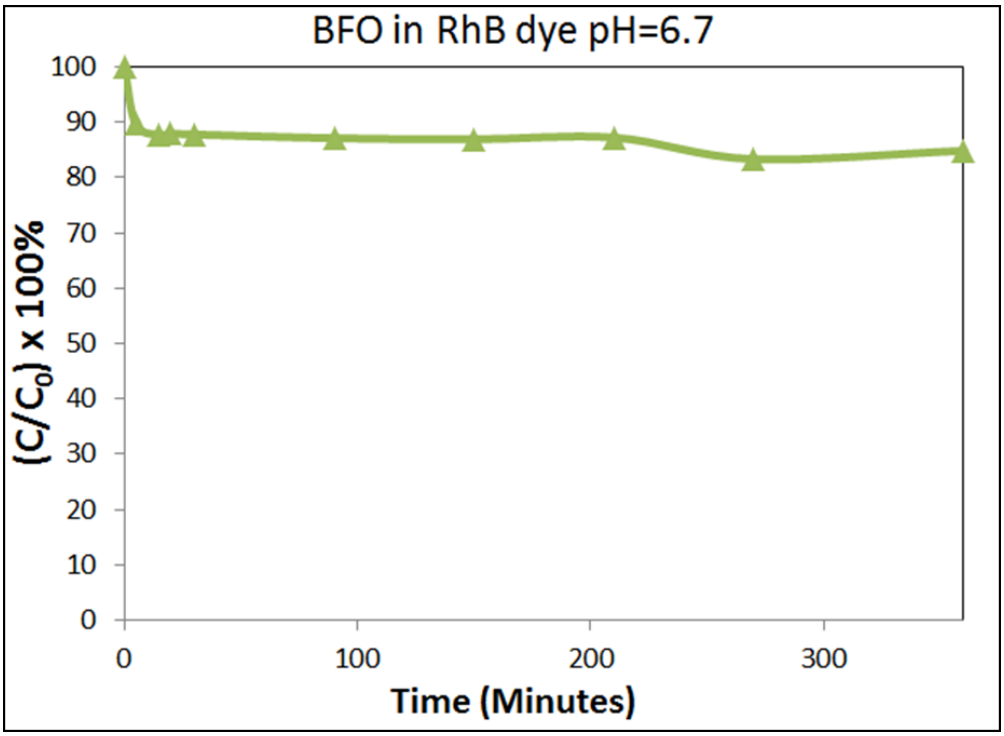

Figure 4.20 Photodecolourisation profile Rhodamine B dye by synthesized BFO nanopowders under solar simulator illumination (AM=1.5)

The photodecolourisation of the RhB dye solution with the BFO nanopowders under normal pH environment (pH=6.7) shows a drop of about 15% and the photodecolourisation rate flattened after 15 minutes, indicating there is no further decolourisation activity of the RhB dye by the BFO nanopowders under exposure to the solar simulator (figure 4.20). From this photodecolourisation experiment, it was hypothesized that the RhB dye molecules did not interact or adsorb properly on the surface of the BFO particles; hence minimum redox reaction

occurred to the RhB dye molecules causing it to be non-effective in photodecolourisation.

Other photodecolourisation experiments involving a blank RhB dye solution (without BFO nanopowders loading) and micron size BFO particle (compacted, sintered and crushed nano BFO) were also conducted to obtain the dye decolourisation profile under a solar simulator AM=1.5 as shown in figure 4.21. The photodecolourisation rate for the blank RhB dye solution and RhB dye solution loaded with a micron size BFO were similar, with no significant decolourisation of the RhB dye solution (about 5% decolourisation).

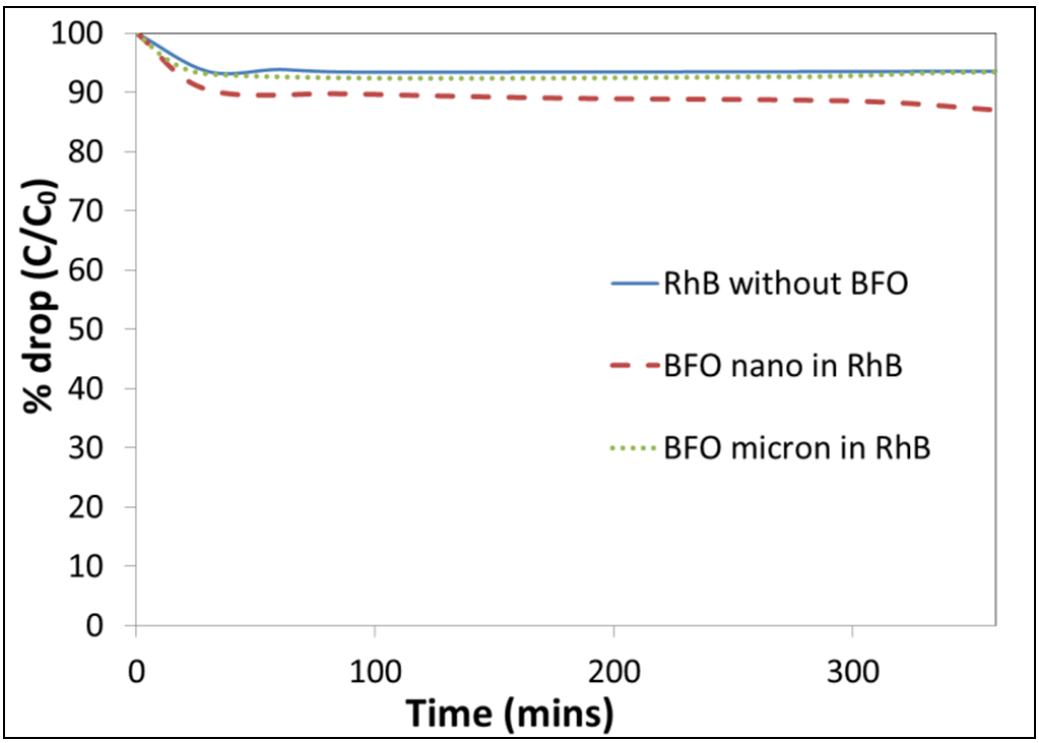

Figure 4.21 Photodecolourisation profile of RhB dye solution without BFO loading, with nano and micron size BFO loading under solar simulator AM=1.5

As shown in a previous experiment that the BFO were not able to degrade Rhodamine B dye molecules at normal pH environment (pH=6.7), hence a study was made to understand the surface charge of the BFO nanopowder by measuring the zeta potential of the BFO nanoparticle dispersed in the DI water at 0.1 wt% concentration at various pH value as shown in figure 4.22. The Zeta potential measurements indicated that at a pH of 6.7, the neutral pH of the RhB solution in water, the BFO particles exhibited a strongly negative zeta potential of -16mV. Changing the pH to strongly acid (pH2.2) reduces the zeta potential to -1.62mV. The isoelectric point when extrapolated would be at pH=2. This indicates that the BFO nanoparticles zeta potential reduces as the pH value is lowered towards zero surface charges at pH 2.

The Zeta potential is the electric potential in the interfacial double layer at the location of the slipping plane against the bulk fluid away from the interface. Hence, the zeta potential result indicates that the synthesized BFO nanopowders has an overall positive surface charge attracting negatively charged co-ions (OH^-) from the solution at normal pH environment (pH=6.7) to form a surface screening layer by co-ions as shown in figure 3.9. When the pH value reduces, the negative co-ions are countered by the positive ions (H^+) reducing the zeta potential value. This indicates that the surface screening layer by co-ions is reduced.

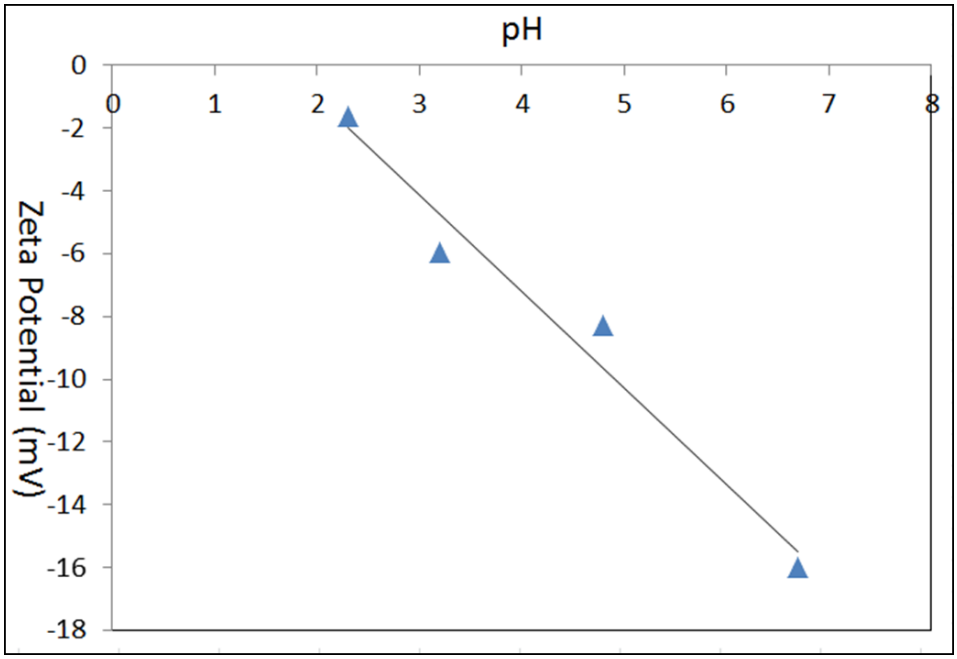

Figure 4.22 Zeta potential measurements indicating a reduction in the surface charge with a decrease in pH value.

The RhB dye molecule has a bulky aromatic molecular structure behind the cationic site when dissociated in an aqueous environment. Rhodamine B is a chemical compound usually considered as basic as it has an overall positive charge. A representative schematic model of the Rhodamine B dye is shown in figure 4.23(b) which will be used in the illustration of the dye molecule – the BFO particle surface interaction describing the interaction mechanism of particle surface charge and the dye molecule during photodecolourisation at a different pH environment.

The cationic site would be attached to the negatively polarized or C- face of the ferroelectric BFO nanoparticle surface, if the screening layer by co-ions at the particle surface is minimum by adjusting/reducing the pH environment of the dye solution.

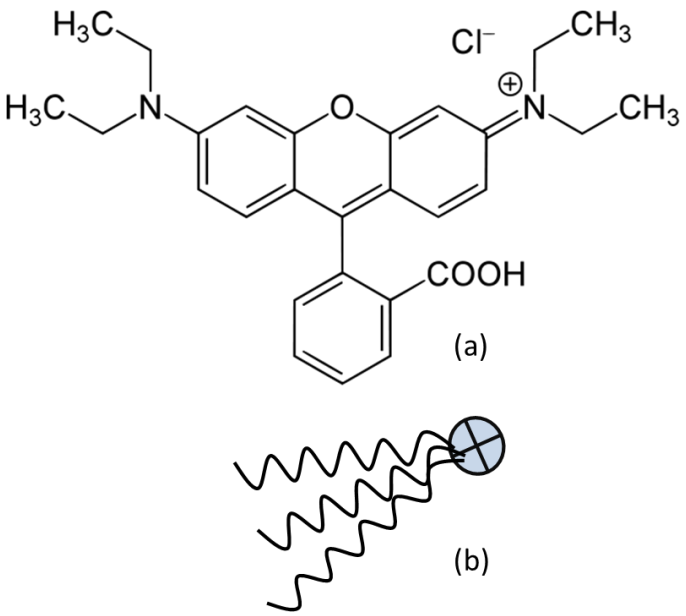

Figure 4.23 RhB dye molecule structure with a bulky molecular structure at the back of the cationic attachment site when dissociated in an aqueous environment (a), and (b) representative schematic diagram of RhB dye molecule

The results of the RhB dye adsorption in various pH values is shown in figure 4.24. To determine the extent of adsorption of the RhB on the BFO nanoparticles, the BFO nanoparticles in the Rhb dye suspension were mixed at 0.3g BFO/100 mL concentration into the RhB dye solution of various pH values (2, 4, 7 and 10) constantly stirred for 2 hours under dark conditions to prevent any occurrence of photo redox reaction. The BFO-RhB dye suspension was centrifuged to separate the dye and the BFO particle and was followed by the absorption measurement with the UV-Vis Spectrophotometer to obtain the absorption intensity of the RhB dye solution.

At pH values 10, 7 and 4, the adsorption of the RhB dye on the BFO nanoparticle is negligible. As the pH value was lowered to 2, the RhB dye solution colour intensity dropped (decolorize) indicating that the dye molecules were absorbed on the BFO particle surface at about 30%. The RhB dye molecule

absorbed the most on the BFO particle surface at pH 2 environment and resulted in more RhB molecules degradation under solar simulator illumination (AM=1.5). This support the observation by the work of Guo *et al*,[163] as Guo reported this earlier. They found that the influence of pH value on the adsorption of the RhB on the surface of the BFO to maximum at pH 2, and may be beneficial in promoting the photocatalytic efficiency.

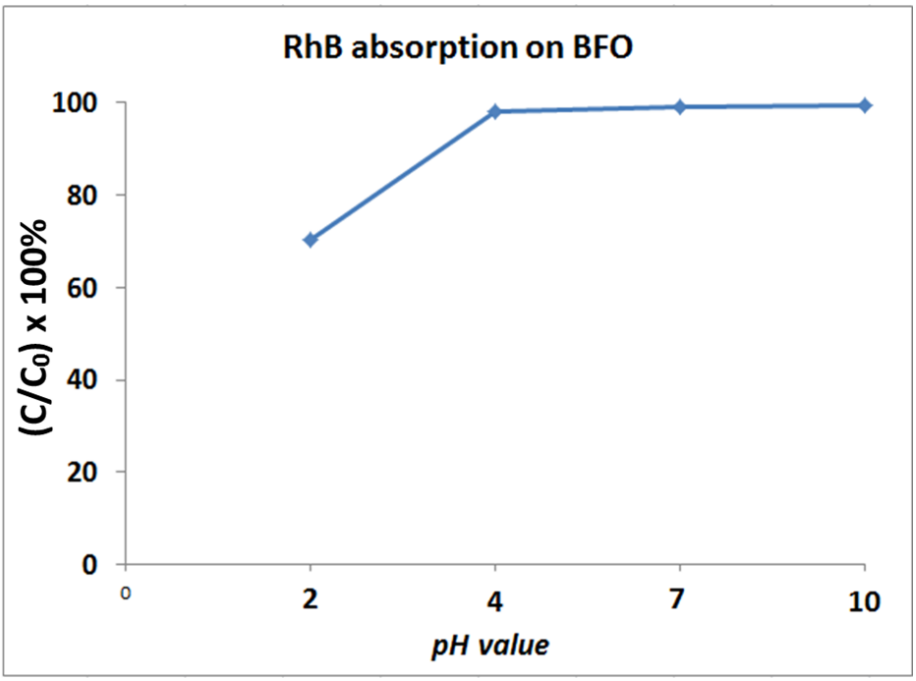

Figure 4.24 Absorption of the RhB molecules on BFO particle surface without solar simulator illumination at various pH values.

The measured zeta potential of the BFO particle surface is -16mV, hence the surface of the BFO particles are overcrowded due to development of the negative charge co-ions screening layer on the BFO particle by OH^- ions presence in the suspension as shown in figure 4.25. Such a screening layer of negative charge co-ions at particle surface could prevent the adsorption of the dye molecules onto the particle surface to decolourise the dye through direct photo-redox reaction, as well

as prevent the formation of suitable reactive species to efficiently decolour the dye. In this instance, the RhB dye molecules were prevented from attaching the BFO surface and evidenced by a minimum amount of the RhB photodecolourisation.

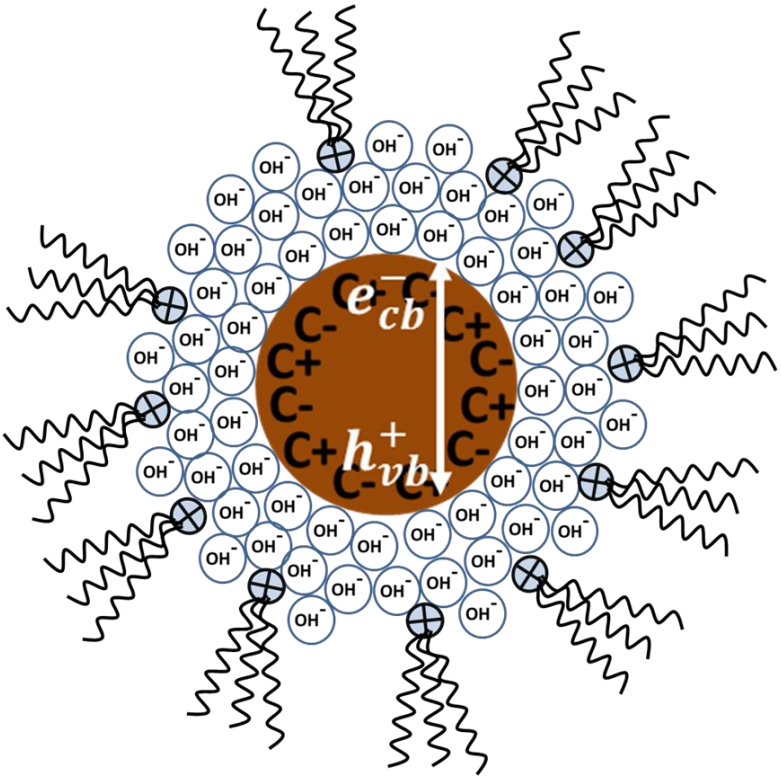

Figure 4.25 Illustration of ions interaction in the suspension containing the cationic RhB dye molecules with the random polarization surface of the BFO particles at pH 6.7, presence of negative charge ions overcrowded (co-ions screening layer) at the BFO particle surface preventing direct adsorption of the RhB dye molecule on the BFO surface.

As the pH value was brought down to 2, the BFO particle surface reached an iso-electric point, hence the ion screening layer diminished allowing the RhB dye molecules adsorbed at the BFO surfaces as shown in figure 4.26, and this is evidenced by the high amount of the RhB dye adsorption to the BFO nanoparticles (~30%) as shown in figure 4.24.

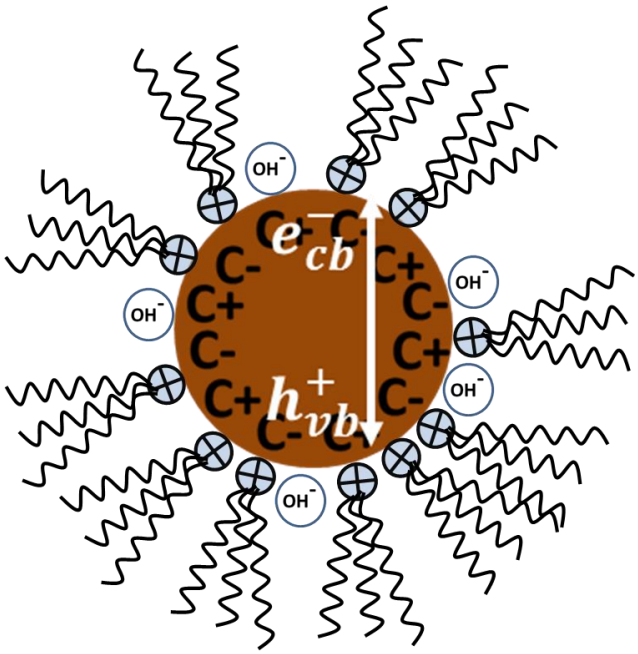

Figure 4.26 Illustration of the ions interaction in the suspension containing the cationic RhB dye molecules with the random polarization surface of the BFO particles at pH 2. The RhB dye molecules adsorbed at the surface of the BFO particles when the screening layer diminished at an isoelectric point (pzc = point of zero charge).

The photo decolourisation of the RhB dye was performed using the synthesized BFO nanopowders at a pH of 6.7, 4.0 and 2. A representative example of dye decolourisation over the BFO nanopowders at pH 2, 4 and 6.7 is shown in Figure 4.27. At pH 6.7, after 360 minutes illumination with a solar simulator (AM=1.5), the maximum decolourisation of the RhB dye is at 15%, and at pH 4 the maximum decolourisation is at 50%, and at pH 2 the maximum decolourisation of the RhB dye is completely decolourised (~99%)

.

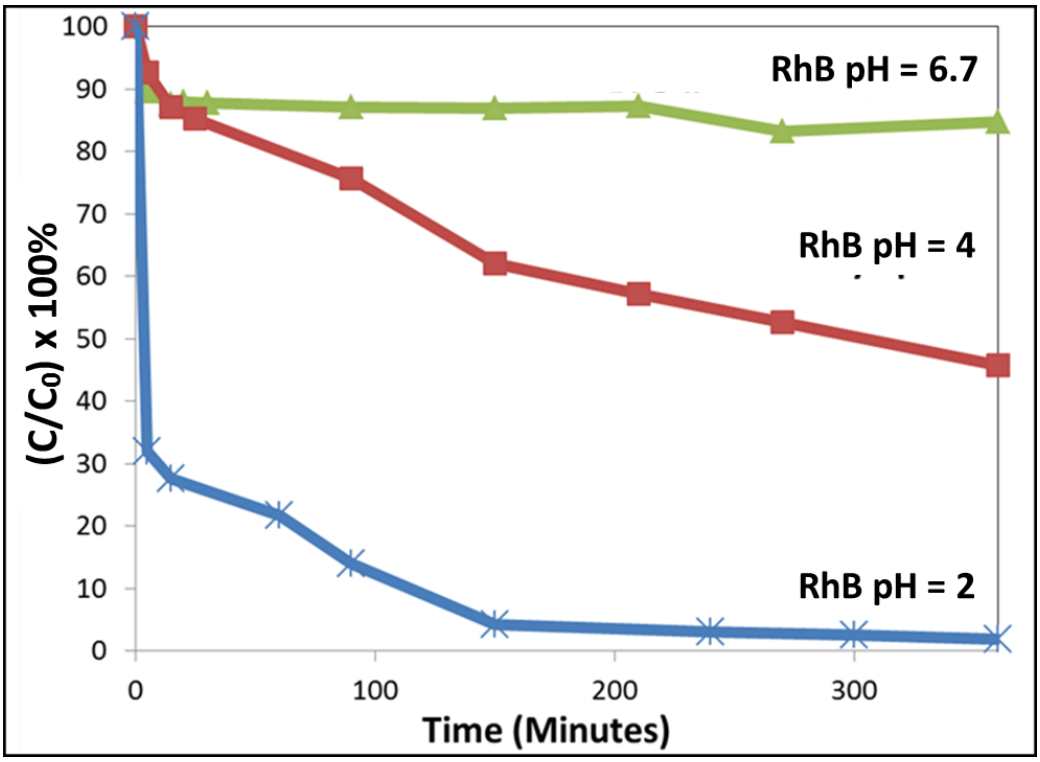

Figure 4.27 Decolourisation profiles for the RhB with the $BiFeO_3$ nanoparticle reagent under a simulated visible light (AM1.5) illumination. Two distinct reaction rates are observable, one a function of pH the other largely independent of the pH with a lower rate of dye decolourisation.

There are two trends visible from the photodecolourisation profile of the Rhb dye at various pH with the BFO. Initial trend shows that there is a clear relation between the initial rate of decolourisation and the pH values of the dye solution. The second rate is slower and the second reaction rate being largely independent of pH. In all cases of photodecolourisation experiments, equilibrium absorption of RhB on the BFO was achieved before the system was illuminated. There was an initial rapid decolourisation of the dye followed by a slower reaction rate. A photocorrosion or oxidation of the BFO catalyst was thought to be the main reason for the change in the photodegradation rate.

A blank test experiment on the RhB dye at various pH levels was conducted to ascertain that the RhB dye did not self-degrade in a low pH environment under illumination. As shown in figure 4.28, after 6 hours illumination without the BFO, the degradation rate of the RhB at pH 6.7, 4 and 2 were less than 5%, 10% and 12% respectively. The results showed that the self-degradation of the RhB is extremely slow and has no measurable decolourisation in the 6 hours timeframe, implying that the RhB is still stable even under an acidic condition (pH = 2), this was expected for a photostable dye compound.

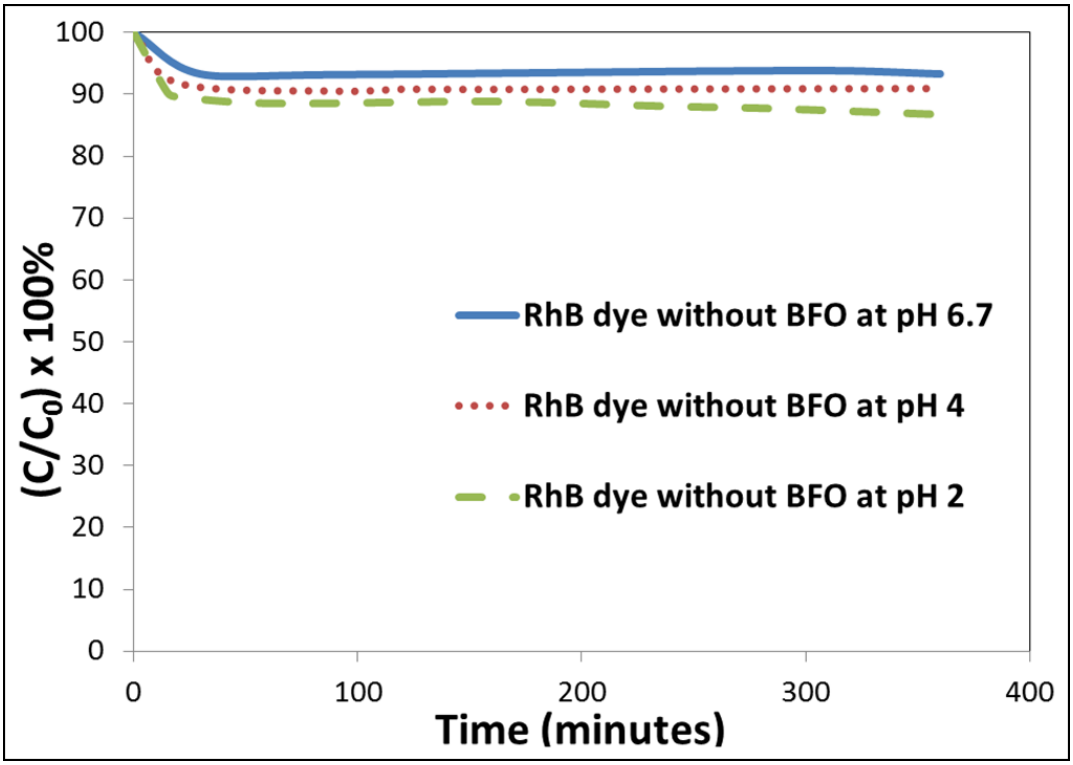

Figure 4.28 Photodecolourisation of the RhB dye at various pH values without the BFO catalyst under a solar simulator illumination (Blank Test).

To ascertain that mechanocatalystic influences were not responsible in all cases of photodecolourisation of the RhB dye at a different pH value, the photodecolourisation experiments were conducted on the BFO nanoparticle in the

RhB dye solution at a different pH value without illumination by a solar simulator. It was found that no dye decolourisation occurred within the 6 hour time frame as shown in figure 4.29. The degradation of the RhB with the BFO nanoparticles in the dark condition for the 6 hours is similar to that of the blank test (figure 4.28), which indicates that the absorption of the RhB on the BFO is limited after the equilibrium adsorption-desorption at the surface was reached. The photodecolourisation experiment for figure 4.27 are done after the adsorption-desorption equilibrium is reached in 2 hours without illumination.

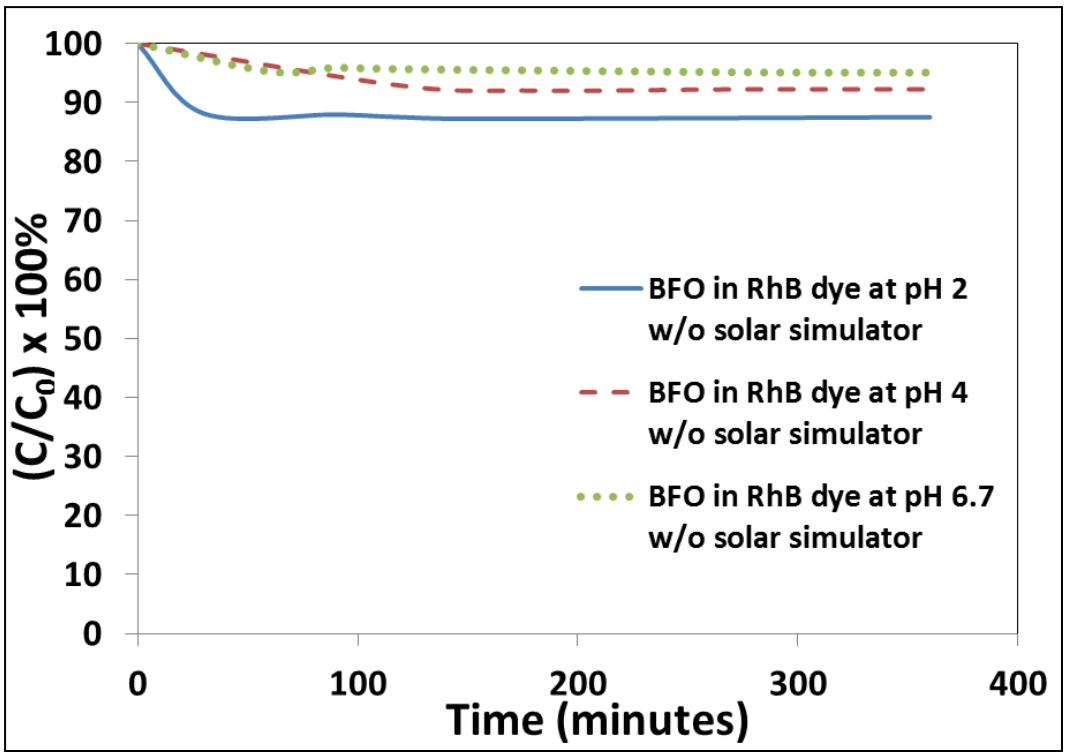

Figure 4.29 Photodecolourisation of the BFO in the RhB dye at a different pH value, without illumination.

Hence, for all pH values of the Rhb dye solution, there were negligible decolourisation of the dye without solar simulator illumination in the presence of the BFO powders and also insignificant decolourisation of RhB dye in the

timeframe of the experiments under illumination in the absence of BFO nanopowders.

Indicative band positions of the BFO relative to the accepted positions of the NHE, water and the RhB are shown in Figure 4.30. It is important to note that the band bending of the ferroelectric is controlled not by the exchange of carriers across the interface like in a traditional semiconductor (e.g. TiO_2), but by the internal field driven by the spontaneous depolarisation field. Hence, in this case the band diagram of the conventional non-polarisable semiconductor is not valid. It is supported by earlier work of Rohrer et al[12] shown that the BFO exhibits a spatially selective photochemistry. For a traditional semiconductor, it is typical to experience movement of free carriers due to the differences in the interface chemical potential that result in band bending when in contact with an ionic solution. However, in ferroelectric materials the internal polarisation fields screen the surface charge by drawing electrons to the positive C+ face and holes to the negative C- face.[26] Thus, these regions of carrier accumulation induce bending at the surface causing downward bending at the C+ face and upward bending at the C- face as shown in the indicative band structures of the BFO (figure 4.30).[12] Reduction will occur at the C+ face due to electron accumulation and oxidation at the C- face.

The energy band structure indicates why there may be some instability in a photoexcited BFO aqueous solution of the RhB. In the band diagram, the valence band of the BFO lies above the lower energy levels of both the dye and the water. As the valence and conduction band of the BFO do not ‘pinch’ the reactive species, there is instability in the system at the interface. This instability is characteristic of

semiconductor systems that are liable to photocorrosion. The band structures show that it is not possible for the BFO to inject holes into the RhB dye due to the alignment of the bands; however, the RhB dye molecules are able to inject holes into the BFO. This leads to the oxidation of the BFO and initiates photocorrosion. This photo instability due to the band alignment between the catalyst/reagent to reactant is a well-known problem for many narrow band gap semiconductors such as CdTe, and has been a significant limiting factor in the development of visibly active systems. The BFO nanopowders after photodecolourisation showed a slight colour changes to lighter brown indicating that some reactions might occurred at the particle surface.

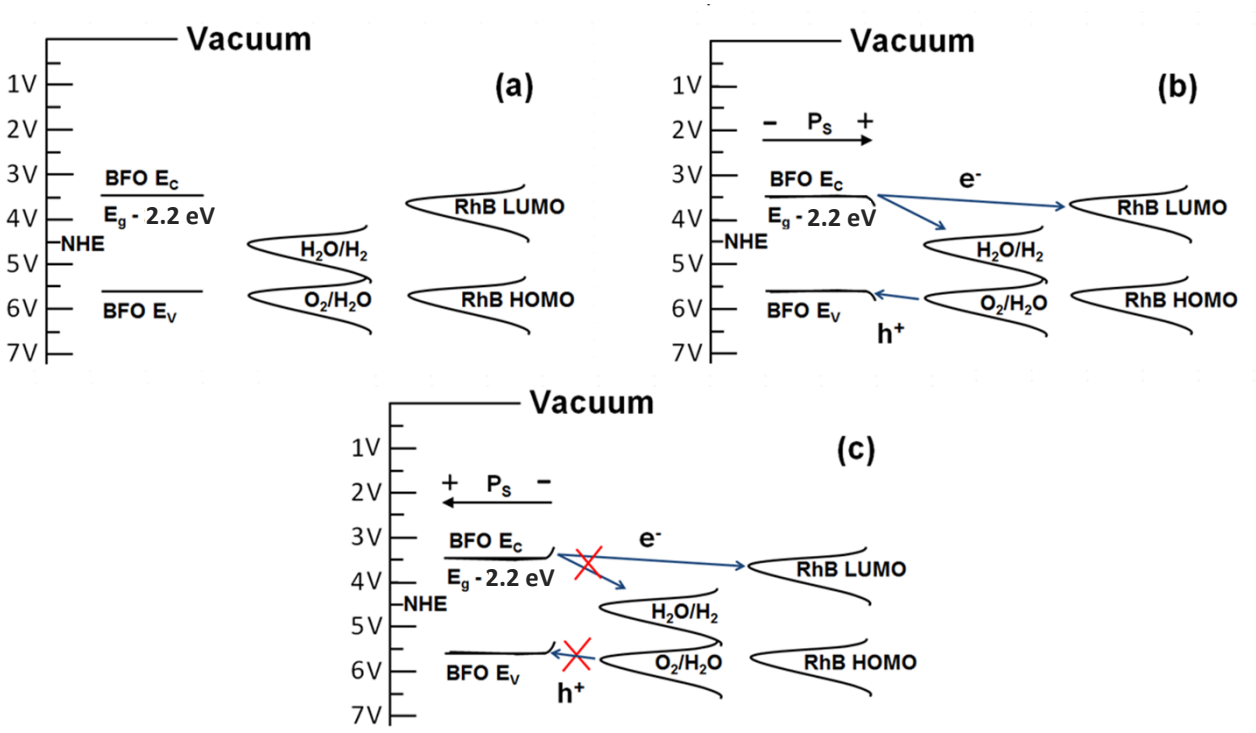

Figure 4.30 Indicative band alignment illustrations for the $BiFeO_3$ in an RhB aqueous environment. The band bending of the $BiFeO_3$ has been drawn as flat in (a) but drawn according to ferroelectric dipole interactions in (b) and (c) indicating the transfer of excited carriers between proximal species.

Nanostructured BFO had shown promise as a photochemical reagent under visible light, an experimental method was developed to mitigate the photocorrosion problem of the BFO and determine the extent to which the BFO could be used in a photochemical reaction to decolourise a typical dye compound.

To mitigate the photocorrosion effect of the BFO nanoparticle, a series of dye decolourisation experiments were conducted with the replacement of the BFO nanopowders at regular intervals, every minute, into the dye solution. The results, shown in Figure 4.31, indicate that decolourisation of the RhB at pH 2 condition is more than 95% after 10 minutes of illumination under simulated solar irradiation with the presence of BFO and replaced at every minute interval. The decolourisation performance for the BFO at pH 6.7 shows that the decolourisation up to 90% within 20 minutes time interval. The differences in the performance for the BFO with different pH values were explained earlier, which is due to the interaction of the reactive species with the BFO surface charge.

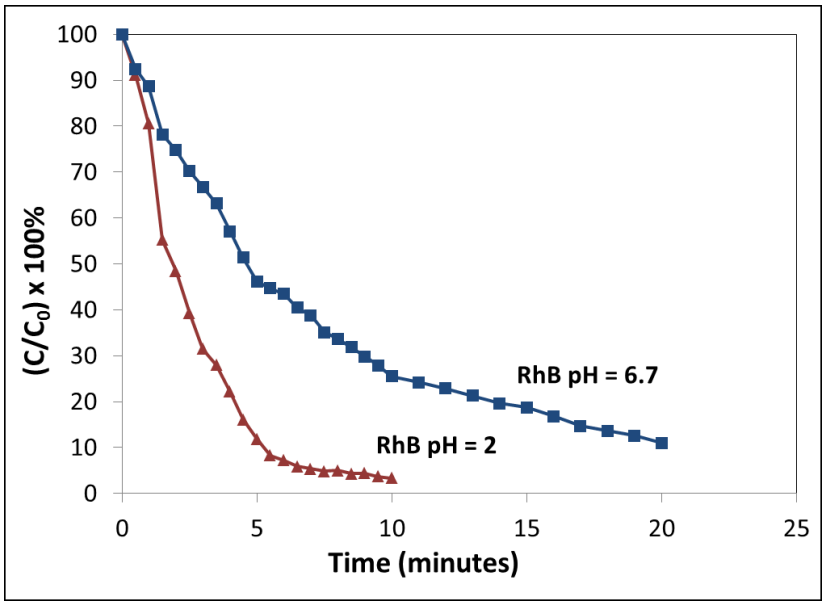

Figure 4.31 Photodecolourisation of the RhB over the $BiFeO_3$ at pH 2 and 6.7 under AM1.5 illumination. Decolourisation at pH 2 shows greater than 95% decolourisation after 10 minutes.

This experiment shows that the photodecolourisation rate performance of the BFO in the RhB dye pH 2 solution is better than the photodecolourisation of the RhB dye by nano TiO_2 (degussa P25) as shown in figure 4.32, and the performance of the BFO in the RhB dye ph 6.7 solution closely matched to the nano TiO_2. The photodecolourisation of the RhB dye was also performed with the nanoparticle of the TiO_2, the conventional semiconductor photocatalyst materials as a benchmark for the photodecolourisation of the RhB dye experiment conducted as shown in figure 4.31. The TiO_2 is a wide bandgap semiconductor material and its band structure against normal hydrogen electrode potential (NHE) is favourable to decolourise the RhB dye molecules as the band structure of the TiO_2 pinch the RhB dye HOMO-LUMO band structure. Hence, the complete photo-redox reactions could occur. Under a solar simulator (AM=1.5) illumination, the nanoparticle TiO_2 is able to decolourise the RhB dye almost completely (>95%) within 30 minutes time frame.

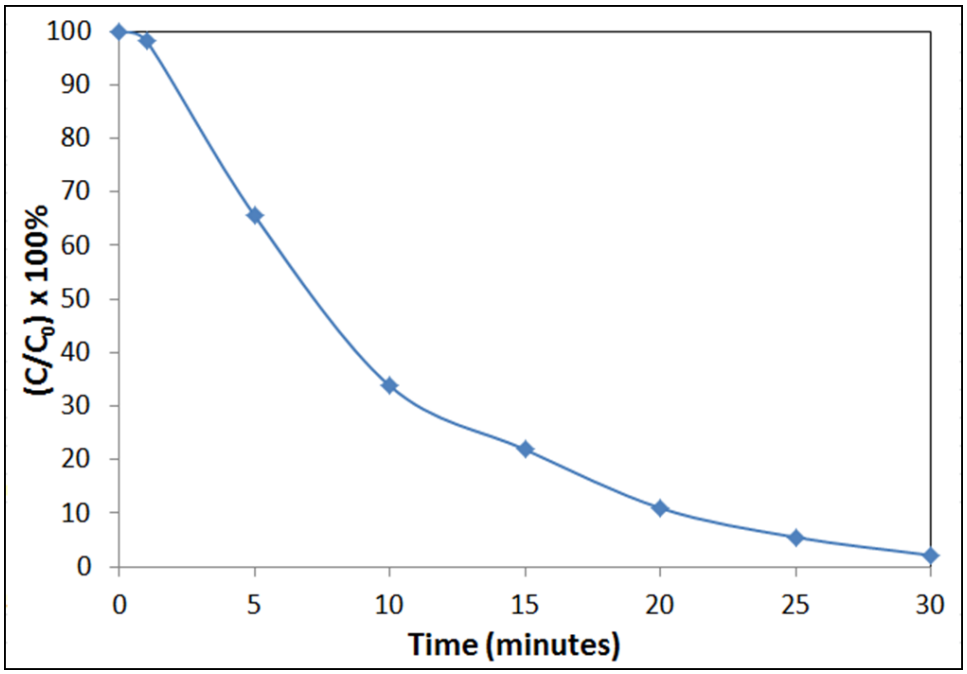

Figure 4.32 Photodecolourisation of the RhB over the nanostructured TiO_2 (Degussa P25) under the AM1.5 illumination for comparison.

Samples of the BFO powder in the RhB dye before and after the illumination were measured using x-ray diffraction (XRD) and x-ray photoelectron spectroscopy (XPS) to characterize the chemical or structural changes in the BFO after 6 hours photodecolourisation experiment. The x-ray diffraction data, shown in Fig 4.33, indicated no change before and after illumination for 6 hours, while the XPS data, shown in Fig 4.34, shows considerable changes. The lack of change in the crystallography is attributed to the nature of the technique. X-ray diffraction produces data averaged over the full penetration of the x-rays used and is not surface sensitive.

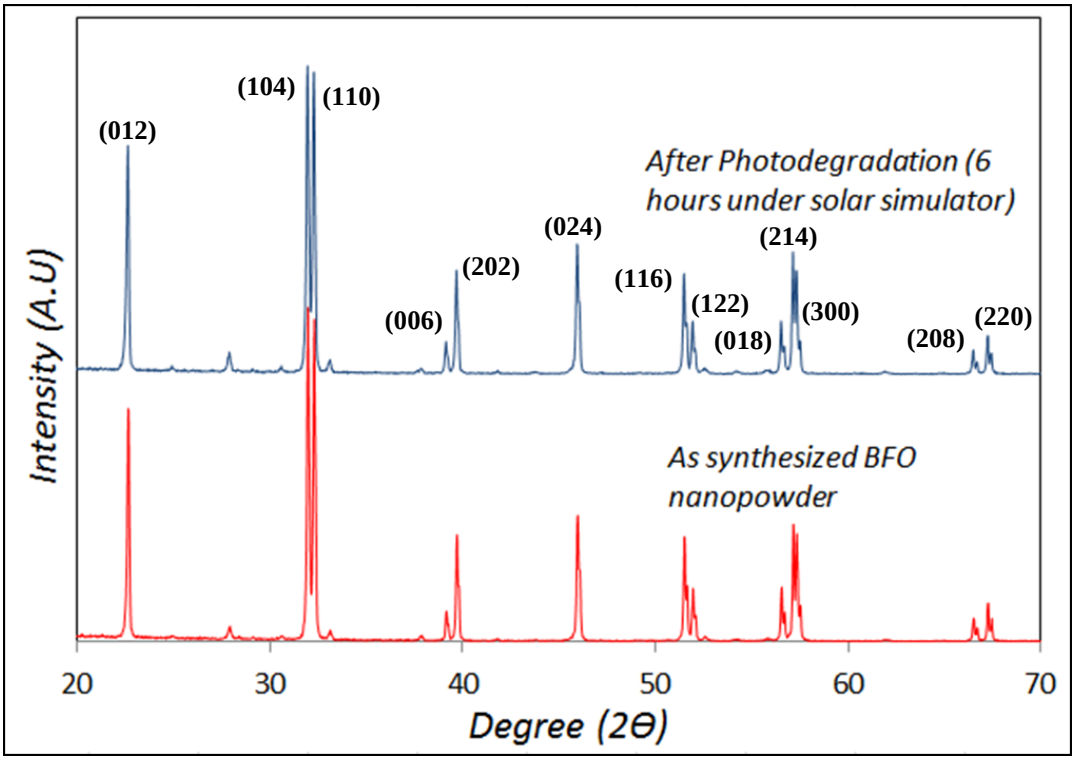

Figure 4.33 XRD patterns of the $BiFeO_3$ before and after illumination indicating no noticeable change.

XPS is a highly surface sensitive technique and returns information about the chemical environment at the surface. The XPS data, Fig 4.34, shows typical spectra for a prepared sample of the BFO and in agreement with another report by Popa et al.[164] In the XPS spectrum of the BFO, the position of the Fe 2p is expected to be at 711 eV for the Fe^{3+} ion and 709.5 eV for the Fe^{2+} ion. The 3/2 and 1/2 spin orbit doublet components of the Fe2p photoemission located at 711.5 and 725.8 eV respectively.

A comparison of the spectra obtained for the samples before and after illuminated at pH 6.7 indicates that there is a significant change in the chemical environment of the Fe^2p (change in the Fe^{2+}/Fe^{3+} ratio) and no visible changes in the environment for the Bi_{1F} and O_{1S}, see figure 4.34 (a) – (c) The BFO has been considered as a solid solution of the oxides of Fe and Bi and in this case the Fe-O bonds are the least stable and so most likely able to corrode. Hence, it is likely that the pathway for photocorrosion is the dissolution and breaking of the Fe-O bonds to effectively etches the Fe from the surface of the BFO lattice.

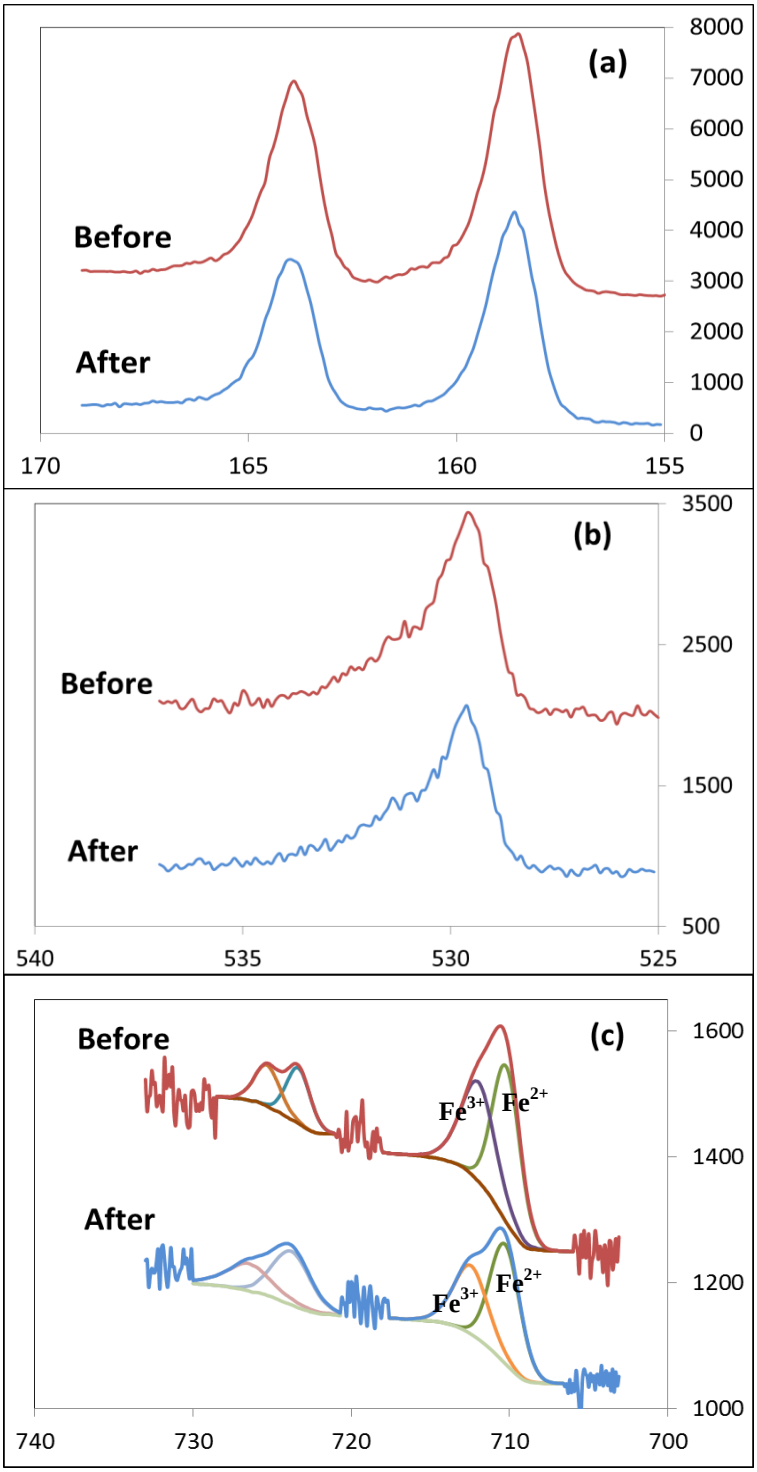

Figure 4.34 XPS spectra for the $BiFeO_3$ before and after exposure to irradiation in the RhB pH 6.7 solutions. (a) indicates the Bi_{1F} peak with a slight shift in peak position, (b) the O_{1S} peak with some minor changes to the peak shape and position,, and (c) the Fe_{2p} peak showing a significant change in the relative ratios of the Fe^{2+}/Fe^{3+} peaks after illumination.

Energy Dispersive Spectroscopy measurement were performed on samples before and after the photodecolourisation experiment to ascertain the chemical change in the BFO. While the EDS spectra cannot be considered as quantitative results, the EDS obtained during the SEM analysis does show a drop in the Fe atomic% of 3.5% across an average of 5 samples after illumination (see Table 4.2). The atomic% of Bi and O increased to compensate for the drop in the Fe content.

	Before Photodegradation						After 6 hours Photodegradation					
	Bi		Fe		O		Bi		Fe		O	
S/No.	At%	Wt%	At%	Wt%	At%	Wt%	At%	Wt%	At%	Wt%	At%	Wt%
1.0	22.3	65.3	30.9	24.2	46.8	10.5	22.5	66.2	29.1	22.9	48.4	10.9
2.0	22.6	64.8	33.1	25.4	44.3	9.7	22.9	67.1	27.7	21.8	49.4	11.1
3.0	24.4	66.0	35.7	25.8	39.9	8.2	22.0	65.6	29.2	23.3	48.7	11.1
4.0	23.3	65.9	32.4	24.5	44.3	9.6	22.7	66.5	29.0	22.7	48.4	10.9
5.0	22.1	65.2	30.7	24.2	47.2	10.6	24.0	67.6	29.9	22.5	46.1	9.9
Average	23.0	65.4	32.6	24.8	44.5	9.7	22.8	66.6	29.0	22.6	48.2	10.8

Table 4.2 Energy Dispersive Spectroscopy data of the BFO particle elemental composition showing the Bi, Fe and O elements before and after the photodecolourisation experiment with the RhB dye (pH 6.7)

When the Fe is removed from the crystal lattice due to photocorrosion, this would cause the material's surface highly defected at a crystallographic level and thus induce a number of charge trap states into the band structure. The ferroelectric properties at the surface of the BFO will be disappeared, while bulk region would be presumed still have the ferroelectric properties. This change of the BFO surface properties would change the interaction between the BFO and the dye during exposure to light illumination. The adsorbtion of dye molecules onto BFO surface would be affected due to the loss of ferroelectric nature at BFO surface, and also the

surface of the BFO then becomes less suitable for the production of a reactive species and slows the rate of the RhB dye decolourisation. Therefore, the photocorrosion of BFO surface could be the reason for the reduction in reaction rate for the decolourisation of the dye.

4.2.2 Photodecolourisation of Acid Black Dye with BFO Nanopowders

A photodecolourisation experiment on acid black dyes, which are known to be negatively charged when dissociated in water (anionic dye), was carried out. It was found that the BFO nanoparticles were able to photodegrade the acid black dyes (10ppm concentration in DI water) rapidly under exposure to a solar simulator AM=1.5 as shown in figure 4.35, and the photodecolourisation of the acid black dye only without the presence of the BFO nanoparticle (blank dye test) did not decolourise, and ascertain that the acid black dye is a photostable dye compound and its degradation is only with the presence of the BFO nanoparticle.

The photodecolourisation of the AB dye by the BFO can be attributed to the band position of the AB dye, where the HOMO – LUMO level of the AB dye is located within the band gap of the BFO as shown in figure 4.36. As such, the photo-REDOX reactions will occur and degrade the AB dye molecules that are adsorbed at the surface of the BFO. This is the case for a traditional semiconductor photocatalyst such as the TiO_2 where the band positions of the semiconductor 'pinch' the REDOX couples of available reactants and products. If the photocatalyst, or reagent, does not do this then it may be liable to photocorrosion[132],

which is in the case of the RhB dye photodecolourisation by the BFO experiment where the BFO reagent photocorroded due to the band positions between the BFO and the RhB dye (Figure 4.30). The pathway for the degradation of the AB dye could be a direct photoreduction of the adsorbed anionic AB dye molecules at C+ face where photogenerated electrons accumulated,[26,144] or through the indirect degradations pathway by the generations of superoxide anion radicals (equations 2.17-2.22).

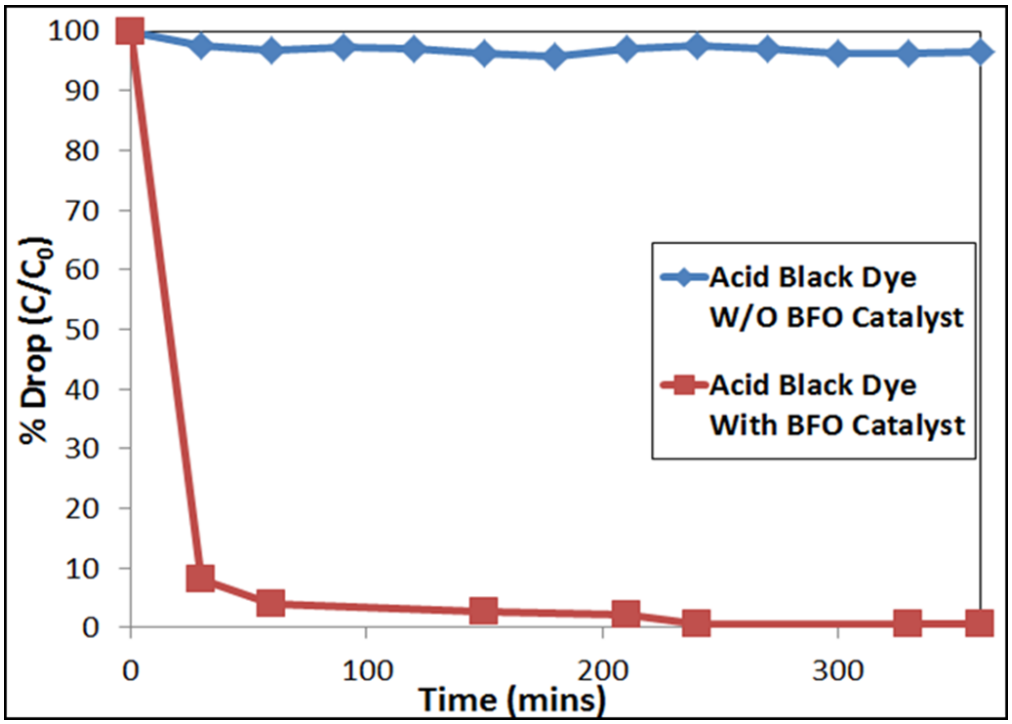

Figure 4.35 Photodecolourisation profile of the blank Acid Black dye and Acid Black dye with the BFO powder at normal pH (pH = 6.7)

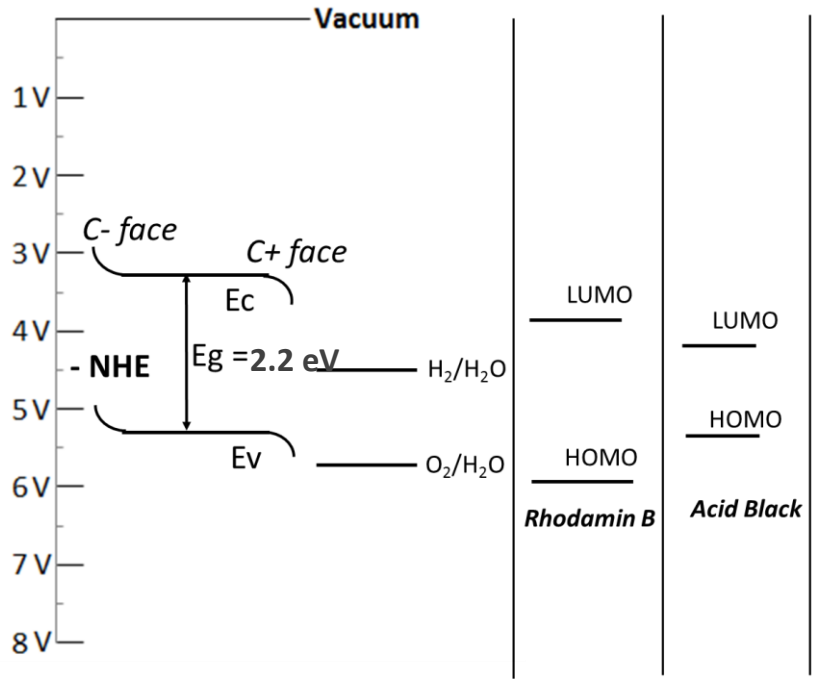

Figure 4.36 Indicative band positions for the BFO with respect to the NHE, H_2O and HOMO-LUMO positions of the Rhodamine B (RhB) and the acid black (AB) dye, with a focus on band bending due to the ferroelectric nature of the BFO.

Figure 4.37 shows the illustration of the Acid black dye molecule with a linear aromatic molecular structure with two anionic sites when dissociated in an aqueous environment. A representative schematic model of the AB dye is shown in figure 4.37(b) which will be used in the illustration of the dye molecule – the BFO particle surface interaction describing the interaction mechanism of the particle surface charge and the dye molecule during photodecolourisation.

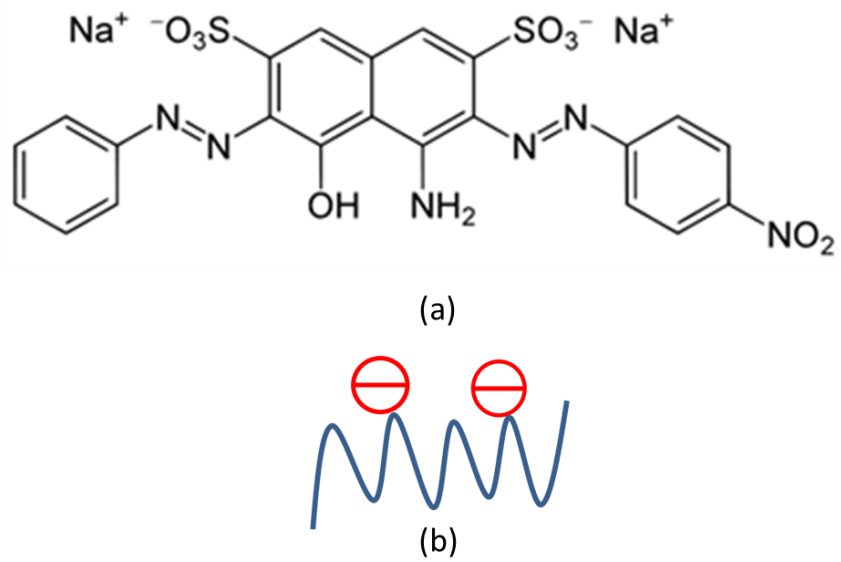

Figure 4.37 Acid Black (AB) dye molecule structure with a linear molecular structure and both the anionic attachment site at the middle of the linear molecular structure when dissociated in an aqueous environment, and (b) representative schematic diagram of the AB dye molecule

To determine the extent of adsorption of the AB on the BFO nanoparticles, the BFO nanoparticles in the AB dye suspension were mixed at 0.3g BFO/100 mL concentration and constantly stirred for 2 hours under dark conditions to prevent any occurrence of photo redox reaction. The BFO-AB dye suspension was centrifuged to separate the dye and BFO particle followed by an absorption measurement with the UV-Vis Spectrophotometer to obtain the absorption intensity of the AB dye solution.

After 2 hours, the AB dye solution colour intensity dropped (decolourise) indicating that the dye molecules were readily absorbed on the BFO particle surface at about 35% (figure 4.38). This adsorption of the AB dye may be attributed to the presence of two anionic sites that are able to adsorb to the surface of the BFO which

has a net C+ face polarization, shown by the high negative zeta potential value (-16 mV). The presence of two anionic attachment sites will provide a strong electrostatic attraction to the C+ face of the BFO surface as illustrated in figure 4.39. Hence, facilitate the degradation of the AB dye through the direct photo-REDOX reaction path for photodecolourisation of the AB dye.

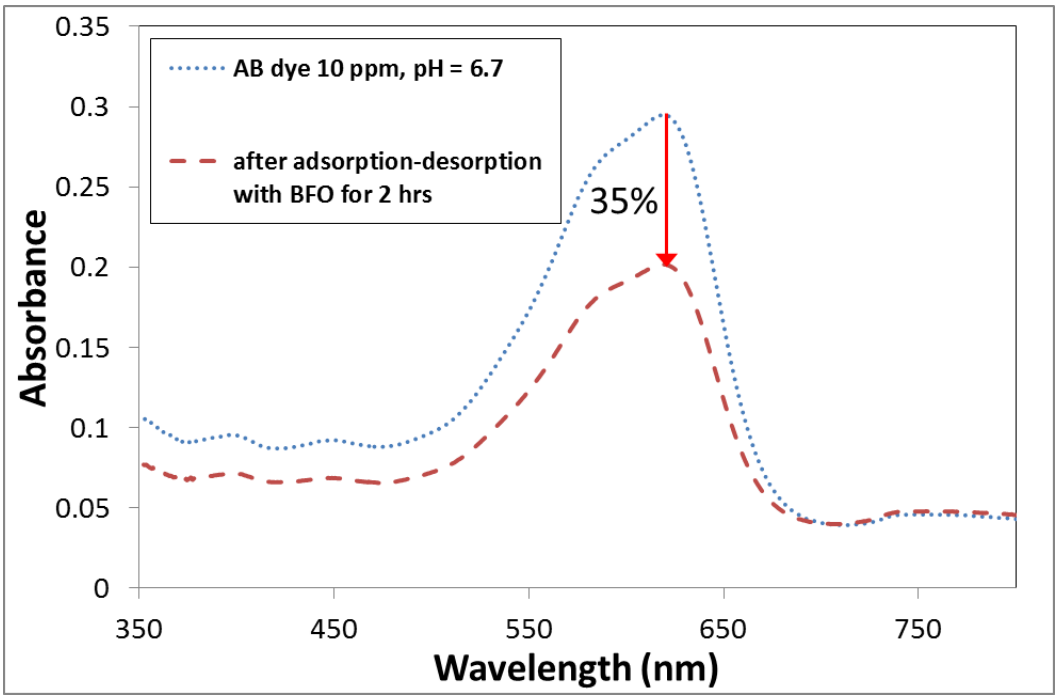

Figure 4.38 Absorption spectra of the Acid Black dye molecules before and after adsorption-desorption on the BFO particle surface without illumination for 2 hours at pH 6.7.

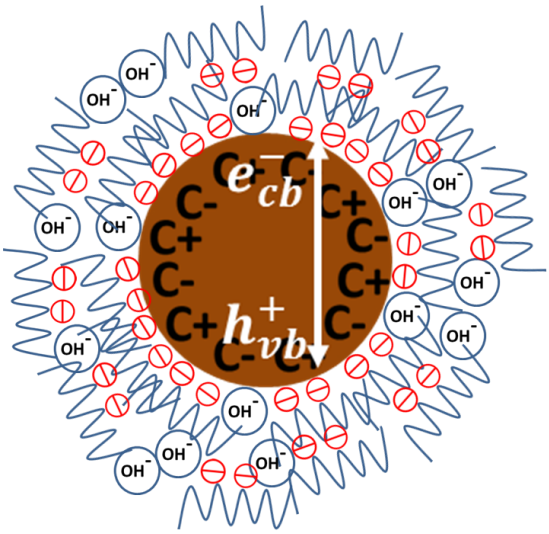

Figure 4.39 Illustration of the ions interaction in the suspension containing the anionic AB dye molecules with the random polarization surface of the BFO particles at pH 6.7, anionic AB dye molecules adsorbed together with hydroxyl (OH^-) ions at the BFO particle surface facilitates the degradation of the AB dye molecule on the BFO surface by photo redox reactions.

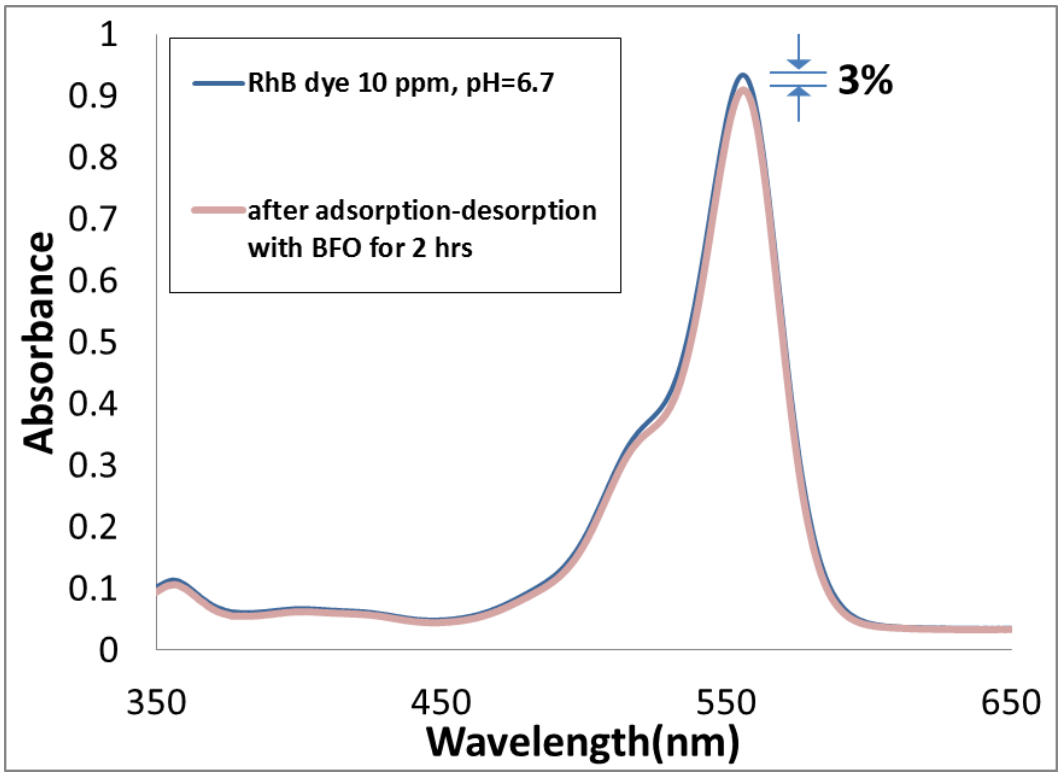

Figure 4.40 Absorption spectra of Rhodamine B dye molecules before and after adsorption-desorption on the BFO particle surface without illumination for 2 hours at pH 6.7.

Since the RhB dye which has a cationic attachment site, the predominantly C+ face at the BFO particle surface would form the negative ions screening, evidenced by the negative zeta potential preventing the adsorption of cationic RhB dye on the BFO particle surface. Hence, the possibility of the photo-REDOX reactions to degrade the RhB dye molecules is minimised. Only about 3% of the RhB dye adsorbed on the BFO surface after adsorption-desorption experiment for 2 hours as shown in figure 4.40, compared to 35% of the AB dye adsorption. The difference in the adsorption and photodecolourisation results between the RhB and the AB dye with the BFO further support the hypothesis of the presence of the stern layer and its interactions with the organic molecule species, where the anionic AB dye adsorbed more readily at the predominantly C+ BFO surface and does not induce photocorrosion due to the favourable band positions with respect to the BFO band structures.

In comparison with non-ferroelectric metal oxide, nano TiO_2 in this case, absorption test of dyes molecules on nano-TiO_2 was performed by mixing the TiO_2 nanoparticles in the dye solutions and continuously stirred under dark environment (without light illumination). It was observed that the colour intensity of the dye solution didn't have any significant drops (see Figure 4.41), and suggested that the nano TiO_2 was not able to adsorb both anionic and cationic dyes molecules, the AB dye and RhB dye molecules respectively.

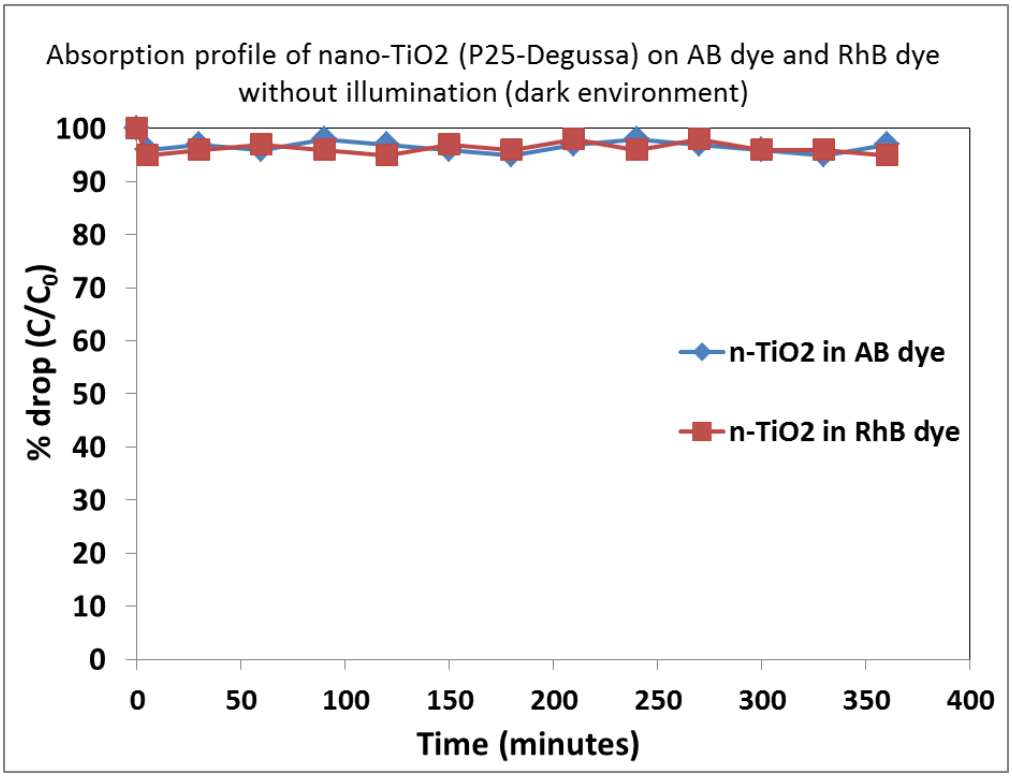

Figure 4.41 Absorption profiles of AB dye and RhB dye by nano TiO2 particle (P25 Degussa) under dark environment (without illumination) for 6 hours.

4.3 Doping of the $BiFeO_3$ and their Photodecolourisation Efficiency Assessment

4.3.1 Photodecolourisation of Copper (Cu) Doped BFO

Previous works have shown that the BFO can also be regarded as a visible-light photocatalyst for organic pollutants degradation because of its small band gap (~2.2 eV). However, the low photocatalytic activity of the BFO hinders its commercialization as photocatalytic technology.[10] Therefore, improvement of the photocatalytic activity of the BFO become an important task and gain significant research interest for practical use.

Doping is the process that intentionally introduces impurities into a pure semi-conductor with the aim to modulate its electrical properties. Recent works have shown that doping of the BFO with a dopant atom at either the A or the B site of the ABO_3 lattice could alter its properties. For example, substitution of the Bi-site with rare-earth (RE) elements, such as La, Nd, or Sm, etc. and substitution of the Fe-site with transition metal such as Ni, Cr, Ti, Mn, Sc, etc. resulted in a remarkable improvement of the ferroelectric and ferromagnetic of the BFO, such as improving the large current density leakage which could possibly lead to an enhanced ME effect.[165,166]

Figure 4.42 shows the evolution of the XRD patterns of the Cu doped BFO powder from 0.5at% to 2 at%. At 0.5at% doping concentration, the XRD patterns did not show significant changes to the original synthesized BFO powder, and as the doping concentration increased, the XRD patterns showed some deviations from original as synthesized BFO powder and showed the $Bi_2Fe_4O_9$ phase becoming more prominent, while maintaining the peaks from the original BFO powder. At 5% Cu at% doping, the $Bi_2Fe_4O_9$ and the Bi_2O_3 phases evolved together with the BFO phase. However, no Copper Oxide phase was present.

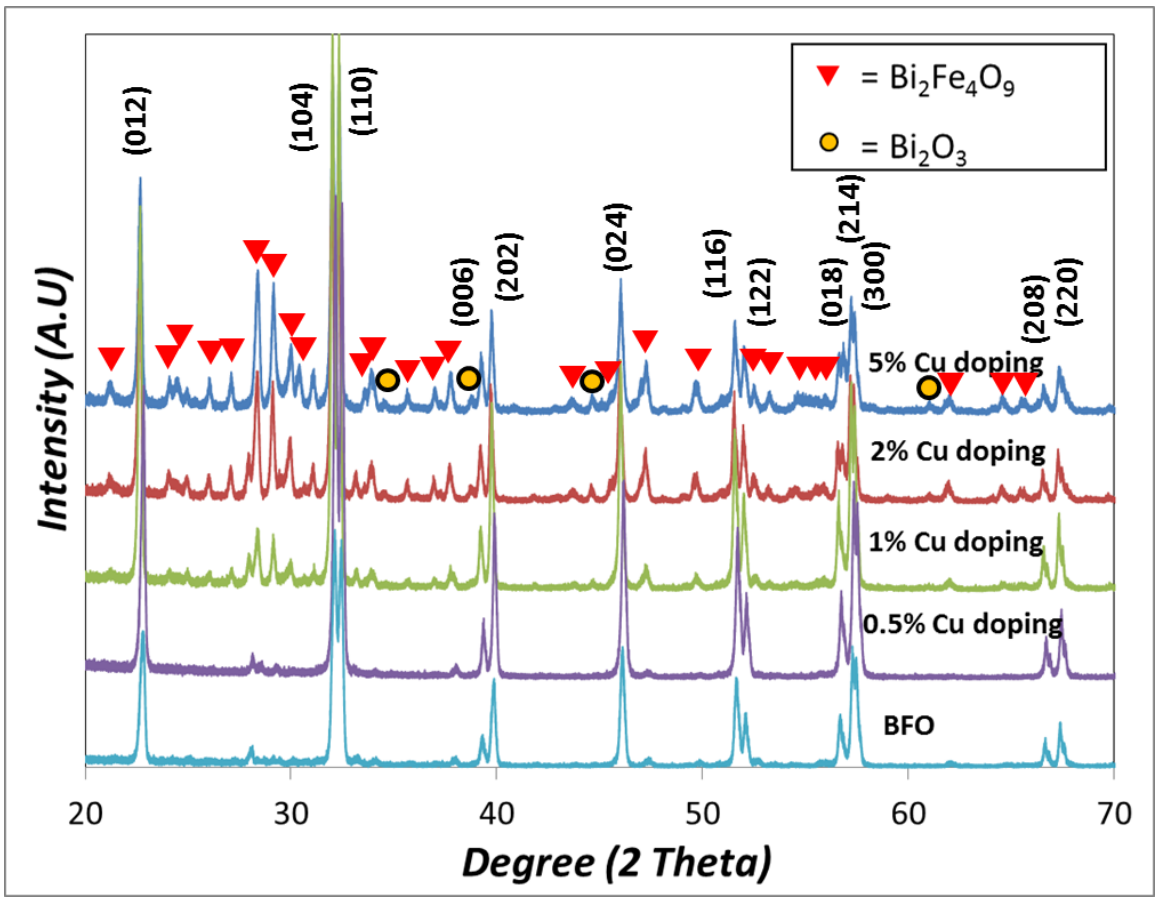

Figure 4.42 XRD patterns evolution of the Cu doped BFO powder from 0.5at% to 5at%

The magnified XRD patterns of the Cu doped BFO are shown in figure 4.43 (a) – (d). The BFO phase characteristic peaks corresponds to the crystallographic planes of (104), (110), (006), (202) at lower 2 theta angle (figure 4.43 (a) & (b)) showed slight right peak shift at 0.5at% Cu doping and at 1at%, 2at% and 5at% Cu doping, the peaks showed shifting towards a smaller 2Θ angle. At higher 2 theta angle (figure 4.43 (c) & (d)), the BFO peaks corresponds to the crystallographic planes of (018), (214), (300), (208) & (220) also showed slight right peak shift at 0.5at% Cu doping and slight left peaks shift at 1at%, 2at% and 5at% Cu doping This result suggests that the Cu atoms mixed in well in the rhombohedral lattice of

the BFO crystals with other secondary phase of the $Bi_2Fe_4O_9$ evolved that is thought due to the Cu atoms incorporation into the BFO lattice substituting the Fe element, which has been observed in other transition metals doped BFO ceramics.[167] The shift of the XRD pattern also indicates the lattice distortion due to larger copper ions doping, resulting in change of the crystallography symmetry of the BFO.

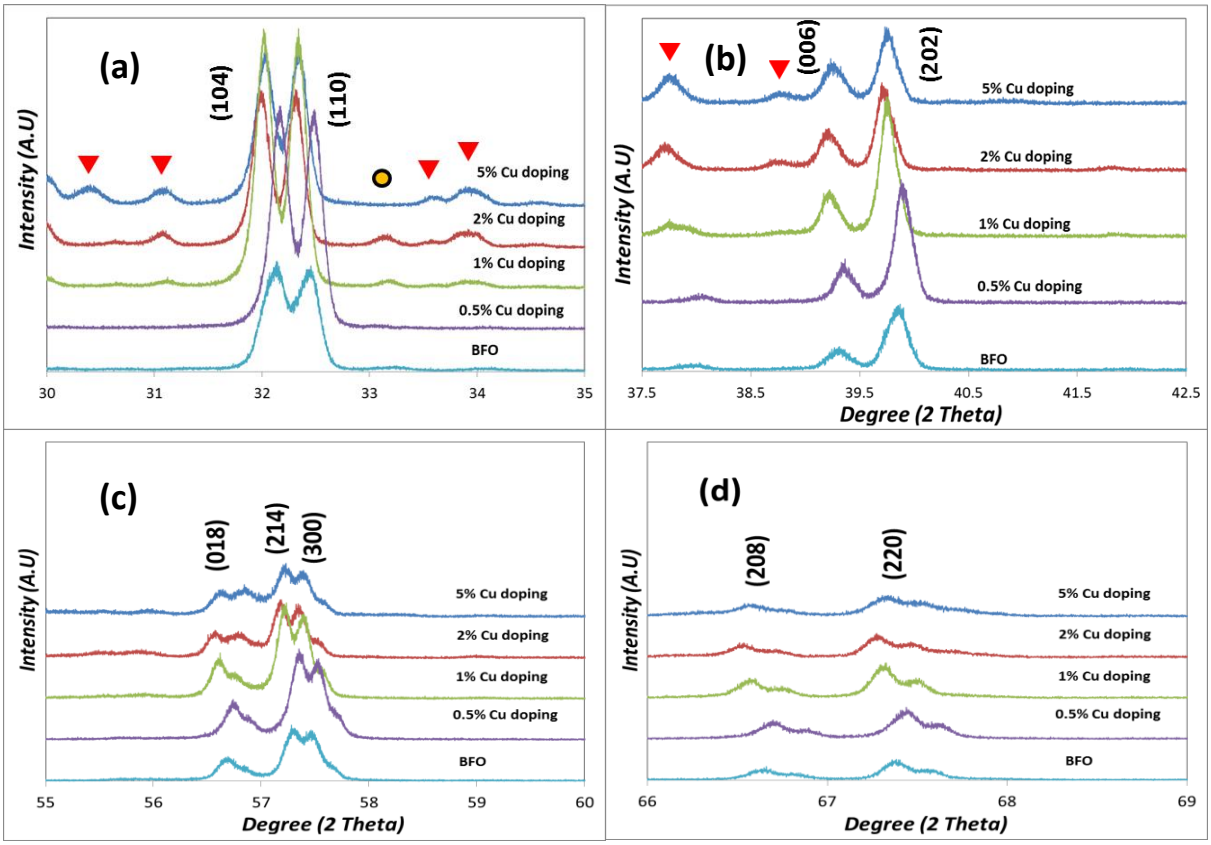

Figure 4.43 XRD patterns evolution of the Cu doped BFO powder from 0.5at% to 5at%, zoom in of (a) (104) and (110) peaks, (b) (006) and (202) peaks, (c) (018), (214) and (300) peaks, (d) (208) and (220) peaks

The X-Ray Fluorescence measurements shown and confirm the atomic concentration of the Cu elements to be at 0.5 at%, 1.at%, 2.5 at% and 4.6at% Cu concentration in the BFO particles.

Photodecolourisation experiments of the Cu doped BFO powder to the RhB dye solution at normal pH (pH=6.7) environment were conducted and found that as doping concentration increased, the photodecolourisation rate increased (figure 4.44). At 0.5at% the Cu doping photodecolourisation rate did not show significant decolourisation of the RhB dye solution, similar to the pure BFO. The photodecolourisation rate of 1at%, 2at% and 5at% the Cu doped BFO after 6 hours' time frame is at 35%, 75% and 90% decolourisation of RhB dye.

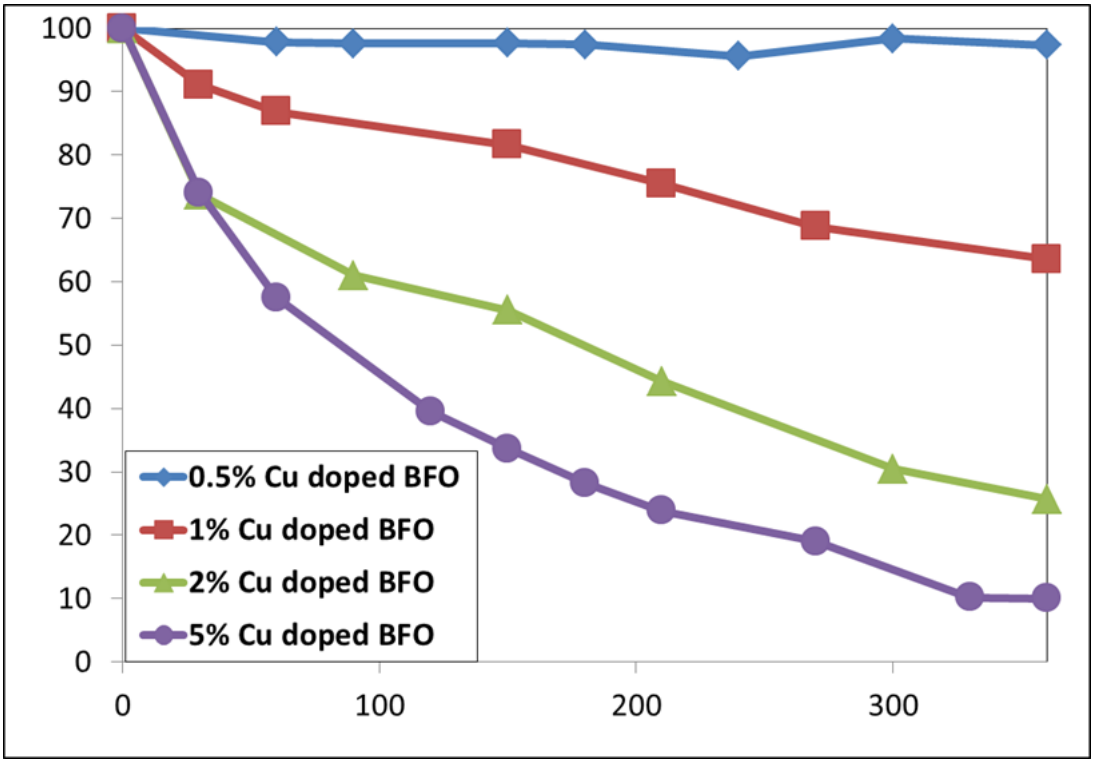

Figure 4.44 Decolourisation profiles for the RhB dye with the Cu doped (0.5% - 5%) $BiFeO_3$ under a simulated visible light (AM1.5) illumination.

Figure 4.45 shows the room-temperature magnetization-magnetic field (*M*-*H*) curves of the Cu doped BFO samples for the maximum magnetic field (*H*m) of 6 kOe. In contrast to pure BFO nanoparticles which exhibit a linear magnetization, the Cu doped samples up to 2at% Cu doping exhibit a small ferromagnetism with a

small coercivity with no hysteresis loop; however at 5at% Cu doping the hysteresis *M-H* loop behaviour is observed, see figure 4.45 a-d. Also, the magnetization of the Cu doped BFO showed an increasing trend as the Cu doping concentration increased.

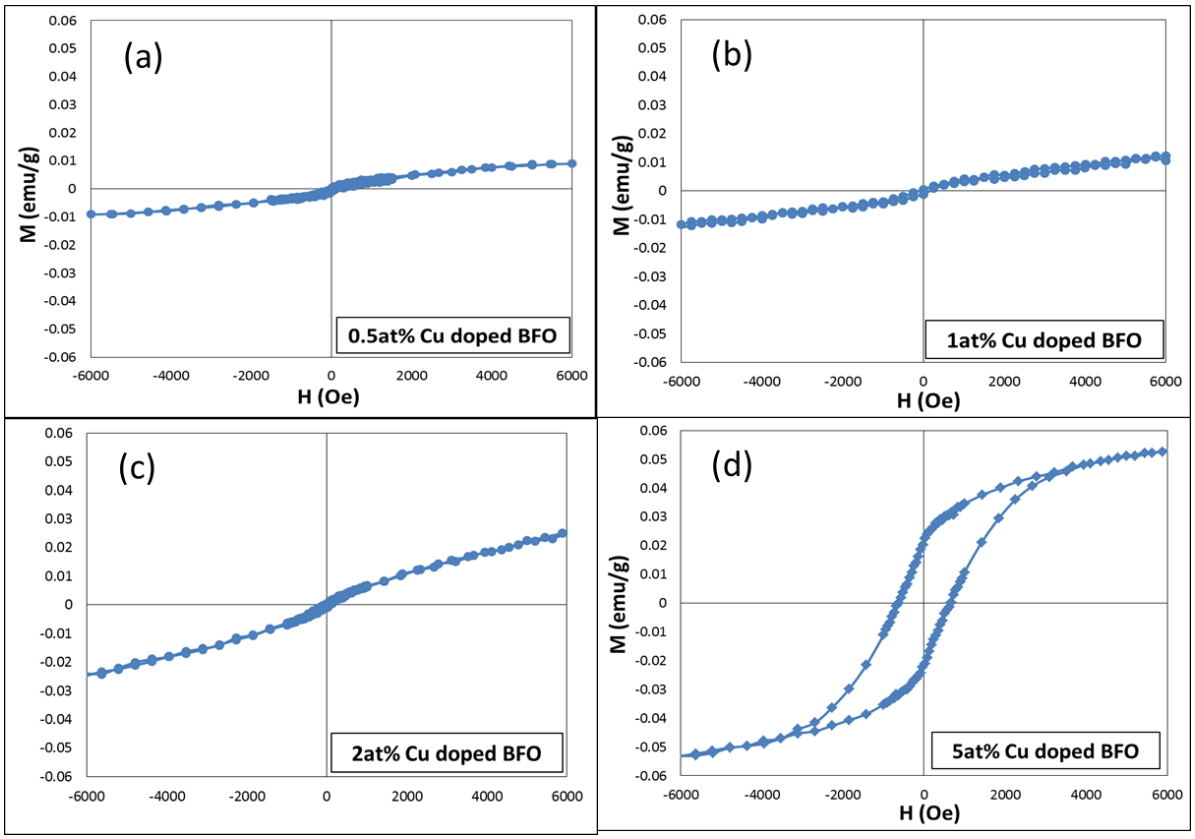

Figure 4.45 Magnetization hysteresis loops of the Cu doped BFO samples.

This ferromagnetism (FM) behaviour of the samples can be exploited for the magnetic separation of a photocatalyst after the degradation of the aqueous dye solution. The enhanced FM properties could be attributed to the fact that the substitution-induced suppression of the spiral spin modulation (spiral spin structure is partially destroyed in the BFO nanoparticles), due to the larger distortion of the lattice.[154,163,168]

It was observed in figure 4.46 that the Tauc's plot from the absorption curve of the Cu doped BFO showed a decrease in the optical bandgap as the doping concentration increased from 0.5at% to 5at% Cu doping. The optical bandgap of the Cu doped BFO decreased from 2.22 eV for the pure BFO to 2.16 eV, 2.14 eV, 2.12 eV and 2.08 eV for 0.5at%, 1at%, 2at% and 5at% Cu doped BFO respectively. The decrease of the optical bandgap might contribute to the increase in the photocatalytic property. It has been reported by Zhang *et al*[169]that the band gap of some bismuth photocatalysts decreased with doping, which might increase the photocatalytic activities.

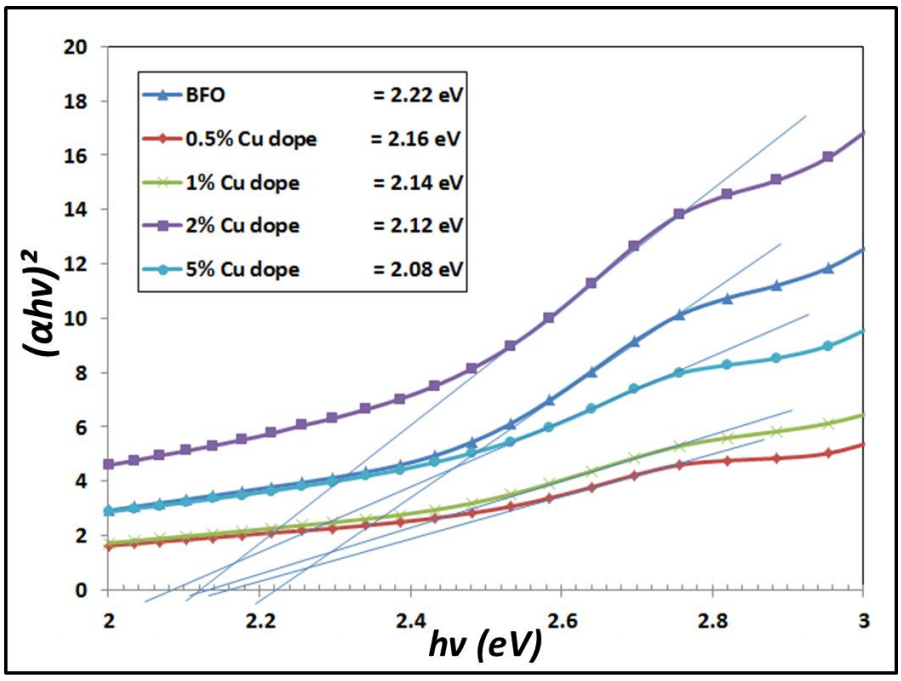

Figure 4.46 Tauc's plot of the Cu doped BFO nanopowders (0.5at% - 5at% Cu dope BFO)

Possible reasons or mechanism for an improved photodecolourisation rate of the Cu doped BFO by substituting the Cu^{2+} ions to replace the Fe^{3+} ions may be ascribed to the following factors:

- **Improved Leakage Current Density and Enhanced Internal Polarization.**

It is well known that some dopants can modify and improve the properties of ferroelectrics and ferromagnetic properties of the multiferroic BFO, such as an improved leakage current density[119,165,170] . Substituting the Cu^{2+} ions to replace the Fe^{3+} ions would reduce the leakage current density and enhance the internal polarization of the BFO. The Cu^{2+} ions substitution would obstruct the formation of the Fe^{2+} ions and control the Fe^{2+}/ Fe^{3+} charge fluctuation[171] and oxygen vacancy with two positive charges is introduced to maintain the charge neutrality[172] when two Fe^{3+} ions are substituted by two Cu^{2+} ions [Kroger– Vink notations: 2CuO-> $2Cu'_{Fe} + O_o^x + V_{\ddot{o}}$; where the Cu'_{Fe} represents the Cu ions sitting on the Fe lattice with one negative charge (electron), the $V_{\ddot{O}}$ represents the two positive charges oxygen vacancy and the O_o^x represents the zero charge on oxygen.] The oxygen vacancy can form defect dipoles with 2Cu'Fe as $[2Cu'_{Fe} \text{ --- } V_{\ddot{o}}]$[173], and these dipoles formed may lead to the decrease of the leakage current density and the increase of polarization in the BFO.[173].

In ferroelectric materials the internal polarization fields screen the surface charge by drawing the electrons to the positive C+ face and holes to the negative C- face.[26] The increased in the internal polarization due to the doping of the BFO resulted in the increase of the carriers separation by the internal polarization fields, suppresses recombination rates thereby increasing carrier lifetimes. Evidence for this is provided by the long photo luminescence of up to 9 μs in $LiNbO_3$.[145]

- **Increase in the Space-Charge Width at the Interface of the Materials Surface.**

The increase in the photodecolourisation with the Cu^{2+} ions doping can also be possible due to the increase in the space-charge width at the interface of the materials surface to the secondary phase (e.g. liquid, gas, or metals) because the doped BFO has been known to generally have a significant improvement in the dielectric property.[119,168,173,174] It is well known that the contact between a semiconductor and another phase such liquid, gas, or metal will involves redistribution of electric charges and the formation of a double layer.[7] The width of the space-charge region is proportional to the Debye length,[175] L_D.

$$L_D = \left(\frac{\varepsilon_0 \varepsilon_r kT}{e^2 N_D}\right)^{1/2} \qquad \text{Equation 4.2}$$

Where ε_0 is the permittivity of free space, ε_r is the dielectric constant or permittivity value of the material, and N_D is the donor density. According to the equation above, it can be observed that an increase in the dielectric constant can increase the Debye length and, which also proportional to the increase in the width of the space-charge region. The increase in the space-charge width will in turn increase the number of carriers separation which prolonged the photogenerated carriers lifetime. Therefore, has the potential to increase the photocatalytic activity.

BFO multiferroic materials having ferroelectric and anti/ferromagnetic behaviour has gained an increasing interest for visible light activated photocatalytic processes[10] Study are being made to elucidate that ferroelectric materials can be highly photoactive with some exceptional properties due to the internal dipole of the material[15] Although the photocatalytic activity of the BFO powders under visible

light is mainly due to small energy band-gap, other factors such as their ferroelectric nature, weak ferromagnetic properties and dielectric property are still being investigated[97] and further enhanced the interest in such functional materials as photocatalysts.

It is, therefore, important to consider that the BFO is not only a semiconductor but also a multi-ferroic material that demonstrates electrons and holes separation due to the internal fields within the crystal lattice. In essence the internal electric field of the BFO exhibits a spontaneous polarisation that acts like an internal p-n junction. This band structure can be considered a '**self-junction'** as carriers are influenced by the field within, and inherent to, the material. This, largely, determines the band bending at the interface and the surface where the mobile carriers can accumulate. Hence, the enhanced internal polarization and increase in dielectric property of the ferroelectric material (BFO) due to doping is thought to be the reasons of the increased photodecolourisation rate of the RhB dye.

Figure 4.47 (a) and (b) show the high resolution of the Transmission Electron micrograph of 1at% Cu doped BFO. The electron micrograph showed the presence of darker spots within the BFO particles (figure 4.47 (a)), and the magnified image of darker spots showed the locations of the lattices distortion due to the foreign atom inclusion (doping).

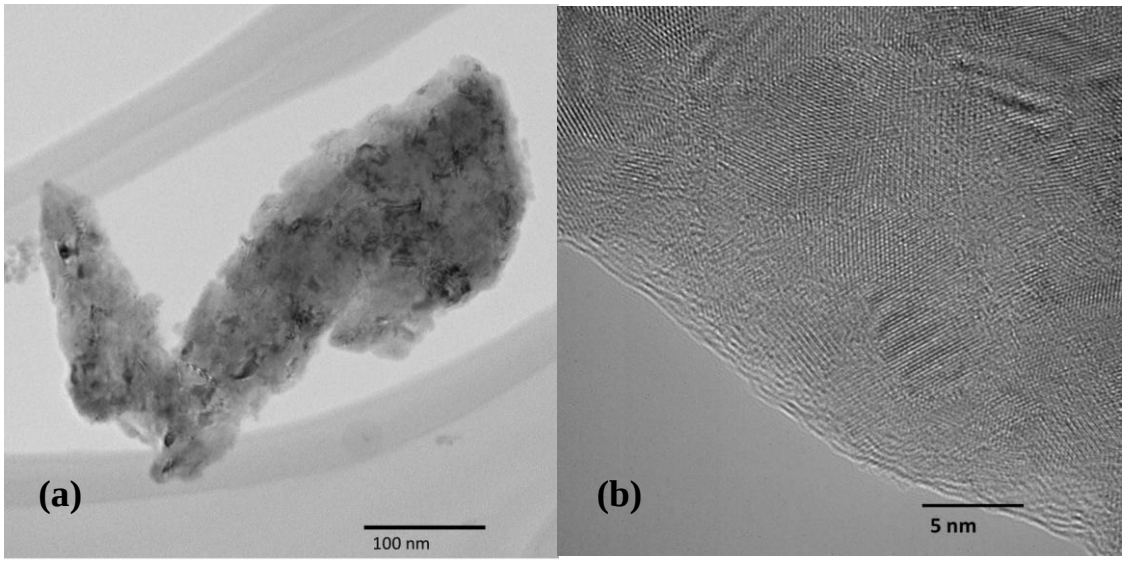

Figure 4.47 (a) Transmission electron micrograph of 1at% Cu doped BFO, (b) high resolution image showing lattice distortions

Figure 4.48 shows the high resolution of the Transmission Electron micrograph of 2at% Cu doped BFO. Similarly to 1at% Cu doped BFO, darker spots were observed within the BFO particles (figure 4.48 (a)), but with more frequency. Figure 4.48 (b) is the magnified TEM image of the 2at% Cu doped BFO and showed the locations of darker spots within the lattices indicating the distortion of the crystal lattice due to the foreign atom inclusion (doping).

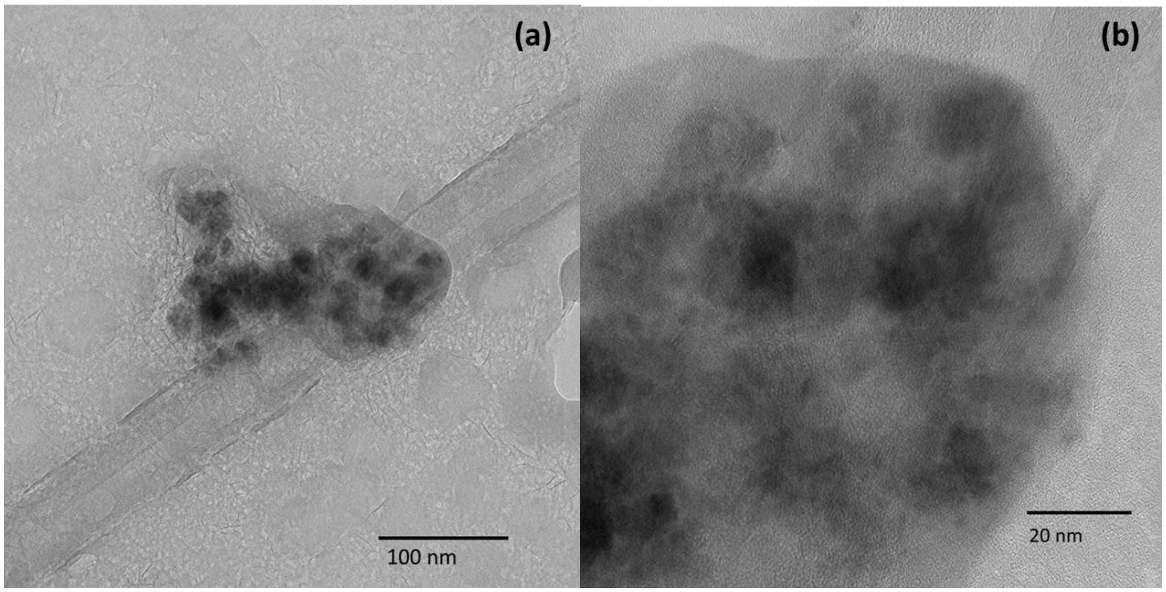

Figure 4.48 Transmission electron micrograph of 2 at% Cu doped BFO

4.3.2 Photodecolourisation of Tungsten (W) Doped BFO

A limited amount of data was collected in experiments, however, the measurements of the photodecolourisation of the Rhodamine B solutions over various atomic percentage tungsten (W) BFO doped powders were found to be repeatable. Tungsten (W) doped BFO was also synthesized by in-situ doping via an autocombustion method. Figure 4.49 shows the overall evolution of the XRD patterns of W doped BFO powder from 0.5at% to 2 at%. At 0.5at% doping concentration, the XRD patterns did not show significant changes to the original synthesized BFO powder, and as the doping concentration increased, the XRD patterns showed some deviations from original as synthesized BFO powder and the $Bi_2Fe_4O_9$ phase become more prominent, while maintaining the peaks from the original BFO powder. At 5at% W doping, the $Bi_2Fe_4O_9$ and Bi_2O_3 phases evolved together with the BFO phase. However, no Tungsten Oxide phase was present in all cases.

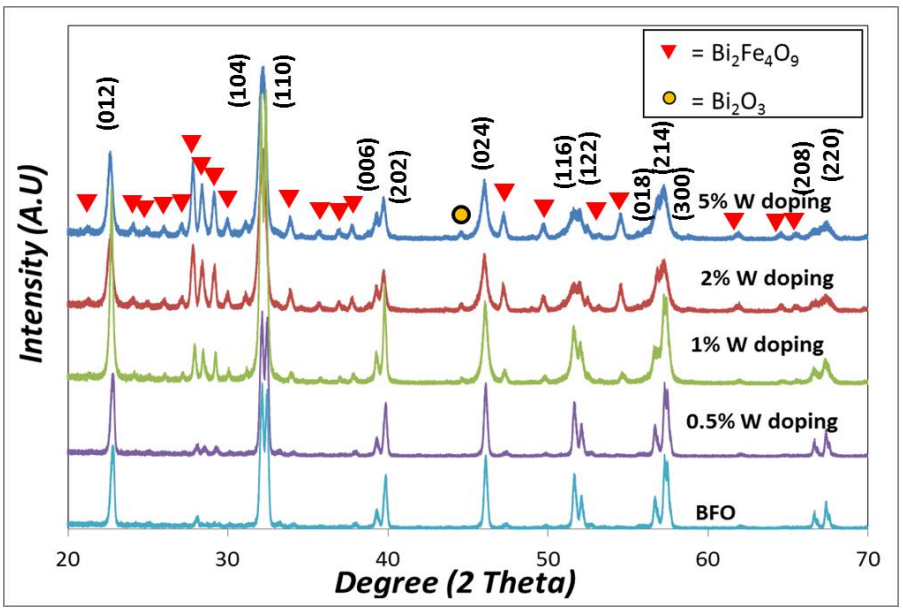

Figure 4.49 XRD patterns evolution of W doped BFO powder from 0.5at% to 5at%

Figure 4.50 shows the magnified XRD patterns of W-doped BFO at 2theta angle from 30 to 69 degree, presenting the BFO phase characteristic peaks corresponds to the crystallographic planes of (104), (110), (006), (202), (018), (214), (300), (208) and (220). The XRD patterns showed no changes up to 1at% Cu doping, and after that at 2at% and 5at% Cu doping one noticeable feature that the peak-splitting behaviour in the samples disappeared. From the magnified XRD patterns in the vicinity of 2Θ around 32 degrees (Figure 4.50(a)), the separated (104) and (110) diffraction peaks are still observed at until 1at% W doped BFO sample. However, as the W concentration increases to 2at% and 5at%, the two diffraction peaks almost merged into a single broad peak and also has a tendency to shift toward a slightly lower 2Θ value. At higher 2 theta angle (figure 4.50 (c) & (d)), the BFO peaks corresponds to the crystallographic planes of (018), (214), (300), (208) & (220) also showed slight right peak shift at 0.5at% W doping and slight left peaks shift at 1at%, 2at% and 5at% W doping. This result suggests that the BFO rhombohedral crystal structure is distorted by W substitution resulting in the change of the crystallography symmetry of the BFO, which also in agreement and also observed in other doped BFO ceramics work.[176,177,178] Other secondary phases of $Bi_2Fe_4O_9$ and Bi_2O_3 are also evolved due to the substitution of the Fe atom by W.

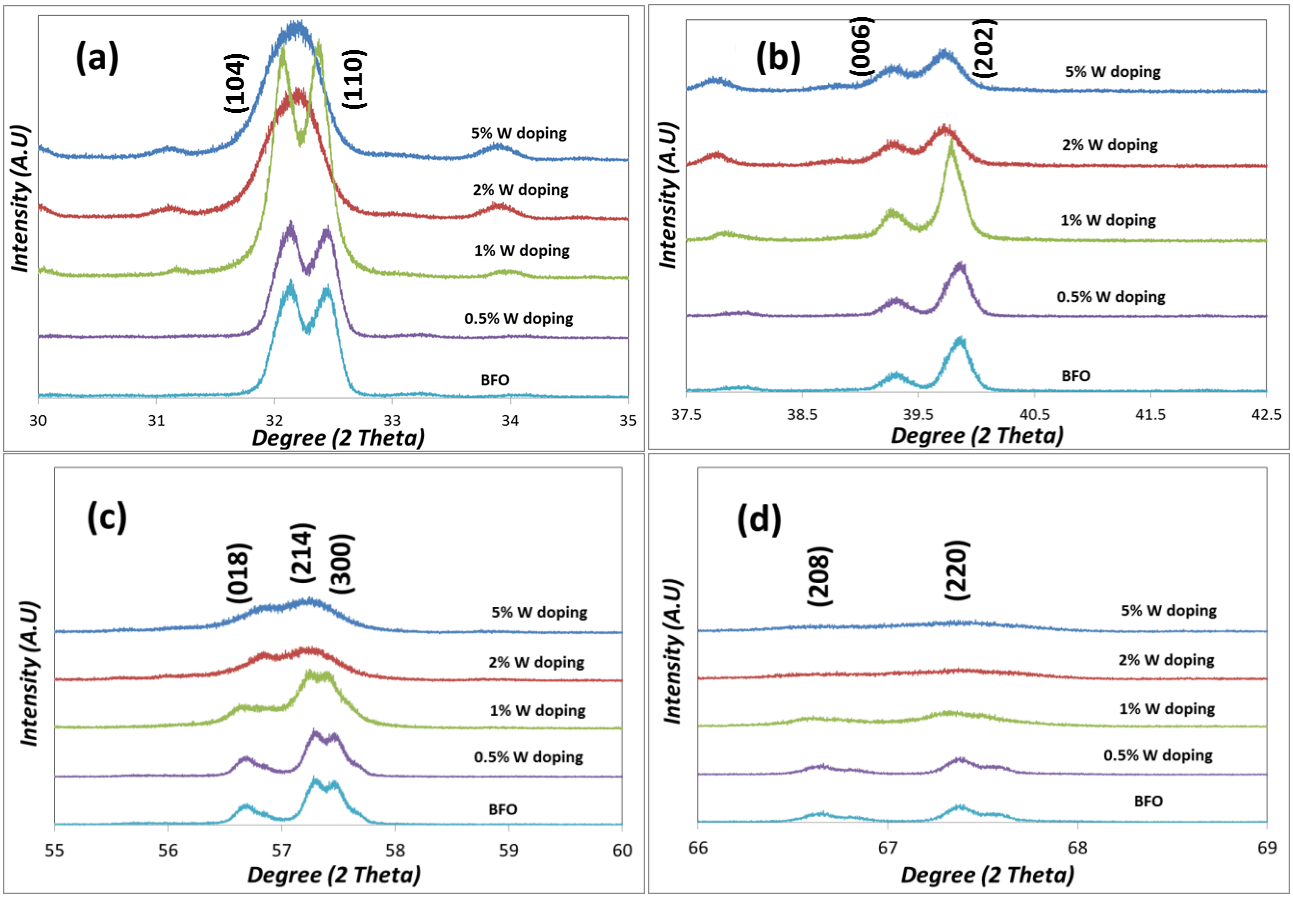

Figure 4.50 XRD patterns evolution of W doped BFO powder from 0.5at% to 5at%, zoom in of (a) (104) and (110) peaks, (b) (006) and (202) peaks, (c) (018), (214) and (300) peaks, (d) (208) and (220) peaks

Figure 4.51 shows the photodecolourisation profile of the W doped BFO powder to the RhB dye solution at a normal pH (pH=6.7) environment. As the doping concentration increased, the photodecolourisation rate increased. At 0.5at% W doping photodecolourisation rate has increased to about 50% dye decolourisation under a 6 hour time frame, a significant improvement compared to the pure BFO. The photodecolourisation rate of the RhB dye for 1at%, 2at% and 5at% W doped BFO after a 6 hour time frame showed a similar decolourisation rate at more than 90% (92% and 98% respectively).

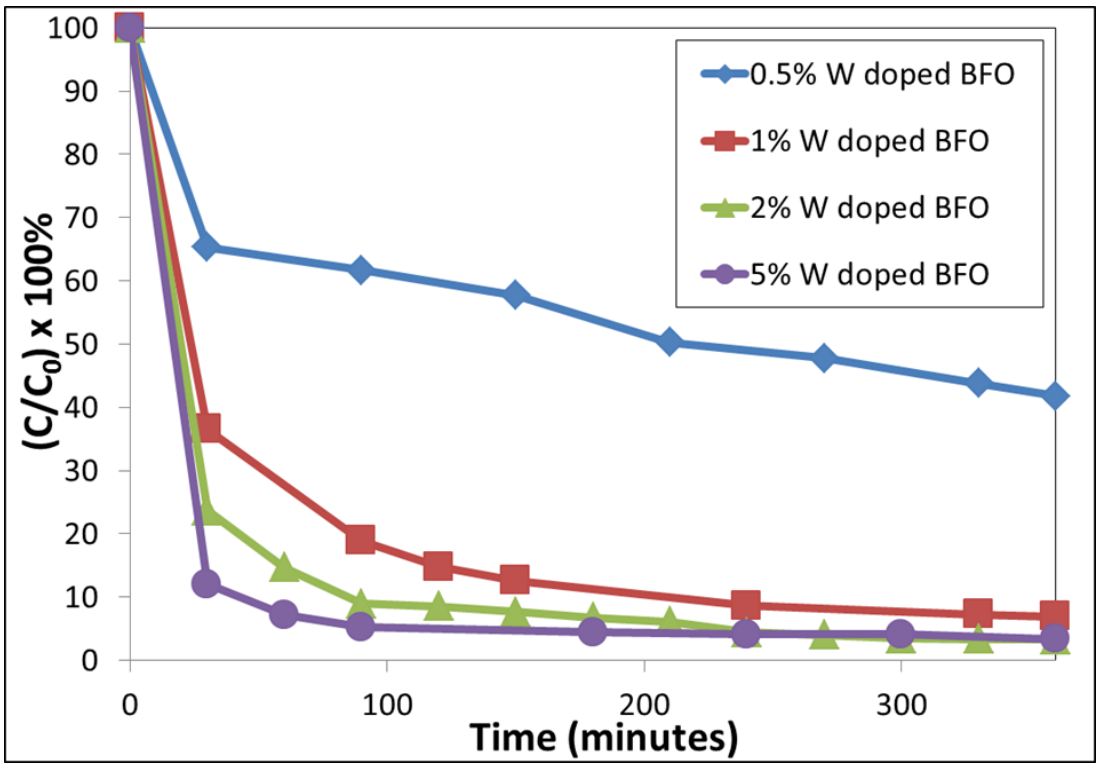

Figure 4.51 Photodecolourisation profiles for the RhB dye with W doped (0.5at% - 5at%) $BiFeO_3$ under a simulated visible light (AM1.5) illumination.

4.4 Heterojunction of the BFO/TiO_2

As the BFO is non-photostable due to its band structure, an effort has been made to protect the BFO surface from photocorrosion during photodecolourisation work. Preliminary work has been carried out on the coating of the TiO_2 onto the BFO nanopowders using Titanium Tetra Iso Propoxide (TTIP) as a precursor for the TiO_2 coated onto the BFO nanopowders with various molar ratio of $BiFeO_3$ to TiO_2 of 1:1, 1:2 and 2:1.

XRD scan was performed onto the three different TiO_2 coated BFO molar ratio as shown in figure 4.52. The X-ray diffraction patterns did not show differences between the three molar ratio specimens. It could be due to the thin layer of the TiO_2 on the BFO particle surface, and again the lack of change in the crystallography is due to the X-ray diffraction technique produces data averaged over the full penetration of the x-rays used and is not surface sensitive.

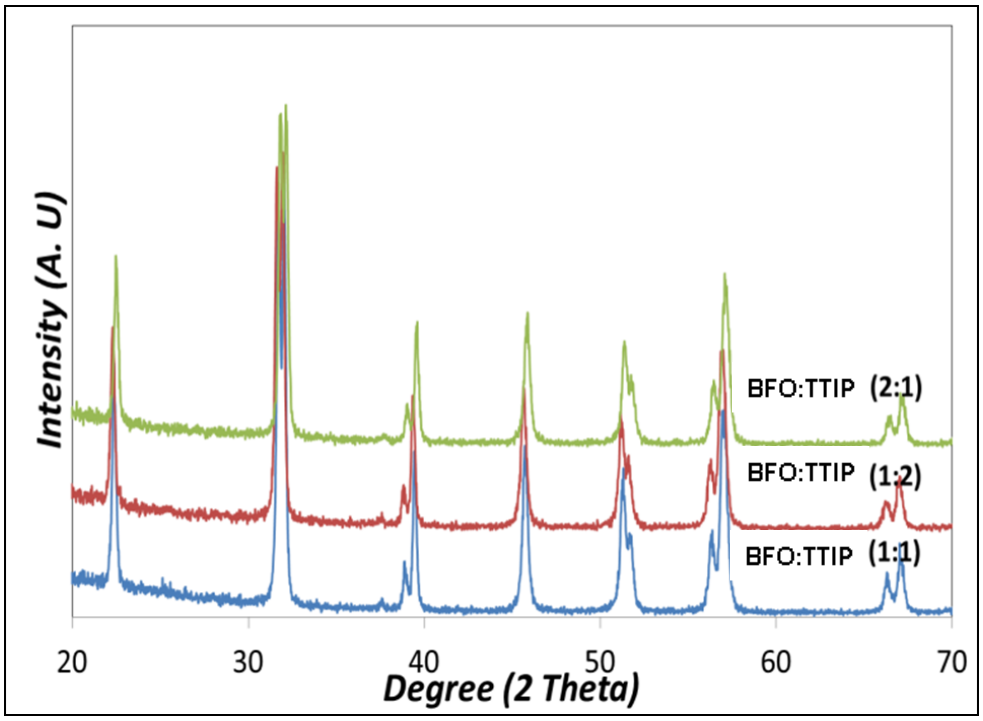

Figure 4.52 XRD patterns of the TiO_2 coated BFO with various molar ratio of BFO: TTIP.

An XPS scan was performed on the three specimens of the various molar ratios between the BFO and the TTIP and the XPS technique is able to detect the presence of the TiO_2 of the three specimens as shown in figure 4.53. XPS is a surface sensitive technique, the photoelectron signal is able to detect from the first 1-10 layers of atoms and molecules. The XPS spectrum shows a different

intensity/concentration of the TiO_2 for the three different specimens and showed the small concentration amount of the Ti element.

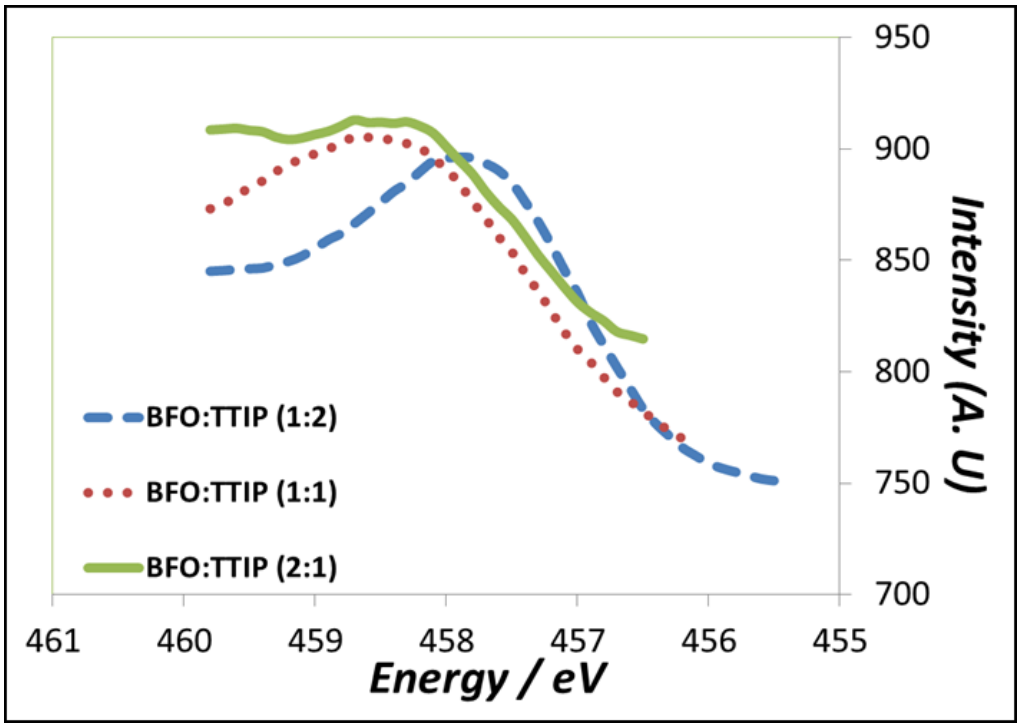

Figure 4.53 XPS spectrum showing the differences of the Ti peaks between the three different molar ratios of BFO: TTIP.

As shown in figure 4.54, photodecolourisation experiment was also conducted on the TiO_2 coated BFO powder with various BFO: TTIP molar ratio. It is found that the RhB dye solution was able to be decolourised and reach > 95% decolourisation of the RhB dye at around 270 minutes for the BFO: TTIP of 1:1 molar ratio. With lesser TTIP ratio (BFO:TTIP of 2:1 ratio), the photodecolourisation rate of the RhB dye reduced, reaching around 90% decolourisation in a 6 hour time frame. For a larger TTIP ratio (BFO: TTIP of 1:2 ratio), the decolourisation rate increased reaching around 90% within 150 minutes. However, in all cases the photodecolourisation rate is still lower than the nano-TiO_2 (P25 Degussa) photodecolourisation rate (Figure 4.54 inset).

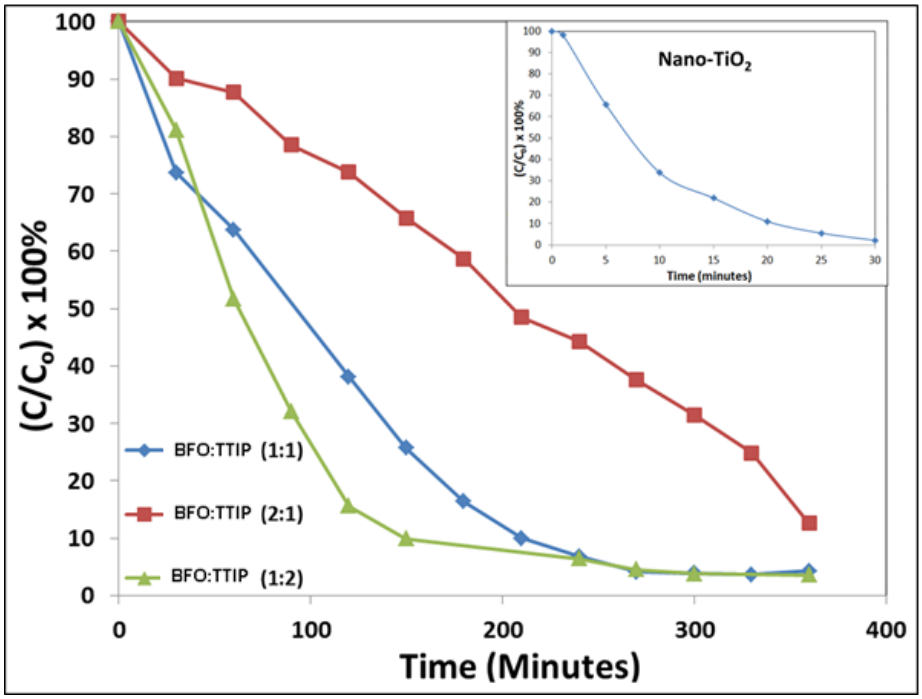

Figure 4.54 Photodecolourisation of the RhB dye (10ppm) pH 6.7 with the TiO_2 coated BFO powder (Various molar ratio of BFO: TTIP) – with a solar simulator air mass 1.5

Figure 4.55 shows a high resolution transmission micrograph of the TiO_2 coated BFO powder with the BFO: TTIP molar ratio of 2:1. In the high magnification image (Figure 4.55(b)), it was observed that there is a thin layer of the TiO_2 film coated on the BFO particle with a thickness of around ~ 1 nm.

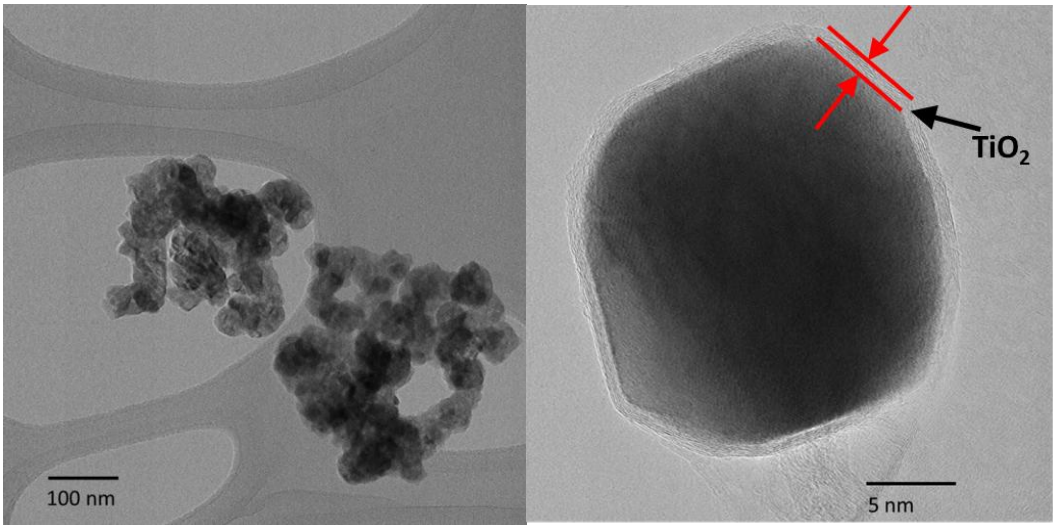

Figure 4.55 Transmission electron micrograph of the TiO_2 coated BFO (hetero-junction) with the BFO: TTIP molar ratio 2:1.

Figure 4.56 shows a high resolution transmission micrograph of the TiO_2 coated BFO powder with the BFO: TTIP molar ratio of 1:2. In the high magnification image (Figure 4.56(b)), it was observed that the thin layer of the TiO_2 film coated on the BFO particle with a thickness of around ~ 3 nm. With a higher molar concentration of the TTIP during a coating reaction will yield a thicker TiO_2 coating on the BFO particle.

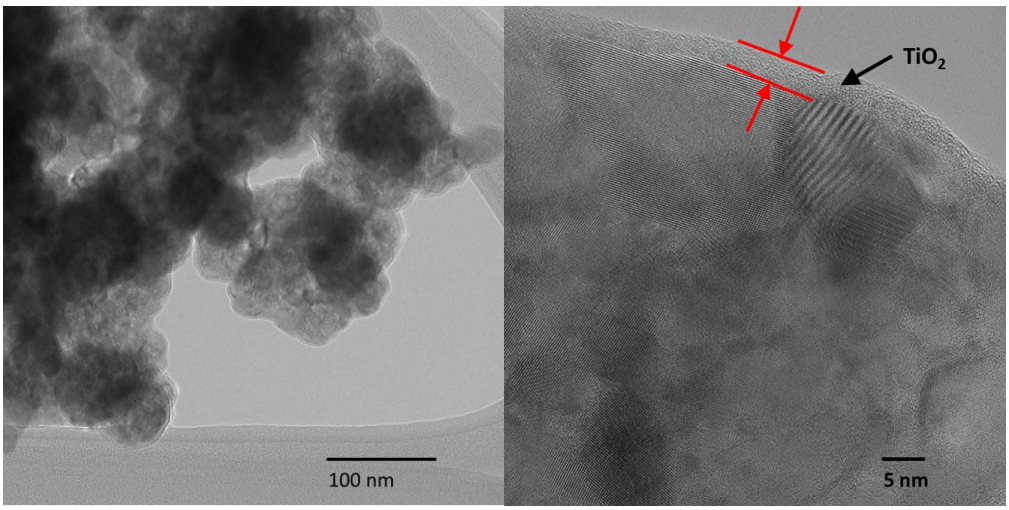

Figure 4.56 Transmission electron micrograph of the TiO2 coated BFO (hetero-junction) with the BFO: TTIP molar ratio 1:2.

From the high resolution TEM micrograph, the TiO_2 seemed to have an amorphous structure as the TiO2 coating did not show ordered atoms orientation of crystalline structure. This explained the reason why the photodecolourisation rate of the RhB dye by the TiO_2 coated BFO samples in this work is still lower than the rate of nano-TiO_2. Amorphous TiO_2 has larger band gap than crystalline anatase phase TiO_2 (larger than 3.4 eV) and has lower photocatalytic rate of dye degradation as reported by Restrepo et al.[179] However, the objective to protect the BFO from photocorrosion is achieved as shown by steady photodecolourisation profile of RhB dye by the TiO_2 coated BFO.

Despite its potential of visible light activation photocatalyst for the degradation of organic pollutants due to its small bandgap value (~2.2 eV), the BFO band structure has the limitations and prone photocorrosion that results in low photocatalytic activity of the BFO which hinders its commercialization as photocatalytic agent for photocatalytic oxidation technology.[10,180] Hence, effort is being made to stabilise the BFO by coating it with a thin film of stable photocatalyst materials to create heterojunctions. Recently, Luo et al [150] reported that the $SrTiO_3$-coated BFO core/shell nanostructures show it can produce H_2 under visible-light irradiation, a promising way to stabilise BFO.

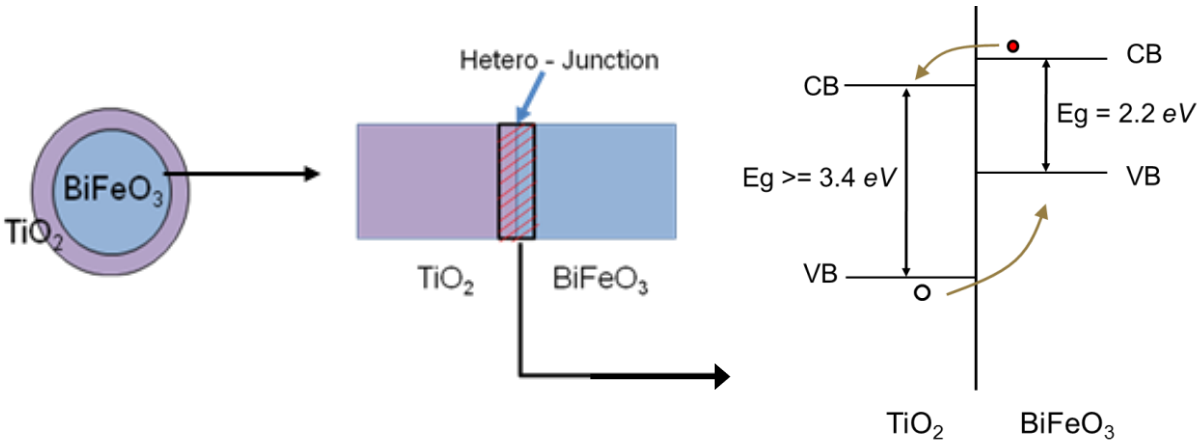

Figure 4.57 Schematic diagram of the heterojunction energy bandgap of the TiO_2 coated $BiFeO_3$

For TiO_2 coated BFO, the heterojunctions will be created when the $BiFeO_3$ and the TiO_2 are in contact. This will improve the photogenerated charge carriers lifetime by enhancing the charge separation as illustrated by the heterojunctions band structure shown in figure 4.57. The photogenerated electrons by the BFO will be injected into the TiO_2 conduction band due to its lower energy level, while the photogenerated holes by the TiO_2 will be transferred to the valence band of the

BFO, hence the photogenerated carriers lifetime were prolonged due to the carriers separation and preventing early recombinations. Thus, this improved the efficiency of the photocatalytic activity by enhancing the photo redox reactions.

The separation of photogenerated electrons and holes induced redox reactions according to the relative potentials of the conduction and valence bands of the two types of the semiconductor and the redox potentials of the redox couples present at the interface. In addition, the coating of the TiO_2 on the BFO surface will provide protection to the BFO reagents against photocorrosion with a liable reactant species such as the RhB dye, as discussed in chapter 4.2. The TiO_2 thin layer coating will prevent direct contact between the RhB dye molecules and the BFO surface which will cause holes injection from the RhB HUMO level to the BFO valence band, the pathway for photocorrosion.

5 CONCLUSION

The aim of this thesis was, through the investigation of a low band gap multiferroic Bismuth Ferrite ($BiFeO_3$), to develop and contribute to the detailed understanding of the $BiFeO_3$ particulate nanostructures as visible light activated photocatalysis with consideration of its ferroelectric nature, against various organic azo dyes. The hypothesis made is that the internal polarization field of the ferroelectric powder could reduce the charge carrier's recombination rate which may translate to increase in the photocatalytic activity. It was also postulated that the amount of reactants adsorbed in the double layer at the ferroelectric surface may be influenced by the surface charge. The band position of the ferroelectric materials against the organic dyes HOMO-LUMO is playing a crucial part in the photostability of the BFO.

The first stage was to obtain best set of synthesis parameters for the $BiFeO_3$ nanopowders and its characterization to ascertain the optical band gap, size and morphology and the magnetic property. It is found that the best annealing of the BFO is at 650˚C for 3 hours and the obtained BFO nanopowders was a highly crystalline phase in the nanoscale and with an optical band gap of 2.2 eV. The photocatalytic performance of the synthesized BFO nanopowders on cationic and anionic organic dyes (Rhodamine B and Acid Black dye respectively) was investigated utilizing a solar simulator illumination spectrum. An effort was also done to understand the effect of the ferroelectric surface charge upon the dye adsorption by monitoring change in the concentration of the ionic dye molecules in an aqueous solution after the BFO powders were added. The synthesized BFO

nanopowders has an overall net positive surface charge (overall net C+ polarization) as evidenced by the negative zeta potential (-16 mV). This is supported by the adsorption-desorption experiment where cationic dye (RhB dye) adsorption on the BFO surface is negligible, while anionic dye (AB dye) adsorption is significant. At the isoelectric point of the BFO at pH 2, the RhB dye adsorption is significantly increased due to the diminished electric double layer on the BFO particle surface and improves the photochemical reaction of the RhB dye degradation through direct photo redox reaction. It was shown that the BFO is able to photodecolourise the RhB dye under visible light simulated by a solar simulator with AM=1.5, and work best under a pH 2 environment where negative charge co-ions screening on the BFO particle surface is minimum (iso-electric point).

However, it was found that the BFO is not photostable with respect to the RhB dye as evidenced by two visible trends in the photochemical decolourisation rate of the RhB dye. There is a trend of photodecolourisation rate slowdown in all pH values. The slowdown of decolourisation rate of the RhB dye was caused by the photocorrosion of the BFO, and this is the limiting feature for the decolourisation of the dye. This could be explained by the band position of the BFO against the RhB dye HOMO-LUMO position where the valence band of the BFO lies above the HOMO level of the RhB dye, hence the band structures show that while it is not possible for the BFO to inject holes into the RhB dye, the RhB dyes are able to inject holes into the BFO, hence the BFO photocorroded. This instability is characteristic of the semiconductor that is liable to photocorrosion. Surface chemical analysis via the X-Ray Photoelectron Spectroscopy (XPS) on the BFO powder after the photochemical decolourisation experiment indicated that the BFO

photocorrodes through the dissolution of the Fe from the Fe-O bond in the solid solution, while the Bi_2O_3 component remaining largely unchanged. It is proven with an experiment by replacing the BFO at regular intervals to mitigate the photocorrosion problem of the BFO and it is shown that the photo-decolourisation of the dye proceeds at a rate exceeding Titania, hence is indeed a promising material for visible-light driven photochemistry.

The second stage was to study the effect of doping to the BFO powder to enhance its photocatalytic activity against organic dyes. Copper (Cu) and Tungsten (W) metal doped BFO have been successfully synthesized via an in-situ doping process using an autocombustion technique. The X-Ray diffraction study indicates that the Cu and W dopants were well incorporated into the rhombohedral lattice structure of the BFO with an increased interplanar spacing due to the lattice distortion as shown in the left shift of the XRD peaks. However, as the doping concentration increased, the secondary phases of the $Bi_2Fe_4O_9$ and the Bi_2O_3 became more prominent, but no Copper Oxide and Tungsten oxide phases were present in all cases. The photochemical decolourisation experiment of the Cu doped BFO powder against the RhB dye at a normal pH environment (pH 6.7) showed that as the doping concentration increased, the photodecolourisation rate increased. This increased in the photochemical decolourisation of the RhB dye by the doped BFO powder could be attributed to several reasons; firstly, it was found that as the doping concentration increased from 0.5at% to 5at%, the calculated optical band gap using Tauc's plot decreased from 2.22 eV band gap for pure BFO to 2.08 eV for 5at% Cu doped BFO and might contribute to the increase in the photocatalytic property. Secondly, it could be due to the enhanced photogenerated carriers'

lifetime by carriers' separation because of the enhanced internal polarization and the dielectric property of the BFO when the Cu^{2+} ions replaced the Fe^{3+} ions in the BFO lattice. The enhancement in the internal polarization is due to the formation of a defect dipole between the oxygen vacancy and the Cu ions that sit on the Fe lattice. An increase in the internal polarization will lead to the increase of separation of the photogenerated carriers' thereby increasing the carriers' lifetime, hence improved photocatalytic performance. Improvement in the dielectric constant could also lead to an increase in the space charge region that will enhance the carrier's separation, thus the enhanced the carrier's lifetime that could potentially increase the photocatalytic property performance.

In the third stage, a study was made with the aim to protect the non-photostable BFO from the surface photocorrosion by coating a thin layer of the TiO_2 onto the BFO surface to create a heterojunction structure. It is found that with the TiO_2 coating on the BFO particle surface, the photocorrosion disappeared and was able to photodecolourise the RhB dye completely, however at a rate slower than Titania (P25 degussa). The improvement of the photostability and photocatalytic performance of the TiO_2 coated BFO is attributed to the enhanced photogenerated carriers lifetime due to the heterojunctions band structure between the TiO_2 and the BFO that allows the photogenerated electrons at the BFO conduction band to be transferred to the TiO_2 conduction band and the photogenerated holes to be transferred from the TiO_2 valence band to the BFO valence band, thus preventing early the carriers recombination.

In summary, the study in this project has demonstrated the photochemical decolourisation performance of a low band gap BFO against organic dyes and its detailed study relating the photochemical decolourisation performance of the BFO to the ferroelectric nature of the BFO, as well as the detailed photocorrosion study of the BFO with respect to the BFO - organic dye band structures. Detailed study on the improvement of the photochemical decolourisation performance of the BFO by the doping and surface coating has also been carried out and shown to have an improved photocatalytic performance.

6 FUTURE WORK

BFO has shown to be promising visible light activated photocatalyst exceeding the rate of photodecolourisation of nano-TiO_2 in the experiment where BFO nanopowders were replaced at 1 minute interval to mitigate photocorrosion effect. However, it is still insufficient for practical use as photochemical reagent. In this thesis, the BFO nanopowders and the doped BFO powders have been proven able to perform photochemical decolourisation of azo dyes under solar simulator illumination (AM =1.5), but still lower than the rate of nano-TiO_2.Hence, there are several highlighted areas for future investigations. These include:

- The investigation of the plasmonic nanostructures on the BFO particle surface (metallic nanostructures on the BFO surface, e.g. Silver) effect on the photochemical reaction rates (Plasmonic). The silver nanostructures will be deposited onto the BFO particle surface using a low intensity UV light and will be deposited onto the C+ face. The photochemical activities of this plasmonic BFO powders could be compared at different silver deposition amount on the BFO surface to determine the optimal loading of the silver deposits.

- The polarisations effect upon photocatalytic activity. The BFO could be made into a thin film and polarised to have a C+, C- or poly domain structure and used to decolourise dye solutions under a simulated solar irradiation. With these polarised BFO thin film samples under the three polarised surface conditions, the adsorption studies of different types of ionic dyes in aqueous solution could be carried out to understand more clearly the effect of the polarisation on the photodecolourisation reaction rate.

- The study of doped BFO in thin film samples. When a doped BFO is made into thin film samples, the surface polarisation state, electronic and the dielectric property are easier to be quantified compared to doped BFO in powder form. This will provide a better understanding of the improved photochemical decolourisation of the doped BFO powder against organic dyes. The doped BFO thin film could also be polarised and a study of the polarisation effect of the doped BFO thin film in the photochemical decolourisation of the organic dyes.
- Measurement of TOC (Total Organic Carbon) content to quantify the amount of organic dye degradation from the photochemical decolourisation experiment. The dye solutions before and after the photodecolourisation experiment will be fed into the TOC analyser to determine the exact amount of organic content degradation. The TOC content is a widely used indicator for organic pollutants in water.

The proposed further studies experimental works above could be performed using the experimental setups used to collect the data in this thesis, with the additional instrumentations such as the TOC analyser for the TOC measurement, Probe Microscopy and the Cyclic Voltammetry instrument for polarisation related studies. These studies were not carried out in this work due restraints on the time available to perform experimental work and also the experiments being outside the scope of this thesis which aimed to specifically study the properties of a low band gap multiferroic BFO powders for degradation of organic compounds by visible light activation.

7 REFERENCES

[1] West, Larry (March 26, 2006). "World Water Day: A Billion People Worldwide Lack Safe Drinking Water".

[2] M. Mohajerani, M. Mehrvar & F. Ein-Mozaffari, "An Overview of The Integration of Advanced Oxidation Technologies and Other Processes for Water and Wastewater Treatment" International Journal of Engineering, Vol 3, Issue 2, pp. 120-146

[3] *R. Vinu AND Giridhar Madras, "*Environmental remediation by Photocatalysis" Journal of the Indian Institute of Science, Vol 90, Issue 2, 2010

[4] A. Fujishima and K. Honda, Nature 37, 238 (1972)

[5] Frank SN, Bard AJ (1977) J Phys Chem 81:1484–1488.

[6] Pruden AL, Ollis DF (1983) J Catal 82:404–417.

[7] Amy L. Linsebigler, Guangquan Lu, and John T. Yates, Jr, *Chem. Rev.* 1995, *95*, 735-758

[8] George S, Pokhrel S, A. E. Nel; J. Am. Chem. Soc. 2011, 133, 11270–11278

[9] Phillip Christopher, Hongliang Xin, Suljo Linic, "Visible-light-enhanced catalytic oxidation reactions on plasmonic silver nanostructures", *Nature Chemistry* 3, 467-472 (2011)

[10] F. Gao, X. Y. Chen, K. B. Yin, S. Dong, Z. F. Ren, F. Yuan, T. Yu, Z. G. Zou, and J. M. Liu, Adv. Mater. **19**, 2889-92 (2007)

[11] Nozik, A.J. and R.J. Memming, Phys. Chem., 1996. 100(31): p. 13061–13078

[12] J. L. Giocondi, G. S. Rohrer, **2001**, *J Phys Chem B, 105*, 8275.

[13] J. L. Giocondi, G. S. Rohrer, **2001**, *Chemistry of Materials, 13*, 241.

[14] S. Dunn, D. Cullen, E. Abad-Garcia, C. Bertoni, R. Carter, D. Howorth, R. W. Whatmore, **2004**, *Appl. Phys. Lett., 85*, 3537.

[15] S. Dunn, P. M. Jones and D. E. Gallardo, J. Am Chem Soc, 129 (28), 8724 – 8728 (2007).

[16] P. M. Jones, S. Dunn, **2009**, *J. Phys. D, 42*.

[17] S. Dunn, D. Tiwari, **2008**, *Appl. Phys. Lett., 93*.

[18] Goldschmidt, V. M., "Geochemische verteilungsgesetze der elemente". *I Mater Naturvid KI no 2 Oslo: Skrifter Norske Videskaps-Akad 1926.*

[19] Jaffe, B, Cook, W. R, Jr. and Jaffe H., "Piezoelectric Ceramics" *Academic Press London and New York, 1971*

[20] J. Curie and P. Curie, C. R. Acad Sci. Paris **91**, 294, (1880); **91**, 383 (1880).

[21] P. Langevin, French Patent No. 505 (17 September 1918), p. 703.

[22] L. E. Cross, "Ferroic Materials and Composites: Pass, Press, and Future" (1997)

[23] Lines, M.E. and A.M. Glass, *Principles and Applications of Ferroelectrics and Related Materials* 1977, Oxford: Clarendon Press.

[24] Forsbergh, P.W., Phys. Rev., 1949. **75**.

[25] W.D. Callister, J., *Materials Science and Engineering: An Introduction*. 2000, New York: John Wiley and Sons, Inc.

[26] J. F. Scott, Ed, *Ferroelectric memories*, Springer **2000**.

[27] W. Cochran, Advan. Phys. **9**, 387 (1960); **10**, 401 (1961)

[28] P. W. Anderson, Fizika dielektrikov (Akad. Nauk, SSSR, Moscow, 1959)

[29] Eng LM (1999) *Nanotechnology* 10:405

[30] Emelyanov AY, Pertsev NA, Salje EKH (2001) J Appl Phys 89:1355

[31] D. Tiwari and S. Dunn, J. of Mats Sci, 44 (19) 5063-5079 (2009)

[32] Introduction to Solid State Physics, C. Kittel, (1976)

[33] S.O. Kasap, Principles of Electronic Materials and Devices, McGraw-Hill, 2nd edition (2002)

[34] Hans Schmid, "Multi-Ferroic Magnetoelectrics", Ferroelectrics 162, 665 (1994)

[35] Curie, P. "Sur la symétrie dans les phénomènes physiques, symétrie d'un champ électrique et d'un champ magnétique" *J. Physique* 1894, 3, 393

[36] Dzyaloshinskii, I. E. "On the magnetoelectrical Effect in Antiferromagnets" Zh. Eksp and Teor. Fiz. 1959, 37, 881

[37] Astrov, D. N., "The Magnetoelectric Effect in Antiferromagnetics". *Zh. Eksp. Teor. Fiz.* 1960, 38, 984

[38] Ascher, E.; Rieder, H.; Schmid, H.; Stossel, H.; "Some Properties of Ferromagnetoelectric Nickel-Iodine Boracite, $Ni_3B_7O_{13}I$". *J. Appl. Phys*. 1966, 37, 1404

[39] J. Ryu, A. Vázquez Carazo, K. Uchino, and H. E. Kim, J. Electroceramics **7**, 17 (2001)

[40] R. P. Mahajan, K. K. Patankar, M. B. Kothale, S. C. Chaudhari, V. L. Mathe, and S. A. Patil, Pramana J. Phys. **58**, 1115 (2002).

[41] J. Ryu, A. Vázquez Carazo, K. Uchino, and H. E. Kim, Jpn. J. Appl. Phys. **40,** 4849 (2001).

[42] Christian Michel, Jean-Michel Moreau, Gary D. Achenbach, Robert Gerson, and W. J. James, Solit State Communications **7**, 701 (1969)

[43] Moreau, J. M.; Michel, C.; Gerson, R.; James, W. J., "Ferroelectric $BiFeO_3$ X-ray and Neutron Diffraction Study". *J. Phys. Chem. Solid*. **1971**, 32, 1315.

[44] W. Eerenstein, F. D. Morrison, M. Blamire, J. F. Scott, and N. Mathur, Science 307, 1203a (2005).

[45] Bucci, J. D.; Robertson, B. K.; James, W.J., "The Precision Determination of the Lattice Parameters and the Coefficients of Thermal Expansion of $BiFeO_3$". *J. Appl. Cryst.* **1972**, 5, 187.

[46] Kubel, F.; Schmid, H., "Structure of a Ferroelectric and Ferroelastic Monodomain Crystal of the Perovskite $BiFeO_3$'. *Acta Cryst. B* **1990**, 46, 698

[47] Chu, Y.H.; martin, L.W.; Holcomb, M. B.; Ramesh, R., "Controlling Magnetism with Multiferroics". *Mater. Today* 2007, 10, 16

[48] Michel, C; Moreau, J. M.; Achenbach, G. D.; Gerson, R.; James, W.J., "The Atomic Structure of $BiFeO_3$". *Solid State Comm.* **1969**, 7, 701.

[49] Sosnowska, I.; Przenioslo, R.; Fisciier, P.; Murashov, V. A., "Investigation of Crystal and Magnetic Structure of $BiFeO_3$ Using Neutron Diffraction". *Acta Phys. Polonica A* **1994**, 86, 629.

[50] James, R. T.; Gerson, R.; James, W. J., "Dielectric Hysteresis in Single Crystal $BiFeO_3$". *Solid State Comm.* **1970**, 8, 1073.

[51] Wang, J.; Neaton, J. B; Zheng, H.; Nagarajan, V.; Ogale, S. B.; liu, B.; Viehlan, D.; Vaithtanathan, V.; Schlom, D. G.; Wahmare, U. V.; Spadin, N. A.; Rabe, K. M.; Wuttig, M.; Ramesh, R., "Epitaxial $BiFeO_3$ Multiferroic Thin Film Heterostructures". *Science* **2003**, 299, 1719

[52] Lebeugle, D.; Colson, D.; Forget, A.; Viret, M., "Very Large Spontaneous Electric Polarization in BiFeO3 Single Crystals at Room Temperature and Its Evolution under Cycling Fields". *Appl. Phys. Lett.* **2007**, 91, 022907.

[53] Shvartsman, V. V.; Kleeman, W.; Haumont, R.; Kreisel, J., "Large Bulk Polarization and Regular Domain Structure in Ceramic $BiFeO_3$". *Appl. Phys. Lett.* **2007**, 90, 172115.

[54] S. V. Kiselev, R. P. Ozerov and G. S. Zhdanov, Sov. Phys. Dokl, Vol. **7**, 742(1963)

[55] Sonowska I, Peterlin–Neumaier T, Steichele E, "Spiral Magnetic Ordering in Bismuth Ferrite", *J. Phys. C* 1982, 15, 4835.

[56] Benjamin Ruette, S. Zvyagin, A. P. Pyatakov, A. Bush, J. F. Li, V. I. Belotelov, A. K. Zvezdin and D. Viehland, Phys. Rev. B **69**, 064114 (2004)

[57] Yu.F. Popov, A.M. Kadomtseva, A.K. Zvezdin, et al., in Magnetoelectronic Phenomena in Crystals, Edited by Manfred Fiebig, Kluwer Academic, Boston, (2004)

[58] Rovillain, P.; Cazayous, M.; Sacutto, A.; Lebeugle, D.; Colson, D., "Piezoelectric Measurements on $BiFeO_3$ Single Crystal by Raman Scattering". *J. Magn. Mater.* **2009**, 321, 1699.

[59] Rakov, D. N; Murashov, V. A.; Bush, A. A.; Venevtsev, Y. N., "Growth and Pyroelectric Properties of BiFeO3 Single-Crystals". *Sov, Phys. Crystallogr.* **1988,** 32, 262.

[60] Selbach, S.M.; Tybell, T.; Einarsrud, M. A.; Grande, T., "The Ferroic Phase Transitions of $BiFeO_3$". Adv. Mater. 2008, 20, 3692.

[61] Hill N. A, "Why There Are so few Magnetic Ferroelectrics?" *J. Phys. Chem. B* 2000, 104, 6694.

[62] Kumar M M, Srinivas A, Suryanarayana S V, Kumar G S, Bhimasankaram T, "An Experimental Set Up for Dynamic Measurement of Magnetoelectric Effect', *Bull. Mater. Sci.* 1998, 21, 251.

[63] Smolenskii, G. A.; Chupis, I. E., "Thermodynamic Theory of Crystals Possessing Ferroelectric and Ferromagnetic Properties". *Sov. Physics. – Solid Sate* **1962**, 4, 807.

[64] Smolenskii, G. A.; Chupis, I. E., "Ferroelectromagnets". *Sov. Phys. Usp*. **1982**, 25, 475.

[65] Lobo, R. P. S. M.; Moreira, R. L.; Lebeugle, D.; Colson, D., "Infrared Phonon Dynamics of a Multiferroic BiFeO3 Single Crystal". *Phys. Rev. B* **2007**, 76, 172105.

[66] Cazayous, M,; Malka, D.; Lebeugle, D.; Colson, D., "Electric field Effect on BiFeO3 Single Crystal Investigated by Raman Spectroscopy". *Appl. Phys. Lett.* **2007**, 91, 071910.

[67] Choi, T.; Lee, S.; Choi, Y. J.; Kiryukhin, V.; Cheong S. W., "Switchable Ferroelectric Diode and Photovoltaic Effect in BiFeO3". *Science* **2009**, 324, 63.

[68] Kundys, B.; Viret, M.; Colson, D.; Kundys, D. O., "Light-Induced Size changes in BiFeO3 Crystals". *Nature Mater*. **2010**, 9, 803.

[69] Baek, S. H.; Jang, H. W.; Folkman, C. M.; Li, Y. L.; Winchester, B.; Zhang, J. X.; He, Q.; Chu, Y. H.; Nelson, C. T.; Rzchowski, M. S.; Pan, X. Q.; Ramesh, R.; Chen, L. Q.; Eom, C. B.; "Ferroelastic Switching for Nanoscale Nonvolatile Magnetoelectric Devices.' *Nature Mater*. **2010**, 9, 309.

[70] Eerenstein, W.; Mathur, N. D.; Scott, J. F., "Multiferroic and Magnetoelectric Materials". *Nature* **2006**, 442, 759.

[71] Szafraniak et al, Journal of the European Ceramic Society 27 (2007) 4399–4402

[72] Wang Y P, Zhou L, Zhang M F, Chen X Y, Liu J M, Liu Z G, "Room-Temperature Saturated Ferroelectric Polarization in $BiFeO_3$ Ceramics Synthesized by Rapid Liquid Phase Sintering" *Appl. Phys. Lett.* 2004, 84, 1731.

[73] Achenbach G D, James W J, Gerson R, "Preparation of Single-Phase Polycrystalline $BiFeO_3$". *J. Am. Ceram. Soc.* 1967, 50, 437.

[74] Singh S K, Ishiwara H, Maruyama K, "Enhanced Polarization and Reduced Leakage Current in $BiFeO_3$ Thin Films Fabricated by Chemical Solution Deposition", *J. Appl. Phys.* 2006, 100, 064102.

[75] Selbach S M, Einarsrud M A, Grande T, "On the Thermodynamic Stability of $BiFeO_3$" *Chem. Mater.* 2009, 21, 169.

[76] E. J. Speranskaya, V. M. Skorikov, E. Ya. Kode, V. A. Terektova, Bull. Acad. Sci. U. S. S. R. 1965, 5, 873

[77] M. I. Morozov, N. A. Lomanova, V. V. Gusarov, Russ. J. Gen. Chem. 2003, 73, 1680.

[78] R. Palai, R. S. Katiyar, H. Schmid, P. Tissot, S. J. Clark, J. Robertson, S. A. T. Redfern, G. Catalan, J. F. Scott, Phys. Rev. B 2008, 77, 014110.

[79] Catalan G, Scott J F, "Physics and Application of Bismuth Ferrite", *Adv. Mater.* 2009, 21, 2463

[80] Lou X J, Yang C X, Tang T A, Lin Y Y, Zhang M, Scott J F, "Formation of Magnetite in Bismuth Ferrite under Voltage Stressing" *Appl. Phys. Lett.* 2007, 90, 262908.

[81] Jong Kuk Kim et al, Materials Letters 59 (2005) 4006 – 4009

[82] Alain C. Pierre, "Introduction to Sol-Gel Processing", Kluwer Academic Publishers

[83] Chao Chen et al, Journal of Crystal Growth 291 (2006) 135–139

[84] Hardy et al., Journal of European Ceramic Society.29, 3007 (2009)

[85] Xue et al., Materials Research Bulletin.43, 3368 (2008)

[86] H. Ke, W. Wang, Y. Wang, J. Xu, D. Jia, Z. Lu, Y. Zhou, J. Alloys Compd. 509 (2011) 2192–2197.

[87] Jiang et al., J Electroceramics.21, 690 (2008)

[88] S. Farhadi, M. Zaidi , Journal of Molecular Catalysis A: Chemical 299 (2009) 18–25

[89] Seema et al. JPMS Conference Issue, Materials 2010 (pg 12-18)

[90] NSTI-Nanotech 2010 conference proceedings, Vol. 1, 2010 (53-56)

[91] Singanahally T. Aruna, Alexander S. Mukasyan," Combustion synthesis and nanomaterials", *Current Opinion in Solid State and Materials Science* 12 (2008) 44–50

[92] Marc Monthioux, Vladimir L. Kuznetsov," Who should be given the credit for the discovery of carbon nanotubes?",CARBON 44 (2006) 1621

[93] Radushkevich LV, Lukyanovich VM. O strukture ugleroda, obrazujucegosja pri termiceskom razlozenii okisi ugleroda na zeleznom kontakte. Zurn Fisic Chim 1952; 26: 88-95.

[94] Park T J, Mao Y, Wong S S, *Chem Comm*, **2004**, 2708.

[95] Zhang X Y, Lai C W, Zhao X, Wang D Y, Dai J Y, *Appl. Phys. Lett.* 2005, 87, 143102

[96] Li C Y, Liu B, Zhao J P, Wang J F, Hu B B, Du Z L, *Chin. Sci. Bull*. 2009, 54,179.

[97] Gao F, Yuan Y, Wang K F, Chen X Y, Chen F, Liu J M, Ren Z F, *Appl. Phys. Lett.* 2006, 89, 102506.

[98] Xie S H, Li J Y, Proksch R, Liu Y M, Zhou Y C, Liu Y Y, Ou Y, Lan L N, Qiao Y, *Appl. Phys. Lett.* 2008, 93, 222904.

[99] Zhang L, Cao X F, Ma Y L, Chen X T, Xue Z L, *J. Solid State Chem.* 2010, 183, 1761.

[100] Yi Liu, Ruzhong Zuo," Tunable morphology and optical absorption of bismuth ferrite synthesized by sol–gel–hydrothermal method", Journal of Materials Science: Materials in Electronics, 2012

[101] X.M. Lu, J.M. Xie, Y.Z. Song, J.M. Lin, J. Mater. Sci. 42, 6824 (2007)

[102] X.Z. Chen, Z.C. Qiu, J.P. Zhou, G.Q. Zhu, X.B. Bian, P. Liu, Mater. Chem. Phys. 126, 560 (2011)

[103] Y.G. Wang, G. Xu, L.L. Yang, Z.H. Ren, X. Wei, W.J. Weng, P.Y. Du, G. Shen, G.R. Han, Ceram. Int. 35, 1285 (2009)

[104] X.L. Chen, Y. Tang, L. Fang, H. Zhang, C.Z. Hu, H.F. Zhou, J. Mater. Sci.: Mater. Electron. (2012).

[105] Joshi U A, Jang J S, Borse P H, Lee J S, *Appl. Phys. Lett.* 2008, 92, 242106.

[106] Li S, Lin Y H, Zhang B P, Wang Y, Nan C W, *J. Phys. Chem. C*, 2010, 114, 2903.

[107] Han J T, Huang Y H, Wu X J, Wu C L, Wei W, Peng B, Huang W, Goodenough J B, *Adv. Mater.* 2006, 18, 2145.

[108] J. Li, Y. Duan, H. He, D. Song, *J. Alloys Compounds*, 315 (2001) 259.

[109] V.R. Palkar, D.C. Kundaliya, S.K. Malik, J. Appl. Phys. 93 (2003) 4337.

[110] Y.K. Jun, W.T. Moon, C.-M. Chang, H.-S. Kim, H.S. Ryu, J.W. Kim, K.H. Kim, S.-H. Hong, Solid State Commun. 135 (2005) 133.

[111] R. Mazumder, A. Sen, Journal of Alloys and Compounds 475 (2009) 577–580

[112] Cheong S W & Mostovoy M, *Nature Mater*, 6 (2007) 13.

[113] Ramesh R & Spaldin N A, *Nature Mater*, 6 (2007) 21.

[114] Rao C N R & Serrao C R, *J Mater Chem*, 17 (2007) 4931.

[115] Komchenko V A, Kiselev D A, Selezneva E K, Vieira J M, Lopes A M L, Pogorelov Y G, Araujo J P & Kholkin A L, Mater Lett, 62 (2008) 1927.

[116] Wang L Y, Wang D H, Huang H B, Han Z D, Cao Q Q, Gu X X & Du Y W, *J Alloys Compounds*, 469 (2009) 1.

[117] Wang D H, Goh W C, Ning M & Ong C K, *Appl Phys Lett*, 88 (2006) 212907

[118] Kothari D, Reddy V R, Gupta A, Sathe V, Banerjee A, Gupta S M & Awasthi A M, Appl Phys Lett, 91 (2007) 202505.

[119] Sahu J R & Rao C N R, *Solid State Sci*, 9 (2007) 950.

[120] Uniyal P & Yadav K L, Mater Lett, 62 (2008) 2858.

[121] Nalwa K S, Garg A & Upadhyaya A, Mater Lett, 62 (2008) 878

[122] Cheng Z X, Li A H, Wang X L, Dou S X, Ozawa K, Kimura H, Zhang S J & Shrout T R, J Appl Phys **103 (2008)** 07E507

[123] Zhang S, Pang L H, Zhang Y, Lu M H & Chen Y F, J Appl Phys, 100 (2006) 114108

[124] A. Fujishima and K. Honda, Nature (London) **37**, 238 (1972)

[125] Michael R. Hoffmann, Scot T. Martin, Wonyong Choi, and Detlef W. Bahnemann," Environmental Applications of Semiconductor Photocatalysis", *Chem. Rev. 1995, 95,* 69-96.

[126] Marye Anne Fox, Maria T.Dulay. "Heterogeneous Photocatalysis'. Chemical Reviews, 1993. Vol.93, pp341-357.

[127] Gratzel, M. *Heterogeneous Photochemical Electron Transfer;* CRC Press: Boca Raton, FL, **1989**

[128] Rothenberger, G.; Moser, J.; Gratzel, M.; Serpone, N.; Sharma, D. K. *J.Am. Chem. Soc.*1985, 107, 8054.

[129] Rao, M. V.; Rajeshwar, K.; Vernerker, V. R.; Dubow, J. *J. Phys. Chem.* **1980, 84,** 1987.

[130] Nishimoto, S.; Ohtani, B.; Kajiwara, H.; Kagiya, T. *J. Chem. Soc., Faraday Trans. 1* **1985, 81,** 61.

[131] Kakuta, N.; White, J. M.; Bard, A. J.; Campion, A.; Fox, M. A.; Webber, S. E.; Finlayson, M. *J. Phys. Chem.* **1986,89,48.**

[132] V. Pleskov, Semiconductor Photochemistry, Springer (1986) ISBN: 978-0306109836

[133] Asahi, R., T. Morikawa, et al. (2001). "Visible-light photocatalysis in nitrogen-doped titanium oxides." Science **293**(5528): 269-271.

[134] Zhu, Y.; Zhang, L.; Yao, W.; Cao, L. Appl. Surf. Sci. 2000 158, 32–37.

[135] Andronic, L. et al. Chemical Engineering Journal 152 (2009) 64-71)

[136] K.Nagaveni et al. Journal of Physical Chemistry B 108, 20204 (2004)

[137] Yuping He et al. Chem Mater 2003, 15, 4039-4045

[138] Brody, P.S., Solid State Commun., 1973. **12**: p. 673-676.

[139] Glass, A.M. and D.v.d. Linde, Appl. Phys. Letters, 1974. **25**: p. 233-235.

[140] Brody, P.S. and F. Crowne, J. Elect. Mater., 1975. **4**: p. 955-971.

[141] Baltz, R.V., Phys. Stat. Sol. (b), 1978. 89: p. 419-429.

[142] Fridkin, V.M., Ferroelectrics, 1984. 53: p. 169-187.

[143] Ambacher O, Smart J, Shealy JR, Weimann NG, Chu K, Murphy M, Dimitrov R, Wittmer L, Rieger W, Hilsenbeck J (1999) J Appl Phys 85:3222

[144] J. Garra, J. M. Vohs, D. A. Bonnell, **2009**, *Surf. Sci., 603*, 1106.

[145] A. Harhira, L. Guilbert, P. Bourson, H. Rinnert, **2007**, *Physica Status Solidi (C) Current Topics in Solid State Physics, 4*, 926.

[146] K. Takahashi, N. Kida, M. Tonouchi, *Phys. Rev. Lett.* 2006, *96*, 117402

[147] J. Xu, G. Zhang, F. Li, X. Zhang, Q. Sun, S. Liu, F. Song, Y. Kong, X. Chen, H. Qiao, J. Yao, Z. Lijuan, **2000**, *Opt. Lett., 25*, 129.

[148] Kalinin SV, Bonnell DA, Alvarez T, Lei X, Ferris JH, Dunn S, Zhang Q (2002) Nanoletters 2:589

[149] Kalinin, S.V., et al., Adv. Mater., 2004. **16**: p. 795-799.

[150] J. Lou and P. A. Maggard, Adv. Mater. 18, 514 (2006).

[151] S. M. Selbach, T. Tybell, M.-A. Einarsrud, and T. Grande, Chem. Mater. **19**, 6478 (2007).

[152] S. Shetty, V. R. Palkar, and R. Pinto, Pramana **58**, 1027 (2002).

[153] Y.-H. Lin, Q. H. Jiang, Y. Wang, C.-W. Nan, L. Chen, and J. Yu, Appl. Phys. Lett. **90**, 172507 (2007).

[154] Mazumder, P. Sujatha Devi, Dipten Bhattacharya, P. Choudhury, A. Sen, and M. Raja, Appl. Phys. Lett. **91**, 062510 (2007).

[155] C. Ederer and N. A. Spaldin, Phys. Rev. B **71**, 224103 (2005).

[156] Shun Li, Yuan-Hua Lin, Bo-Ping Zhang, Ce-Wen Nan and Yao Wang," Photocatalytic and magnetic behaviors observed in nanostructured BiFeO3 particles", *Journal of Applied Physics*, 2009, 105, 056105.

[157] P. Jones, D. E. Gallardo and S. Dunn, Chemistry of Materials, 20, 5901-5906 (2008)

[158] Shun Li, Yuan-Hua Lin, Bo-Ping Zhang, Jing-Feng Li, and Ce-Wen Nan," BiFeO3 /TiO2 core-shell structured nanocomposites as visible-active photocatalysts and their optical response mechanism," *Journal of Applied Physics* 105, 054310 (2009)

[159] Junhua Luo et al. Advanced Materials 2006, 18, 514-517

[160] C. Madhu, B. Manjunath, Belakki and V. Manivannan, Indian J Eng. Mater. Sci., 2010, 17, 131–139.

[161] Y. Zhang, A.M. Schultz, P.A. Salvador, and G.S. Rohrer, J. Mater. Chem., 2011, 21, 4168

[162] T.-J. Park et al., Nanoletters 7, 766 (2007).

[163] R. Guo, L. Fang, W. Dong, F. Zheng, and M. Shen, *J. Phys. Chem. C* 2010, *114*, 21390–21396

[164] M. Popa, S. Preda, V. Fruth, K. Sedláčková, C. Balázsi, D. Crespo, J. M. Calderón-Moreno, Thin Solid Films 517 (2009) 2581–2585

[165] A.Lahmar, S.Habouti, M.Dietze, C.-H.Solterbeck, M.Es-Souni, Applied Physics Letters 94 (2009) 012903.

[166] F.Yan, M.Lai, L.Lu, T.J.Zhu, Journal of Physical Chemistry C 114 (2010) 6994–6998.

[167] Puli V.S, Kumar A, Panwar N, Panwar I.C, Katiyar R.S, Journal of Alloys and Compounds 509 (2011) 8223– 8227

[168] M. Kumar, K. L. Yadav. Appl. Phys. Lett, 91 (2007) 242901.

[169] Zhang, A. P.; Zhang, J. Z. *J. Hazard. Mater.* **2010**, *173*, 265

[170] S. Iakovlev, C.-H. Solterbeck, M. Kuhnke and M. Es-Souni, J. Appl. Phys. 97, 094901 (2005).

[171] X.D.Qi, J.Dho, R.Tomov, M.G.Blamire, J.L.M.Driscoll, Applied Physics Letters 86 (2005) 062903.

[172] Q.Ke, X.Lou, Y.Wang, J.Wang, Physical Review B 82 (2010) 024102.

[173] G.D.Hu, S.H.Fan, C.H.Yang, W.B.Wu, Applied Physics Letters 92 (2008) 192905.

[174] Fujino, S.; Murakami, M.; Anbusathaiah, V.; Lim, S.-H.; Nagarajan, V.; Fennie, C. J.; Wuttig, M.; Salamanca-Riba, L.; Takeuchi, I. *Appl. Phys. Lett.* **2008**, *92*, 202904.

[175] Bhardwaj, A.; Burbure, N. V.; Chen, L.; Gamalski, A.; Rohrer, G. S. *Chem. Mater.* **2010**, *22*, 3257.

[176] S. -T. Zhang, Y. Zhang, M. -H. Lu, C. -L. Du, Y. -F. Chen, Z. -G. Liu, Y. -Y. Zhu, N. -B. Ming, and X. Q. Pan. *Appl. Phys. Lett.* ***2006, 88,*** 162901

[177] G. L. Yuan, S. W. Or, J. M. Liu, and Z. G. Liu, *Appl. Phys. Lett.* **2006, *89, 052905.***

[178] Kan, D.; Palova, L.; Anbusathaiah, V.; Ching, C. J.; Fujino, S.; Nagarajan, V.; Rabe, K. M.; Takeuchi, I. *AdV. Funct. Mater.* ***2010, 20,*** 1108.

[179] Sergio Valencia, Juan Miguel Mar ń and Gloria Restrepo, ***The Open Materials Science Journal,*** **2010,** ***4,*** **9-14**

[180] Chang Hengky, Xavier Moya, Neil D. Mathur and Steve Dunn," Evidence of high rate visible light photochemical decolourisation of Rhodamine B with BiFeO3 nanoparticles associated with BiFeO3 photocorrosion" RSC Adv., 2012, 1–7, DOI: 10.1039/c2ra22211f

APPENDIXES

List of presentations and publications:

1. Chang Hengky and Steve Dunn,"Preparation and Characterization of $BiFeO_3$ nanosystems as visible light driven photo-degradation of organic compound",NSTI-Nanotech 2010, www.nsti.org, ISBN 978-1-4398-3401-5 Vol.1 (pp 570 – 573): Presentations to Nanotech 2010 conference.

2. Chang Hengky and Steve Dunn,"Photocatalytic decolourisation of RhB and photocorrosion of $BiFeO_3$" MRS Proceedings, Volume1443 (2012). DOI: http://dx.doi.org/10.1557/opl.2012.1190. 2012 MRS Spring Meeting.

3. Chang Hengky, Xavier Moya, Neil D. Mathur and Steve Dunn," Evidence of high rate visible light photochemical decolourisation of Rhodamine B with BiFeO3 nanoparticles associated with BiFeO3 photocorrosion" RSC Adv., 2012, 1–7, DOI: 10.1039/c2ra22211f